Observation of the 1S-2S Transition in Trapped Antihydrogen

Author

Steven Jones

Supervisor

Dr Stefan Eriksson

Prifysgol Abertawe
Swansea University

Submitted to Swansea University in fulfilment of the requirements for the Degree of Doctor of Philosophy

September 2017

Thesis summary

Our current understanding of physics suggests that matter and antimatter should be created and destroyed in equal amounts, but this seems inconsistent with the observation that our universe consists almost entirely of matter. Comparisons between matter and antimatter could reveal new physics which explains why the universe has formed with this apparent imbalance. The 1S-2S transition of hydrogen has been measured with incredible precision, and a similarly precise measurement of the 1S-2S transition of antihydrogen would constitute one of the best comparisons between matter and antimatter.

The ALPHA collaboration have been producing and trapping antihydrogen since 2010. This thesis presents an overview of the apparatus and techniques and examines the theoretical aspects of antihydrogen spectroscopy. Generating sufficient optical intensity at 243 nm to excite the 1S-2S transition in a reasonable amount of time requires an enhancement cavity. The development of this enhancement cavity and the setup of the ultra-stable 243 nm laser source form the main focus of this thesis.

The thesis concludes by reporting the first observation of the 1S-2S transition in trapped antihydrogen, which can be interpreted as a comparison between matter and antimatter at the 200 parts-per-trillion level. This result was aided by a significantly improved trapping rate of 10.5 ± 0.6 detected trapped antihydrogen atoms per production cycle, and the stacking of multiple production cycles without ramping down the magnetic trap to accumulate more than 70 simultaneously trapped antihydrogen atoms.

DECLARATION

This work has not previously been accepted in substance for any degree and is not being concurrently submitted in candidature for any degree.

Signed .... (candidate)

Date ....

STATEMENT 1

This thesis is the result of my own investigations, except where otherwise stated. Where correction services have been used, the extent and nature of the correction is clearly marked in a footnote(s).

Other sources are acknowledged by footnotes giving explicit references. A bibliography is appended.

Signed .... (candidate)

Date ....

STATEMENT 2

I hereby give consent for my thesis, if accepted, to be available for photocopying and for inter-library loan, and for the title and summary to be made available to outside organisations.

Signed .... (candidate)

Date ....

Table of Contents

i. Acknowledgements ix

ii. List of Figures xi

iii. List of Tables xxi

1 Introduction 1

- 1.1 The baryon asymmetry problem 1
- 1.2 Physics with low energy antiprotons 2
  - 1.2.1 The AD and ELENA 2
  - 1.2.2 Measurement of the antiproton-proton magnetic moment ratio 4
  - 1.2.3 Measurement of the antiproton-electron mass ratio 4
  - 1.2.4 Antihydrogen formation 4
- 1.3 Physics with antihydrogen 6
  - 1.3.1 Magnetically trapping antihydrogen 6
  - 1.3.2 Tests of the weak equivalence principle 7
  - 1.3.3 Measuring the charge neutrality of antihydrogen 7
  - 1.3.4 Microwave spectroscopy of antihydrogen 8
  - 1.3.5 Laser spectroscopy of antihydrogen 9

2 Antihydrogen production in the ALPHA apparatus 11

- 2.1 The apparatus 11
  - 2.1.1 Penning traps 12
  - 2.1.2 Catching trap 14
  - 2.1.3 Positron accumulator 15
  - 2.1.4 Atom trap 17
  - 2.1.5 Sequencing and data acquisition 18
- 2.2 Tools and diagnostics 18
  - 2.2.1 Sticks 18
  - 2.2.2 Electron gun 19
  - 2.2.3 Faraday cup 19
  - 2.2.4 Multichannel plate 19
  - 2.2.5 Flappers 20
  - 2.2.6 Scintillator panels 21
  - 2.2.7 Silicon vertex detector 22
  - 2.2.8 Temperature diagnostics 23

2.2.9 Magnetometry....24
2.3 Antihydrogen formation and trapping....26
2.3.1 Autoresonant mixing....26
2.3.2 Slow merge mixing....27
2.3.3 Antihydrogen accumulation....28
2.4 Antihydrogen detection....29
3 Antihydrogen spectroscopy considerations....31
3.1 The hydrogen atom....32
3.1.1 Historical observations....33
3.1.2 The Bohr model....33
3.1.3 Fine structure....34
3.1.4 The Lamb shift....35
3.1.5 Hyperfine structure....36
3.1.6 The Zeeman Effect....37
3.1.7 Diamagnetic shift....38
3.1.8 Antihydrogen 1S-2S frequencies....38
3.2 Systematic shifts and broadenings....39
3.2.1 Residual Zeeman Effect....40
3.2.2 Stark effect....41
3.2.3 Transit time broadening....41
3.2.4 2S lifetime reduction....42
3.3 Simulated transition rates....43
3.4 Detection schemes....44
3.4.1 Ly-α detection....44
3.4.2 Annihilation - disappearance mode....45
3.4.3 Annihilation - appearance mode....45
4 The 1S-2S Enhancement Cavity....47
4.1 Enhancement cavity theory....48
4.1.1 Resonance....49
4.1.2 Transverse mode matching....51
4.1.3 Cavity locking techniques....54
4.1.4 Cavity power....56
4.2 Athermal mirror cell development....57

4.2.1 Design and Prototyping 58
4.2.2 Mirror cell assembly 60
4.2.3 Optical deformation measurements 62
4.2.4 Improved interferometry 70
4.3 Internal cavity mechanical design 74
4.4 External cavity mechanical design 80
4.5 Optical design 83
4.6 Performance 85
4.6.1 Loss versus reflectivity 87
4.6.2 Laser induced damage 88
4.6.3 Spatial mode matching 90
4.7 Mirror degradation and recovery 92
5 The 1S-2S Laser System 93
5.1 243 nm light generation 93
5.2 Frequency control and metrology 96
5.2.1 Reference cavity 96
5.2.2 Frequency comb 98
5.2.3 Frequency shifter 99
5.3 Beam transport 101
5.3.1 Optical components 102
5.3.2 Losses 103
5.3.3 Alignment 105
5.3.4 Active beam stabilisation 106
6 Experimental results 107
6.1 Experimental protocol 107
6.1.1 2014 107
6.1.2 2015 108
6.1.3 2016 109
6.2 Results and analysis 111
6.2.1 2014 111
6.2.2 2015 111
6.2.3 2016 112
6.3 Conclusion 115

7 Conclusions and Outlook 117
References 119

i. Acknowledgements

Firstly, I would like to thank my supervisor Dr. Stefan Eriksson, for his dedication and guidance. I would also like to thank Prof. Niels Madsen and Prof. Jeffrey Hangst for their support throughout, as well as the rest of the senior researchers at ALPHA for sharing their knowledge and expertise with me. ALPHA is a collaboration in which the work and opinions of a student are treated with the same respect as a senior researcher, and I could not have asked for a better environment to work in.

Thanks to all of my fellow students and post-docs within the ALPHA collaboration, who have truly become my family away from home. In particular, I would like to thank Chris, Graham, and Bruno, who have all experienced the joys and frustrations from round-the-clock work on the 243 nm laser.

I would like to acknowledge and thank Swansea University and the Engineering and Physical Sciences Research Council (EPSRC) for funding my PhD scholarship, which has been the most amazing opportunity.

Thanks to the friends I’ve made through the CERN board games club, past and present, who are too many to name. Also, a special thank you to my parents for their continuous love and support, even when I decided to move to Geneva.

And finally, I would like to thank Melina, for sharing the adventure with me.

ii. List of Figures

Figure 1.1: A schematic of the AD hall experiments in the 2017 run configuration. The ATRAP zone is on a platform above the surrounding experiments. ELENA and GBAR are still in the commissioning phase. The GBAR zone includes a shielded linear accelerator for positron production. Image adapted from [6]. 3

Figure 1.2: A Breit-Rabi diagram showing the Zeeman splitting of the (anti)hydrogen ground state. The ALPHA collaboration injected resonant microwaves (shown by the black arrows) into the 1 T magnetic trap, and observed a spin flip of the positron (single arrow) which caused the atoms to seek a high magnetic field and annihilate on the walls of the trap. Image from [25]. 8

Figure 2.1: An overview of the ALPHA beamline. Antiprotons are captured in the 3 T field of the CT and cooled using electrons loaded from the CT stick. Meanwhile, positrons are accumulated in a 3-stage Surko-type accumulator. After initial preparations, both species antiprotons and positrons are transferred into the AT for antihydrogen production and trapping. Small solenoids are positioned along the beamline to aid the transfer of particles. The distance between the CT and AT is approximately 3 m. 11

Figure 2.2: A simple Penning-Malmberg trap constructed from three stacked cylindrical electrodes. 13

Figure 2.3: The motion of a single particle in a Penning trap is described by a combination of the magnetron (green), cyclotron (black), and axial motion (red). The image is adapted from [28]. 13

Figure 2.4: A sketch of the catching trap electrode stack. The trap has a length of 396 mm and an inner diameter of 29.6 mm. The two high voltage electrodes are shown in blue and the segmented electrodes used for plasma compression are shown in yellow. An external solenoid provides a 3 T field to complete the Penning trap. The antiproton beam enters from the left of the image. 14

Figure 2.5: a) After an initial stage of rotating wall compression, the antiprotons (left) and the electrons (right) are centrifugally separated [30]. b) Kicking out 90% of the electrons allows the antiprotons to be compressed further. c) Finally, the remaining electrons are kicked out and the antiprotons are ready for transfer. The two species map to different locations on the MCP due to a small misalignment between the electrode stack and the magnetic field. 15

Figure 2.6: A schematic of the positron accumulator. Positrons are emitted from a 5 Kelvin ^{22}Na source (blue) and accumulated in a three stage Penning-Malmberg trap (orange). The accumulator is equipped with a small vertical translator containing a phosphor screen (red) for imaging the positrons and a grounded pass-through tube. The image is adapted from [33]. 16

Figure 2.7: The high energy positrons are cooled by interacting with a nitrogen buffer gas within the electrodes. The accumulator is differentially pumped such that the cooling interactions are strongest in the first stage (right hand side of graph) and the lifetime is prolonged in the third stage (left hand side of graph). The image is adapted from [33]. 16

Figure 2.8: A schematic of the nested Penning-Malmberg and Ioffe-Pritchard traps within the ALPHA-2 atom trap. The antiprotons are transferred in from the left hand side and the positrons are transferred in from the right hand side of the image. The electrodes are in the UHV space, whereas the magnets are in direct contact with liquid helium. An outer vacuum chamber and a layer of super-insulation reduce the heat load on the cryostat. Not shown is an external 1T solenoid. 17

Figure 2.9: The locations of the scintillator panels are highlighted on the CT (left) and AT (right). The scintillators are positioned in pairs either side of the solenoids. Portable scintillator pairs are positioned next to the diagnostic sticks when additional information about the annihilation position is needed. 21

Figure 2.10: An example reconstruction of an antiproton annihilation (left) and a cosmic ray event (right). The blue diamond indicates the position of the reconstructed annihilation event, the red dots the positions of the detected hits, and the inner circle shows the radius of the Penning trap electrodes. Image adapted from [39]. 22

Figure 2.11: A plot of the detection efficiency against the accepted background rate for the MVA analysis. For reference, the performance of the standard online analysis is circled in red. The data displayed is from around 670 mixing cycles and 82 hours of cosmic data from 2014. The Y-axis error bars are negligible. 23

Figure 2.12: An example of an ECR line shape recorded during the 2016 beam period. The trace shows the quadrupole vibrational mode frequency of an electron plasma when excited by microwave pulses of increasing frequency. 25

Figure 2.13: In the autoresonant scheme (left), the antiprotons are excited into the positrons by a chirped frequency. In the slow merge scheme (right), the initial wells (solid line) are reduced until the two species spill into each other (dashed line)....... 27

Figure 2.14: The number of trapped atoms increases linearly with each successive mixing cycle. The error bars show the N counting statistics alone. The detection efficiency is 73.0±0.4%... 29

Figure 3.1: The energy levels of the hydrogen atom are illustrated as the accuracy of models which describe them improves. The horizontal axis shows the quantum numbers which describe the energy levels, and are introduced in the text. The vertical axis shows the energy of the levels, but the scale is illustrative only. 32

Figure 3.2: Feynman diagrams showing the most significant contributions to the Lamb shift [50]... 36

Figure 3.3: The calculated Breit-Rabi diagrams of the 1S (bottom) and 2S (top) states of antihydrogen. The blue lines show the low-field seeking trappable states and the red lines show the high-field seeking untrappable states. Image from [60]......... 39

Figure 3.4: A plot of three possible magnetic field configurations. The black markers labelled A-E show the approximate sizes and locations of the mirror coils. Image from [52]. 40

Figure 3.5: A simulation of the interaction between the antihydrogen atoms within the flattened trap yields the excitation rate and the linewidth of the summed c-c and d-d transitions. The inset shows the time dependence of the excitation period. Image from [60]. 44

Figure 3.6: A close-up image of an antiproton annihilation on an MCP which has left identifiable tracks. The surrounding bright spots are also due to antiproton annihilations. 46

Figure 4.1: A two-mirror Fabry-Pérot cavity 48

Figure 4.2: A plot of the beam waist (top) and the wavefront radius of curvature (bottom) for a Gaussian beam with $w0 = 0.2\ mm,\ \lambda = 243\ nm$, and $z0 = 0.517$ m over a 6 m propagation length. 52

Figure 4.3: The stability of different cavity configurations as defined by their g factors (g_1,g_2). Only the configurations under the blue shaded region are stable. Image by [63]. 53

Figure 4.4: Hermite-Gaussian (top) and Laguerre-Gaussian (bottom) modes. Image from [64] 54

Figure 4.5: The 'x' shows the lock points for the side of peak lock (left) and the amplitude modulation error signal (right). The frequency scale is the same for both plots. 55

Figure 4.6: The frequency/phase modulation adds sidebands to the beam, which are visible in the transmitted signal (left). The capture range of the PDH error signal extends to the sidebands, yet maintains a sharp slope to lock to (right). The 'x' indicates the lock point. 56

Figure 4.7: An athermal mirror cell consisting of an optic (green) bonded within a metal ring (grey) using an epoxy (orange). Autodesk Inventor model. 57

Figure 4.8: A close up view of the cell making jig, showing the locations where the ring and optic sit (Autodesk Inventor drawing). 61

Figure 4.9: The optic and ring are placed onto the jig. The ring is clamped via two slash-cut needles and the optic is clamped via a Teflon spacer whilst the epoxy cures (Autodesk Inventor model). 61

Figure 4.10: The mirror cell is epoxied to a stainless steel adapter piece using the same epoxy and curing process as the cell manufacture. The adapter piece threads into a copper heat sink which is cooled to 20 K by the inner stage of a coldhead. The heat sink is equipped with a Cernox temperature sensor and a heater element. Connected to the outer stage of the coldhead is a copper radiation shield, which has a Ø 12 mm hole for optical access. 63

Figure 4.11: The coldhead cools from room temperature to 20 K in just under 3 hours, which is similar to the cooldown rate of the ALPHA apparatus.................... 63

Figure 4.12: A 767 nm single mode laser is coupled into a fibre and output onto an optical bench. The light is collimated at Ø 10 mm and split into two beams using a 50-50 beam splitter. One beam is reflected from the mirror cell under test, whilst the other is reflected from a flat reference mirror. The vacuum window and the beam splitter have THORLABS –B NIR anti-reflection coatings to prevent multiple images. The test and reference mirrors are both THORLABS PF05-03 mirror blanks, which have a ground back surface to prevent multiple reflections. Recombining the beams creates an interference pattern which is imaged on a screen. A webcam placed behind the screen saves the image for analysis... 64

Figure 4.13: An example of two interference patterns generated by the interferometer. The image on the left has no tilt between the two mirrors, whereas the image on the right has a tilt of 6 waves. The edge of the images corresponds to the edge of the Ø10 mm laser beam.. 65

Figure 4.14: The image on the left shows the interference pattern with the dark fringes traced, and the image on the right shows a reconstruction of the surface using Zernike polynomials... 66

Figure 4.15: An initial measurement of the 0.5 mm H77 titanium cell. The chamber is at room temperature and under a vacuum of $1\times 10-6$ mbar.............................. 68

Figure 4.16: A measurement of the surface of the 0.5 mm H77 titanium cell when cooled to 20 K for the first time. The mirror appears to have bulged outwards by >1100 nm. The surface looked similar for the subsequent two cooldowns. The vacuum reaches $1\times 10-8$ mbar when the coldhead is at 20 K... 68

Figure 4.17: A measurement of the surface of the 0.5 mm H77 titanium cell at room temperature and still under vacuum after 3 thermal cycles. There appears to be a residual deformation of around 400 nm.. 68

Figure 4.18: An initial measurement of the 0.5 mm T7109 titanium cell. The chamber is at room temperature and under a vacuum of $1\times 10-6$ mbar............... 69

Figure 4.19: A measurement of the surface of the 0.5 mm T7109 titanium cell when cooled to 20 K. There is no obvious deformation within the precision of the interferometer. 69

Figure 4.20: A measurement of the surface of the 0.5 mm T7109 titanium cell at room temperature and still under vacuum after thermally cycling. There is no obvious change from the initial surface. 69

Figure 4.21: In this improved interferometer setup, a stabilised 532 nm laser is coupled into a single mode fibre and output onto an optical bench which is directly mounted to the cryostat. Not shown are a 400 V piezo driver and a laptop equipped with a NI-DAQ module for controlling the piezo and acquiring images from the camera. The optics are coated for visible light and the vacuum window is wedged to prevent interference patterns from the window surfaces being imaged. The setup is designed to be as compact and lightweight as possible to avoid coupling vibrations into the cryostat. 71

Figure 4.22: The deformation of a mirror blank in a 0.5 mm athermal cell cooled to 20 K. 72

Figure 4.23: The residual deformation of a mirror blank after being thermally cycled between room temperature and 20 K. 72

Figure 4.24: A plot of the radial gap size of an athermal cell vs the cooldown deformation of the central Ø 12 mm of the optic. A positive deformation indicates a bulging of the mirror surface. In each case, the deformation was almost purely a defocussing of the mirror. For small deformations the error is approximately the resolution of the interferometer, whereas for larger deformations, the error is dominated by knowledge of the beam size and image edge. Inset is the result of the DeLuzio stress calculation based on equation 4.30, which is in rough agreement with the trend and the zero-crossing point. 74

Figure 4.25: From left to right: The upstream triangle, the upstream end of the magnet form, the downstream end of the magnet form, and the downstream triangle. Both triangles contain two slots for mounting a mirror assembly, but are shown with only one mirror assembly installed. 75

Figure 4.26: The mirror cell, piezo (yellow with grey electrodes), and downstream adapter piece mounted within the alignment jig. A similar jig is used to ensure the alignment of the upstream assembly. 76

Figure 4.27: The upstream and downstream mirror adapter pieces. 76

Figure 4.28: The downstream adapter pieces still mounted into the triangle (left) and one of the piezo assemblies (right). The piezos were attached to the adapter pieces by placing beads of epoxy around the outer diameter, but the piezo also seems to have bonded close to the inner diameter. Piezo material can be seen still bonded to the adapter pieces. 77

Figure 4.29: The modified downstream adapter. 77

Figure 4.30: As the triangle was inserted, one of the support rods (highlighted) came into contact with the piezo assembly and sheared it off. A kapton bumper was installed to protect the piezo against knocks during installation, but this had also been sheared and epoxy had been scraped off the piezo, implying that the damage was done when holding tension was applied to the back of the triangle. 78

Figure 4.31: A 13 mm PI Ceramic's PAHH+0050 piezo was cooled down to 20 K on a coldhead. The travel was measured interferometrically as the piezo warmed up. 79

Figure 4.32: A Bode plot of the piezo electrical response at 7 K. The black curve shows the magnitude and the blue curve shows the phase of the response relative to the drive signal. 79

Figure 4.33: A photograph of the assembled mirror flange. The flange adapter contains holes to allow the space in the bellows behind it to be pumped, but it is an acknowledged pumping restriction. The mirror, piezo, and adapter are bonded using EPOTEK T7109 epoxy. 80

Figure 4.34: The mirror is mounted on a piezo between two bellows. The window is clamped in place, allowing the mirror flange to be titled using a modified commercial mirror mount. 81

Figure 4.35: An Autodesk Inventor rendering (left) and photograph (right) of the structure designed to clamp the external cavity assembly to the beamline. The vacuum window is not shown. 82

Figure 4.36: The highlighted nuts on the M4 threaded rods were loosened or tightened to adjust the alignment of the cavity mirror. 82

Figure 4.37: A histogram of the cavity length fluctuation in nm over 100 s, as measured by a wave meter when the laser was locked to the external cavity. 83

Figure 4.38: In a confocal cavity, transverse modes (red) are frequency degenerate as all path lengths are equal. As the cavity is made longer or shorter, the transverse modes will separate. 84

Figure 4.39: A photograph of the 2015 upstream window mounted on the bench. A large diameter 243 nm beam was sent through and the transmission was measured using a CCD camera. The laser induced damage can already be seen by the dark spot within the blue fluorescence. 89

Figure 4.40: A small burn spot is present on the AR coating of the upstream mirror. 90

Figure 4.41: The PDH error signal (upper) and the transmitted intensity (lower) as the piezo is scanned linearly over 50 V to cover a full free spectral range of the cavity. 91

Figure 4.42: A saturated image of the transmitted beam when the cavity has been locked on resonance for 1 s (left) and 30 s (right). 91

Figure 5.1: A schematic of the optical elements in the 1S-2S spectroscopy setup. The red, cyan, and navy blue lines show the propagation of the 972, 486, and 243 nm light respectively. Some steering mirrors have been removed for simplicity. 94

Figure 5.2: The internal layout of the Toptica TA-FHG pro laser, which generates the high power 243 nm light for antihydrogen spectroscopy. Image modified from [61]. 95

Figure 5.3: A flow chart of the frequency control setup. 96

Figure 5.4: The set point of the PDH lock to the reference cavity was adjusted at 100 s intervals to ± 1 FWHM of the measured noise of the locked cavity, the frequency of the laser is measured using the frequency comb. The difference between the blue and red points gives 2 x the FWHM of the laser linewidth, assuming the dominant source of broadening of the linewidth is the quality of the lock. 97

Figure 5.5: A schematic diagram of a v-2v frequency comb. The repetition rate (v_{rep}) is referenced to a microwave clock, and the offset of the zeroth line (v_0) can be determined by measuring the beat note between the frequency-doubled red end of the comb and the blue end. 98

Figure 5.6: An AOM in double-pass configuration is used to shift the 972 nm light to the reference cavity frequency (not to scale). The black curve illustrates the gain profile of the AOM, which must be accounted for when normalising the output power. 100

Figure 5.7: A non-overlapping Allen deviation measurement of the fractional uncertainty of the comb locked to the OCXO (black dots) and the light sent to the reference cavity (red dots). The turning point at 20 s corresponds to a fractional uncertainty of $2.45 \times 10 - 13$, or equivalently, 75 Hz at 972 nm. 101

Figure 5.8: The fluorescence observed from a 243 nm beam passing through a standard UV grade fused silica substrate changes from pale blue to bright red after several hours of exposure, and the transmission through the substrate falls. 102

Figure 5.9: The black trace at the top of the graph shows the control voltage applied to a piezo used to scan the length of the cavity over a full spectral range. The blue trace shows the temporal mode structure of a cavity which is enclosed by a tube and the red trace shows the mode structure of a cavity which is stirred by the laboratory air conditioning. 104

Figure 6.1: A plot of the declining mixing triggers (proportional to antihydrogen production) when the 243 nm cavity is locked for two trapping series with 1 W circulating power (black squares) and 0.65 W of circulating power (red circles). The first few points of the 0.65 W series are low as the laser experiment has begun whilst some trap surfaces are still cooling down. 113

Figure 6.2: Evolution of the trapping data for the on resonance, off resonance, and no laser runs. The error bars represent the counting statistics (N) alone. 114

iii. List of Tables

Table 3.1: Spectroscopic notation. 34

Table 3.2: A summary of the shifts and broadenings which contribute >1 kHz towards the total 1S-2S transition frequency 42

Table 4.1: A comparison of the properties of EPO-TEK H77 and EPO-TEK T7109 epoxies. Data from the H77 [70] and T7109 [71] datasheets. It is important to note that the CTE data for the epoxies was only available down to 228K and must be extrapolated down to 7K. 59

Table 4.2: A calculation of optimal radial bond thicknesses using the Bayar and DeLuzio equations for four potential mirror cells... 60

Table 4.3: A summary of the deformation of a 0.5 mm T7109 titanium athermal mirror cell when cooled from room temperature to 20 K, for different batches of the same epoxy.. 73

Table 4.4: The enhancement cavity design parameters....................................... 85

Table 4.5: A summary of the cavity performance. Values marked with (*) were not well characterised as contributing effects were not discovered until later. The measured coupling is the ratio of injected to reflected light, and hence is a function of both the impedance mismatch and spatial mode matching... 87

Table 4.6: Measurements of the mirrors delivered to ALPHA. The "HR" mirror was specified for maximum reflectivity. The measured transmission is an average over several mirrors from each batch in new condition, including substrate losses. The variance between mirrors is approximately ± 5%.. 88

Table 5.1: Power losses at 243 nm as measured at the end of the 2016 run. The components are listed in the order they are seen by the beam, with the exception of the transport mirrors which are interspersed among the other components. 105

Table 6.1: A summary of the experimental protocol employed in 2014, 2015 and 2016.. 111

Table 6.2: The annihilation events detected during the shutdown of the neutral trap. The magnet system is intentionally quenched to de-energise the neutral trap in <30 ms, so there is no significant detector background. The error of the rate is from the N counting statistics alone. 111

Table 6.3: The annihilation events detected during the 1.5 s ramp down of the neutral trap magnets. The error of the rate is the standard deviation about the mean of the number of detected events. 112

Table 6.4: The number of events detected upon ramping down the trap after 2 x 300 s of laser exposure on resonance, laser exposure off resonance, or a wait without any laser exposure. The uncertainty is from the counting statistics(N) alone. 114

Table 6.5: Detector efficiency of the different protocols 115

Table 6.6: The number of events detected during the 300 s hold periods. The uncertainty is from counting statistics (N) alone. 115

1 Introduction

1.1 The baryon asymmetry problem

As predicted by the Standard Model of particle physics, and indeed as observed in high energy particle accelerators, particles and antiparticles are always created in pairs. Particles and antiparticles have opposite electrical charge and opposite baryon/lepton numbers, but are otherwise indistinguishable. However, when they recombine, they annihilate and release a blast of energy given by Einstein's famous equation;

$$E = mc^2. \tag{1.1}$$

One of the greatest open questions in physics today is the 'Baryon Asymmetry' problem. As the early universe cooled to the point where there was no longer enough energy to create particle-antiparticle pairs, one would expect the existing pairs to recombine and annihilate, leaving a universe devoid of both particles and antiparticles today. However, it seems a small fraction of these early universe particles survived to create the universe as we know it today. If matter and antimatter were originally created in equal amounts, then the question is simply "where is the antimatter?" The search for antimatter in astrophysics is ongoing, but no experiment to date has detected any signal, such as the distinctive 511 keV gamma rays emitted from electron-positron annihilations, which would be indicative of a significant quantity of antimatter in the observable universe [1]. Instead, physicists must consider a different hypothesis: "Is there a difference between matter and antimatter that has caused this imbalance, and can we measure it experimentally?"

A surprise result came in the form of a violation of charge conjugation and parity transformation (CP) symmetry, one of the fundamental symmetries of the Standard Model of Particle Physics. CP violation was first observed indirectly in 1964, when neutral kaons were observed to transform into their antiparticles and vice-versa with differing rates [2], and later measured explicitly by both the NA48 experiment [3] at CERN, and the KTeV experiment [4] at Fermilab. This CP violation is due to the existence of the Top and Bottom quarks in the Standard Model, and is explained by the Kobayashi–Maskawa model [5]. However, it is generally agreed that this amount of CP violation is not sufficient to explain the matter-antimatter imbalance alone.

The most fundamental symmetry of the Standard Model is charge conjugation, parity transformation, and time reversal (CPT) symmetry. Direct evidence for CPT violation can be searched for by comparing the quantum energy spectra of atoms with their antiatom counterparts. The search for CPT violation has led to the construction of the Antiproton Decelerator (AD) at CERN, and the creation and trapping of antihydrogen atoms for comparison with hydrogen, the simplest and best understood (both experimentally and theoretically) atom to date.

1.2 Physics with low energy antiprotons

Antiprotons are formed at CERN by firing a beam of protons from the Proton Synchrotron (PS) into a metal target. The proton beam has sufficient kinetic energy to create many secondary particles, including proton-antiproton pairs. As protons and antiprotons have opposite electrical charge, the antiprotons can be separated and steered away by strong magnetic fields.

Prior to the construction of the AD, antiprotons were produced and accumulated at the Antiproton Accumulation Complex (AAC). As well as serving high energy physics experiments at CERN, the AAC also supplied antiprotons to the Low Energy Antiproton Ring (LEAR) which explored the possibilities of making antihydrogen and capturing antiprotons within Penning traps – a type of charged particle trap which we will discuss in further detail in chapter 2.

1.2.1 The AD and ELENA

Constructed in 2000, the AD is capable of decelerating the injected antiproton beam down to 5.3 MeV. A combination of stochastic cooling and electron cooling are used to cool and increase the density of the antiprotons, and a short (~100 ns) bunch of around 3×10^7 antiprotons can be delivered to the experiments within the AD hall every ~2 minutes.

The ELENA (Extra-Low ENergy Antiproton) ring is a synchrotron with a circumference of just 30 m, and is reaching the final stages of commissioning. This decelerator is designed to reduce the energy of the AD beam to just 100 keV, and promises to increase the number of antiprotons which can be trapped by the experiments within the AD hall by a factor of between 10 and 100 [6]. Figure 1.1 shows an overview of the AD hall, with the location of the ELENA ring and the experimental zones highlighted.

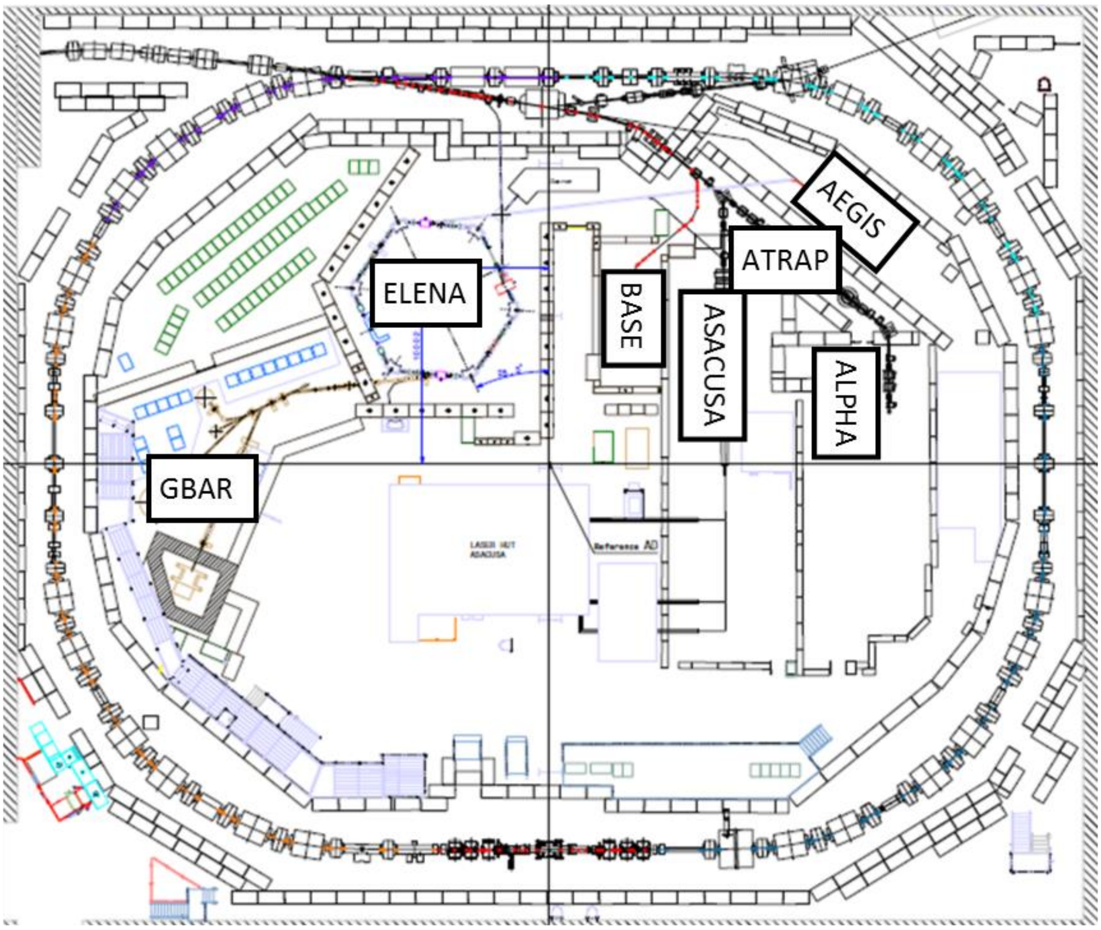

Figure 1.1: A schematic of the AD hall experiments in the 2017 run configuration. The ATRAP zone is on a platform above the surrounding experiments. ELENA and GBAR are still in the commissioning phase. The GBAR zone includes a shielded linear accelerator for positron production. Image adapted from [6].

1.2.2 Measurement of the antiproton-proton magnetic moment ratio

Both the ATRAP (Antihydrogen TRAP) and BASE (Baryon-Antibaryon Symmetry Experiment) collaborations have experiments dedicated to measuring the ratio between the proton and antiproton magnetic moment in a Penning trap. In 2013, ATRAP reported a measurement with a precision of 4.4 parts-per-million [7]. The BASE collaboration reported a 6-fold improvement in this measurement in 2016, with an uncertainty of just 0.8 parts-per-million, as well as outlining a new trapping technique which, when implemented in their next generation apparatus, could enable a measurement precision with an uncertainty at the level of a few parts-per-billion [8]. By using an isolated reservoir trap, BASE have also demonstrated the ability to hold a few tens of antiprotons for more than 1 year without any losses [9].

1.2.3 Measurement of the antiproton-electron mass ratio

The ASACUSA (Atomic Spectroscopy And Collisions Using Slow Antiprotons) collaboration measures the antiproton to electron mass ratio by ionising a helium atom and replacing the lost electron with an antiproton. Probing two-photon transitions in antiprotonic helium with high powered pulsed lasers has allowed the team to resolve the antiproton to electron mass ratio to better than 5 parts-per-billion [10].

1.2.4 Antihydrogen formation

Antihydrogen was first produced at the Low Energy Antiproton Ring at CERN in 1995 [11], and later at Fermilab [12]. Antiprotons were shot through a xenon gas target with a small chance to produce electron-positron pairs, and velocity matched positrons would bind with the antiprotons in the beam to form antihydrogen. However, these relativistic atoms were much too energetic to be suitable for detailed study. With the subsequent construction of the AD, a new generation of experiments were able to capture and cool antiprotons in Penning traps with the aim of producing much colder antihydrogen.

By mixing these antiprotons in a carefully controlled way with positrons accumulated in a Surko-type accumulator, cold antihydrogen was produced in 2002 by the ATHENA (AnTiHydrogEN Apparatus) [13], and ATRAP [14] collaborations. The dominant formation method at low temperatures is thought to be a three-body process, where two positrons scatter in close proximity to an antiproton. One positron carries away the excess energy of the other positron, which binds with the antiproton to form antihydrogen. However, these antihydrogen atoms would still annihilate on the walls of the Penning trap shortly after production, leaving little time for precision measurements. Confining the antihydrogen atoms in a magnetic trap was the next step for the ATRAP collaboration, along with ALPHA (Antihydrogen Laser PHysics Apparatus), a collaboration which succeeded ATHENA.

The ASACUSA collaboration aim to produce a beam of ground state antihydrogen atoms for measurements free from any significant magnetic field perturbations, and reported the first antihydrogen beam in 2014 [15]. ASACUSA uses a similar technique to ALPHA and ATRAP for antihydrogen synthesis, but does so in a cusp trap consisting of an anti-Helmholtz coil for beam formation.

The AEGIS (Antihydrogen Experiment: Gravity, Interferometry, Spectrometry) collaboration's approach to antihydrogen formation begins by shooting a beam of positrons at a micro structured target, on which some of the positrons bind with an electron to form positronium atoms. Positronium can be formed in two different states depending on the spin orientations of the positron and electron, and these states have individual lifetimes of 0.125 and 142 ns [16] before self-annihilating. However, the lifetime can be prolonged by using lasers to excite the positronium to a high Rydberg state. Theory suggests that Rydberg positronium should give more efficient production of antihydrogen atoms [17], and could result in colder antihydrogen than what is produced with the methods employed by ALPHA, ATRAP, and ASACUSA, as it allows the antihydrogen atom to form at the temperature of the antiproton.

GBAR (Gravitational Behaviour of Antihydrogen at Rest) is the newest collaboration in the AD hall, and is scheduled to be the first collaboration to use the beam from ELENA. By further cooling the ELENA beam and sending it through a very dense region of positronium, the collaboration plans to produce positive antihydrogen ions, which can be trapped and sympathetically cooled using laser cooled beryllium ions in a Paul trap. The conventional positron sources and accumulation techniques used by the other collaborations do not produce nearly enough positrons to achieve the required density of positronium for creating positive antihydrogen ions, so the team is installing a small linear accelerator for positron production which has been developed off-site.

1.3 Physics with antihydrogen

High precision comparisons between hydrogen and antihydrogen provide a sensitive test of CPT symmetry. As well as measurements of both optical and microwave spectroscopy transitions, there are other tests of CPT which can be examined, such as the charge neutrality of the atom. Another area of interest is the weak equivalence principle (a statement of the equality of gravitational and inertial mass), which can be tested by measuring the influence of gravity on antihydrogen atoms in free fall.

1.3.1 Magnetically trapping antihydrogen

Although antihydrogen is electrically neutral, the spin orientations of the antiproton and the positron form a dipole which causes the atom to seek a magnetic maximum or minimum. Both ALPHA and ATRAP developed magnetic minimum traps, where antihydrogen atoms that were cold enough would be confined radially by a cylindrical multipole magnet and prevented from escaping at the ends by short solenoids known as mirror coils. In November 2010 the ALPHA collaboration reported the first trapped atoms of antihydrogen [18], with ATRAP reporting similar success in 2012 [19]. By the end of 2011, the ALPHA collaboration had detected more than 300 trapped antihydrogen atoms, with as many as three trapped simultaneously and for up to 1000 seconds [20].

1.3.2 Tests of the weak equivalence principle

ALPHA's approach to testing the weak equivalence principle is to compare the ratio of the atoms which annihilated on the top and bottom halves of their trap. Any significant difference observed could be used to infer the gravitational mass of antihydrogen, and an analysis of the initial data was performed [21]. However, the geometry and systematic uncertainties of the ALPHA apparatus make it relatively insensitive to gravitational variations and unable to place any meaningful bounds without much colder antihydrogen. However, the technique was shown to be a viable method for a future specifically designed experiment, and work on a new apparatus has already begun. ALPHA-g is a vertically orientated version of the ALPHA apparatus, which is designed to look for the escape of antihydrogen atoms at either the top or bottom of the trap as the confining magnetic fields are slowly ramped down.

AEGIS's approach to testing the weak equivalence principle is to produce a horizontally travelling beam of cold antihydrogen atoms that will be sent through a moiré deflectometer, which will measure the drop of atoms of different velocities with respect to an optical interference pattern.

Finally, the GBAR collaboration's trapped and cooled antihydrogen ions will be photo-ionised, and the now neutral antihydrogen will be in free-fall within their detector.

1.3.3 Measuring the charge neutrality of antihydrogen

Similar to how the gravitational measurement was conducted, the ALPHA collaboration searched for a left/right bias in the annihilation locations within their trap as it was shut down under the influence of a strong electrostatic gradient. This technique was used to place an experimental limit on the charge of antihydrogen in 2014 [22]. This bound was improved by a factor of 20 in 2015 when stochastic acceleration [23] was applied to the trapped antihydrogen atoms in an attempt to kick them out of the trap, determining the charge of antihydrogen to equal zero to 0.71 parts-per-billion (one standard deviation) [24].

1.3.4 Microwave spectroscopy of antihydrogen

The Zeeman Effect causes a splitting of the energy levels of atoms under the influence of a magnetic field. Figure 1.2 is the Breit-Rabi diagram which shows the hyperfine splitting of the ground state of hydrogen.

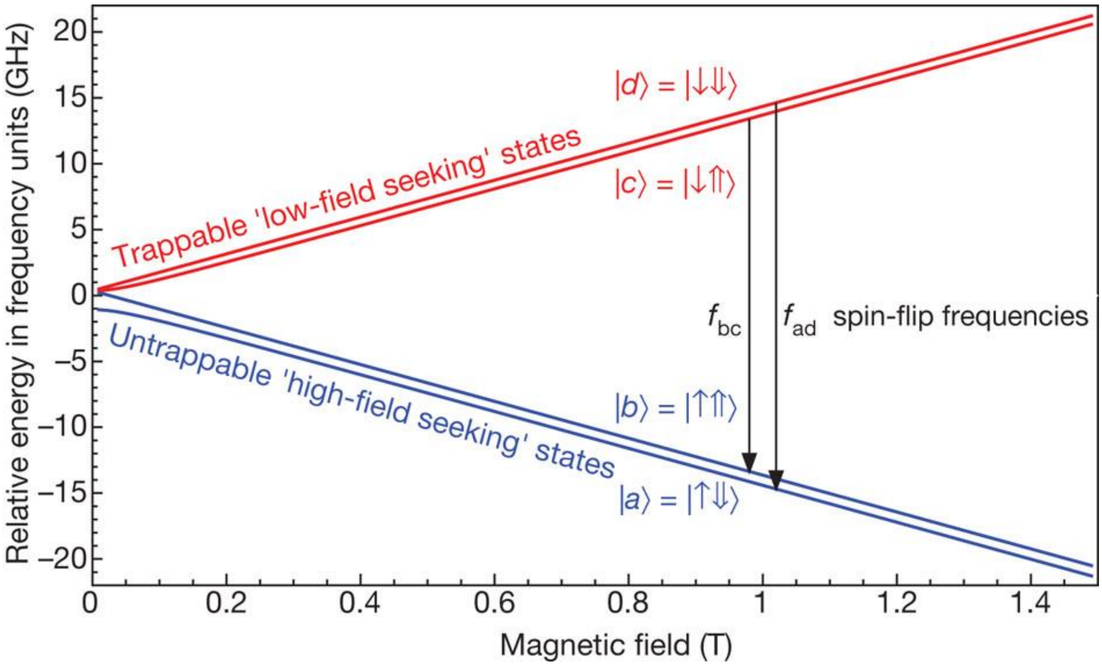

Figure 1.2: A Breit-Rabi diagram showing the Zeeman splitting of the (anti)hydrogen ground state. The ALPHA collaboration injected resonant microwaves (shown by the black arrows) into the 1 T magnetic trap, and observed a spin flip of the positron (single arrow) which caused the atoms to seek a high magnetic field and annihilate on the walls of the trap. Image from [25].

In 2012, the ALPHA collaboration observed the first resonant quantum transitions in antihydrogen [25] by exciting the ground state hyperfine splitting transitions in a 1T magnetic field. When tuned on resonance, the microwaves caused the spin state of the positron to flip from a low-field seeking state to a high-field seeking state, and the atoms would travel towards and annihilate on the walls of the trap.

ASACUSA plan to improve on this measurement by using a beam of antihydrogen atoms to measure the ground state hyperfine splitting in a region free of strong magnetic gradients in the near future.

1.3.5 Laser spectroscopy of antihydrogen

Laser spectroscopy of antihydrogen was one of the key motivations for the construction of the AD [26], and it marks the next step towards studying antihydrogen in detail. Spectroscopic measurements of hydrogen have inspired many of the quantum and field theory developments we have today, and the hydrogen atom is still a major source of study for many ongoing experiments.

With a natural linewidth of only 1.3 Hz, the 1S-2S transition in atomic hydrogen provides one of the most sensitive measurements of several fundamental physical constants, and the high level of experimental precision possible pushes for more precise calculations of QED and field theories. As such, a comparison between the 1S-2S transition in hydrogen and antihydrogen would constitute an extremely sensitive test of CPT symmetry. The precise measurement of the antihydrogen 1S-2S transition frequency is one of the primary goals of the ALPHA collaboration.

Also of interest is the 121.5 nm Lyman-α transition between the 1S and 2P states. Whilst the transition is relatively broad, it could potentially be used to laser cool antihydrogen, which would push the precision of other measurements. Both the ALPHA and ATRAP collaborations are developing lasers towards this effort.

2 Antihydrogen production in the ALPHA apparatus

2.1 The apparatus

The ALPHA apparatus (upgraded from ALPHA-1 to ALPHA-2 in 2012) consists of a catching trap (CT) for capturing and cooling antiprotons from the AD beam, a positron accumulator for collecting and cooling positrons emitted from a ^{22}Na source, and an atom trap (AT) for precision manipulation of the antiproton and positron plasmas and the formation and trapping of antihydrogen. In addition, two vertical translators, or “sticks”, are used to position instruments for loading electrons into the traps and diagnosing particles ejected from the traps. The ALPHA beamline is shown in Figure 2.1.

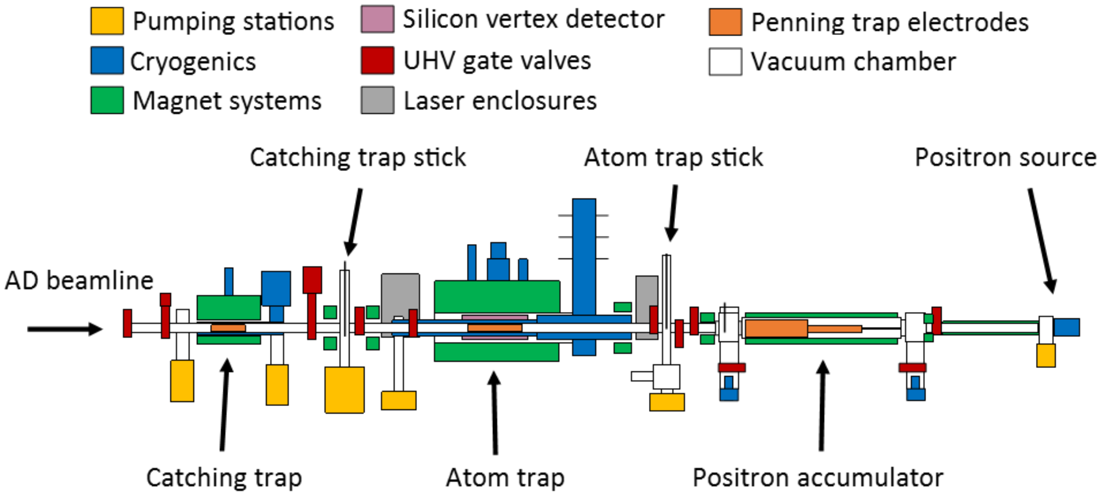
Pumping stations
Cryogenics
Magnet systems
Silicon vertex detector
UHV gate valves
Laser enclosures
Penning trap electrodes
Vacuum chamber
Catching trap stick
Atom trap stick
Positron source
AD beamline
Catching trap
Atom trap
Positron accumulator

Figure 2.1: An overview of the ALPHA beamline. Antiprotons are captured in the 3 T field of the CT and cooled using electrons loaded from the CT stick. Meanwhile, positrons are accumulated in a 3-stage Surko-type accumulator. After initial preparations, both species antiprotons and positrons are transferred into the AT for antihydrogen production and trapping. Small solenoids are positioned along the beamline to aid the transfer of particles. The distance between the CT and AT is approximately 3 m.

The storage time of antiparticles is directly related to the quality of the vacuum, as the antiparticles will annihilate with background gas particles. To achieve an ultra-high vacuum (UHV), the individual sections of the beamline must be baked to between 80 and 120 °C whilst being pumped by turbo molecular pumps, before being closed off to the outside world and pumped by a combination of ion pumps and titanium sublimation pumps. The room temperature sections of the beamline typically achieve a vacuum below 10^{-9} mbar, whilst the cryogenic CT and AT can achieve a vacuum below 10^{-12} mbar, yielding antiproton lifetimes longer than 10,000 s.

The ALPHA-2 upgrade allows optical access to the AT via four paths which cross the central trap axis at an angle of 2.3° (shown in Figure 2.8), for the introduction of 121 and 243 nm light for antihydrogen spectroscopy. Precision mounting structures at the ends of the magnet form enable the installation of two 90 cm Fabry-Pérot cavities in the UHV, cryogenic region, which we will discuss in detail in chapter 4. The access windows at the ends of the vacuum chamber are within the laser enclosures shown in Figure 2.1 and are separated by 2.7 m.

In the context of the ALPHA apparatus, the terms “upstream” and “downstream” are used throughout to relate the apparatus to the direction which the antiproton beam enters. The most upstream point of the beamline is the catching trap degrader, and the most downstream point is the positron source. 243 nm light is injected into the enhancement cavity at the upstream end of the AT. Where applicable, images are orientated so that the antiproton beam enters from the left side.

2.1.1 Penning traps

The CT, AT, and positron accumulator all contain a variant of a Penning trap. Penning traps are composed of a set of at least three electrodes within a homogenous axial magnetic field, such as the central region of a solenoid. The magnetic field confines charged particles radially, and a static electric potential provided by the electrodes confines oppositely charged particles axially. In an ideal trap, the electrodes are either hyperbolically shaped, or have hyperbolic end-caps to produce a perfectly quadratic electric field. However, simpler electrode structures such as the stacked cylinders of Figure 2.2 still form functional traps. These so-called Penning-Malmberg traps are used by ALPHA as the shaped electrode design would take up more radial space and reduce the depth of the magnetic trap, whilst the end-cap design would make it much more technically challenging to load particles into the trap.

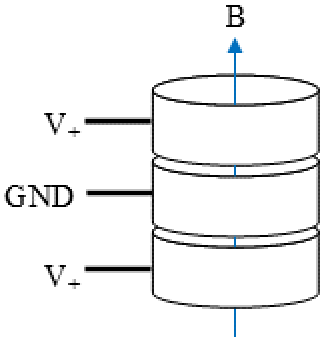

Figure 2.2: A simple Penning-Malmberg trap constructed from three stacked cylindrical electrodes.

The movement of charged particles within a Penning trap is described by the Lorentz force;

$$F = q(\boldsymbol{E} + \mathbf{v} \times \boldsymbol{B})\,, \tag{2.1}$$

where q is the charge of the particle, $\mathbf{v}$ is its velocity, and $\boldsymbol{E}$ and $\boldsymbol{B}$ are the electric and magnetic fields respectively. In a perfect Penning trap, the axial motion is decoupled from the radial motion and undergoes simple harmonic motion within the confining electric potential. The radial motion consists of a high frequency solution known as the (modified) cyclotron frequency, and a slower drift around the trap axis known as the magnetron frequency. Note that the emission of cyclotron radiation is the dominant source of cooling for electron and positron plasmas in a strong magnetic field. Removing energy from the magnetron motion (e.g. by collisions with background gas) causes the orbit to increase, and is the dominant source of loss from a trap which is not operated under UHV conditions. The radiative loss associated with the magnetron frequency is low enough that the motion is otherwise stable for many years [27]. Figure 2.3 shows the combined motion within a Penning trap.

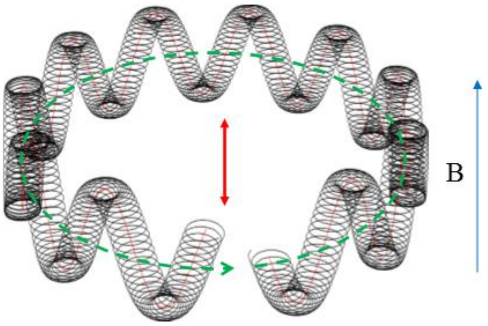

Figure 2.3: The motion of a single particle in a Penning trap is described by a combination of the magnetron (green), cyclotron (black), and axial motion (red). The image is adapted from [28].

2.1.2 Catching trap

The CT is a cryogenic Penning-Malmberg trap consisting of an electrode stack within a 3 T external solenoid field. The electrodes are overlapping, but electrically isolated from each other using ruby balls, and the outer diameter of the electrode stack is wrapped in Kapton to isolate it from the surrounding cryostat. The 5.3 MeV antiproton beam from the AD is extracted and steered into the ALPHA zone using a series of dipole magnets, and focussed onto a layered Al/Be foil degrader at the nose of the catching trap using a pair of quadrupole magnets. The degrader also separates the ALPHA beamline vacuum from the vacuum of the AD. A small fraction of the beam passing through the degrader has a low enough energy to be trapped between two specialised 5 kV electrodes labelled HVA and HVB in Figure 2.4. HVB is energised in advance, and a fast amplifier triggered at the arrival of the beam energises HVA to close the trap. The trapped antiprotons are then sympathetically cooled by collisions with electrons pre-loaded into the trap from the CT stick, and transferred into a six-segmented electrode (RW1).

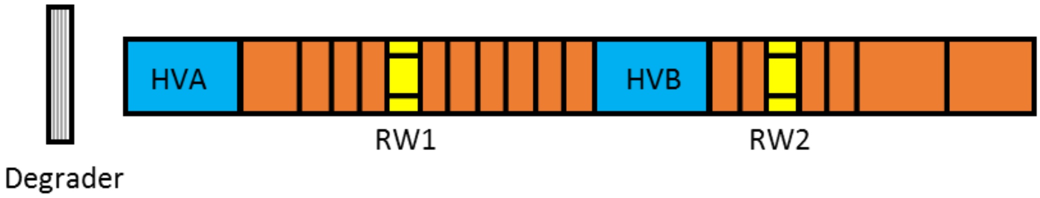

Figure 2.4: A sketch of the catching trap electrode stack. The trap has a length of 396 mm and an inner diameter of 29.6 mm. The two high voltage electrodes are shown in blue and the segmented electrodes used for plasma compression are shown in yellow. An external solenoid provides a 3 T field to complete the Penning trap. The antiproton beam enters from the left of the image.

A high frequency sinusoidal electric field with a phase difference of 60° between neighbouring electrode segments is used to apply a torque to the combined antiproton-electron plasma to compress it using a technique known as ‘rotating wall’ compression [29]. This technique also heats the plasma, so electrons are required throughout to sympathetically cool the antiprotons. Lowering one side of the confining potential in the Penning trap for 75 ns allows the lighter electrons to escape, whilst retaining the majority of the heavier antiprotons. After several stages of rotating wall compression and electron removal, a pure antiproton plasma containing between 10^5 and 10^6

particles with a temperature of a few hundred Kelvin is ready to be transferred across to the AT. Figure 2.5 shows images of the antiproton and electron plasmas at various stages of the preparation cycle, generated by ejecting the plasma towards a multichannel plate (MCP) mounted on the catching trap stick (which we will discuss in more detail in section 2.2.4). Multiple shots from the AD can be stacked to capture additional antiprotons.

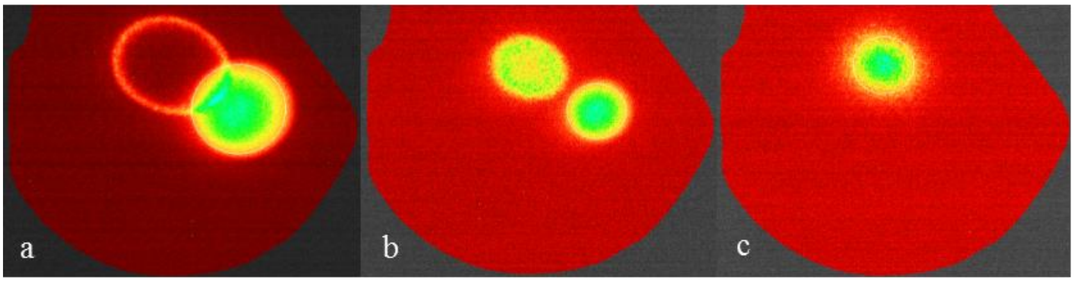

Figure 2.5: a) After an initial stage of rotating wall compression, the antiprotons (left) and the electrons (right) are centrifugally separated [30]. b) Kicking out 90% of the electrons allows the antiprotons to be compressed further. c) Finally, the remaining electrons are kicked out and the antiprotons are ready for transfer. The two species map to different locations on the MCP due to a small misalignment between the electrode stack and the magnetic field.

2.1.3 Positron accumulator

Positrons are emitted via β^+ decay from a ^{22}Na source mounted to a coldhead (shown in blue in Figure 2.6). The source is cooled to 5 K, and a solid Ne moderator film is grown over the surface as gas which is allowed into the chamber condenses. This reduces the emission energy of the positron to around 50 eV meaning the can readily be formed into a beam. The positrons are guided into a Surko-type accumulator [31], which employs a nitrogen buffer gas cooling technique to slow down and trap the positrons within a three stage Penning-Malmberg trap [32]. The accumulator is differentially pumped from both ends so that the hotter positrons in the first stage have more interaction with the nitrogen gas than the cooler positrons in the third stage (see Figure 2.7). A six-segment rotating wall electrode in the third stage is used to compress the positron cloud.

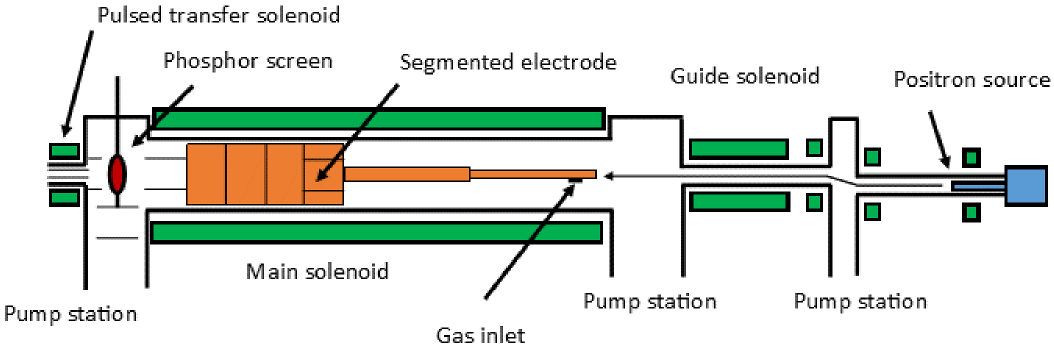
Pulsed transfer solenoid
Phosphor screen
Segmented electrode
Guide solenoid
Positron source
Main solenoid
Pump station
Gas inlet
Pump station
Pump station

Figure 2.6: A schematic of the positron accumulator. Positrons are emitted from a 5 Kelvin ^{22}Na source (blue) and accumulated in a three stage Penning-Malmberg trap (orange). The accumulator is equipped with a small vertical translator containing a phosphor screen (red) for imaging the positrons and a grounded pass-through tube. The image is adapted from [33].

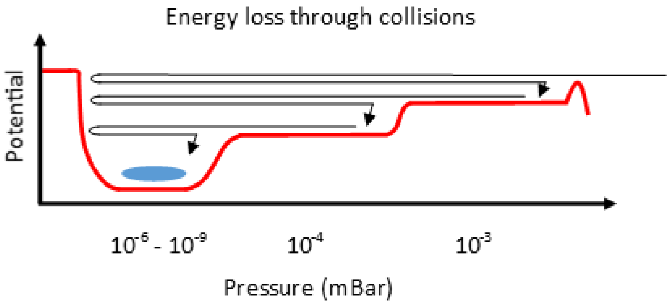
Energy loss through collisions
Potential
10^{-6} - 10^{-9}
10^{-4}
10^{-3}
Pressure (mBar)

Figure 2.7: The high energy positrons are cooled by interacting with a nitrogen buffer gas within the electrodes. The accumulator is differentially pumped such that the cooling interactions are strongest in the first stage (right hand side of graph) and the lifetime is prolonged in the third stage (left hand side of graph). The image is adapted from [33].

After 150 s, the accumulator reaches a saturation point with around 50 million trapped positrons. The rotating wall compression is run continuously, so at this point the accumulator can be thought of as an on-demand positron reservoir. Before ejecting the positrons towards the atom trap, the nitrogen buffer gas is pumped out to reach a vacuum of 10^{-8} mBar. The positrons are transferred through a 100 mm long tube with a narrow pumping restriction, and a 1.2 T solenoid which covers the length of the tube is pulsed to prevent the positrons annihilating on the wall. CsI diode detectors are placed in various locations around the apparatus to identify and quantify positron losses by detecting the 511 keV gamma rays emitted by electron-positron annihilation.

2.1.4 Atom trap

The AT (shown in Figure 2.8) consists of a Penning-Malmberg electrostatic trap nested within a Ioffe-Pritchard magnetic minimum trap. Not pictured is the 1 T external solenoid, which provides the magnetic field for the Penning-Malmberg trap. The magnetic trap is composed of a superconducting octupole magnet for radial confinement, and a set of short solenoids known as mirror coils (labelled A-E in Figure 2.8) for axial confinement. The five mirrors allow for a flatter central field, as well as the realisation of more complex well shapes compared to the original ALPHA apparatus which only had mirrors in locations A and E. The design trap depth is 1.16 T [34], which corresponds to a peak trappable antihydrogen temperature of 0.78 K. In practice, the octupole only runs at 70% of the design current, reducing the well depth to 0.54 K.

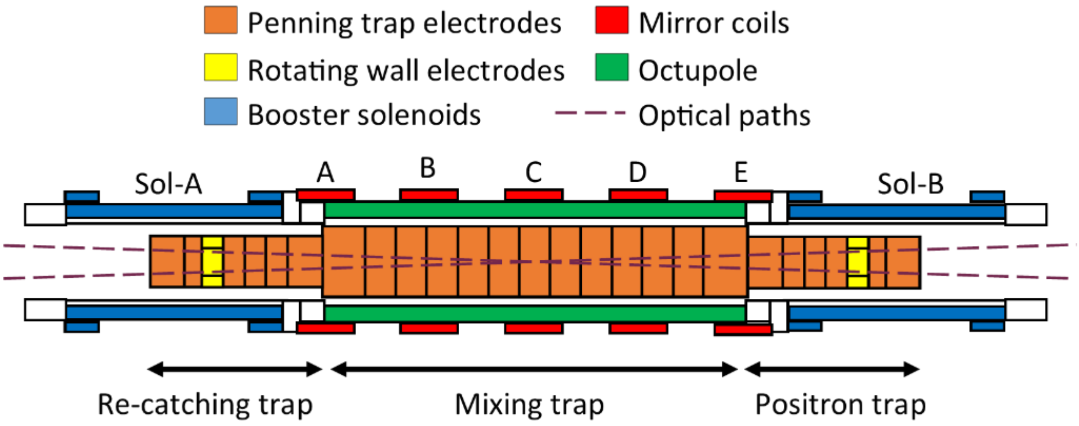

Figure 2.8: A schematic of the nested Penning-Malmberg and Ioffe-Pritchard traps within the ALPHA-2 atom trap. The antiprotons are transferred in from the left hand side and the positrons are transferred in from the right hand side of the image. The electrodes are in the UHV space, whereas the magnets are in direct contact with liquid helium. An outer vacuum chamber and a layer of super-insulation reduce the heat load on the cryostat. Not shown is an external 1T solenoid.

The Penning-Malmberg trap is separated into three independently controllable regions nicknamed the re-catching, mixing, and positron traps. The re-catching trap functions to catch and further cool the antiprotons transferred over from the CT. Electrons loaded from the AT stick are used to sympathetically cool the antiproton plasma in a second round of rotating wall compression and cooling, and the end result is a dense plasma with a temperature of 70 K. The positron trap is a mirror of the re-catching trap, and is used to catch and compress the positrons from the accumulator. Both of these traps have a six-segment electrode for rotating wall compression, and a booster solenoid which locally raises the magnetic field to 3 T for more effective cyclotron cooling of leptons. The mixing trap electrodes are much thinner to allow antihydrogen atoms to approach closer to the octupole, maximising the neutral trap depth. The antiprotons and positrons are brought almost simultaneously into the centre of the mixing trap to adjacent electrostatic wells. The wells are reduced slightly to evaporatively cool the antiprotons to 50 K and the positrons to below 20 K [35], and the two species of particle are now ready to be mixed to form cold, trappable antihydrogen.

2.1.5 Sequencing and data acquisition

A set of FPGA-based sequencers are used to maintain the timing and reproducibility of experiments. The sequencers are equipped with National Instruments (NI) PXI-6733 cards to control the Penning trap voltages and an NI PXI-7811R card for communicating with external hardware using TTL logic. A frontend created using NI LabVIEW allows an experimental sequence to be written by generating a set of ‘states’. A state can include a voltage change of the Penning trap electrodes or a trigger to/from an external device. The sequencers maintain the timing of states to within 500 ps, and will respond to external triggers with a timing jitter of approximately 100 ns. This allows for complex operations to be performed simultaneously and with a high level of reproducibility.

2.2 Tools and diagnostics

2.2.1 Sticks

Two vertical translators, or ‘sticks’ (locations shown in Figure 2.1), are used to position various pieces of essential hardware onto the ALPHA beamline. The CT stick carries an electron gun and an MCP which face the CT, and a Faraday cup which faces the AT, whilst the AT stick carries an electron gun and an MCP, both of which face the AT. Both sticks also carry a pass-through electrode for particle transfer. The sticks are driven by stepper motors, and use a laser range-finder to consistently position the instruments on the beamline.

2.2.2 Electron gun

Electrons are essential for sympathetically cooling antiprotons via their short cooling time in a strong magnetic field (0.4 s at 3 T) by the emission of cyclotron radiation. The electron guns consist of a thermionically emitting barium oxide filament and an accelerating plate. The resulting electron beam is guided into the Penning-Malmberg traps by the axial magnetic fields generated by several transfer magnets.

2.2.3 Faraday cup

A Faraday cup is a simple piece of conducting material with a known capacitance. Electrons and positrons dumped to a Faraday cup will generate a voltage, which can be converted to the amount of charge collected, and thus the number of particles. Using an SRS SR560 amplifier, a resolution of around 2×10^5 particles can be achieved. A Faraday cup is mounted to the CT stick and faces towards the AT, whilst the CT degrader functions as a Faraday cup for diagnostics from the CT.

2.2.4 Multichannel plate

The MCP devices used on the catching trap and atom trap sticks are manufactured by PHOTONIS, and consist of a single layer MCP, a P45 phosphor screen, and a 45° mirror for reflecting the light from the phosphor. Plasmas trapped in the Penning-Malmberg traps can be imaged by manipulating the trapping potentials to eject them towards an MCP. The front surface of the MCP can be biased with either a positive voltage to accelerate electrons and antiprotons towards it, or negative voltage to accelerate positrons towards it.

Particles hitting the channels produce a shower of electrons, with a gain of between 10^4 and 10^6 depending on the bias voltage across the plate. The bias voltage is typically between 400 and 900 V, and is chosen to avoid saturation. The electron shower is then accelerated towards the phosphor screen by a 4 kV potential difference, and the spatial distribution of the plasma can be reconstructed by imaging the phosphor screen using a CCD camera looking through a vacuum viewport [36].

The MCP can be used to calibrate the number of leptons by measuring the charge drawn away from the front surface. However, calibrating the number of antiprotons is more difficult as they will annihilate upon impact with the MCP, and the products of the annihilation can trigger electron emission in other channels, drawing away more charge than a proton collision would. Instead, scintillator panels (which we will discuss in section 2.2.6) are placed close to the MCP to count the antiproton annihilation events.

2.2.5 Flappers

The atom trap contains two beamline shutters, or ‘flappers’, which are heat sunk in their respective ends of the AT cryostat. When closed, these prevent black body radiation from the room temperature parts of the beamline entering the trap. The flappers use a small coil to open and close within the field from the external 1 T solenoid. Note that the flappers were not used in this work, as they are still in the final stages of testing, and it was deemed too risky to run them during the antiproton beam periods because the atom trap would have to be aired up if one was to get stuck in the closed position.

2.2.6 Scintillator panels

To detect antiproton annihilations, scintillator panels are placed in key locations around the ALPHA apparatus. As particles pass through a scintillating material, the material emits a small amount of light which can be detected by a photo multiplier tube (PMT). The panels are paired and read out in coincidence to reduce the dark noise of the PMTs, and pairs positioned on both sides of the catching trap and atom trap (shown in Figure 2.9) can further improve the signal to noise ratio by using coincidence to reject cosmic events. The scintillators are useful for measuring the antiproton lifetime, as well as counting the number of annihilations when the antiproton plasma is dumped to a solid surface.

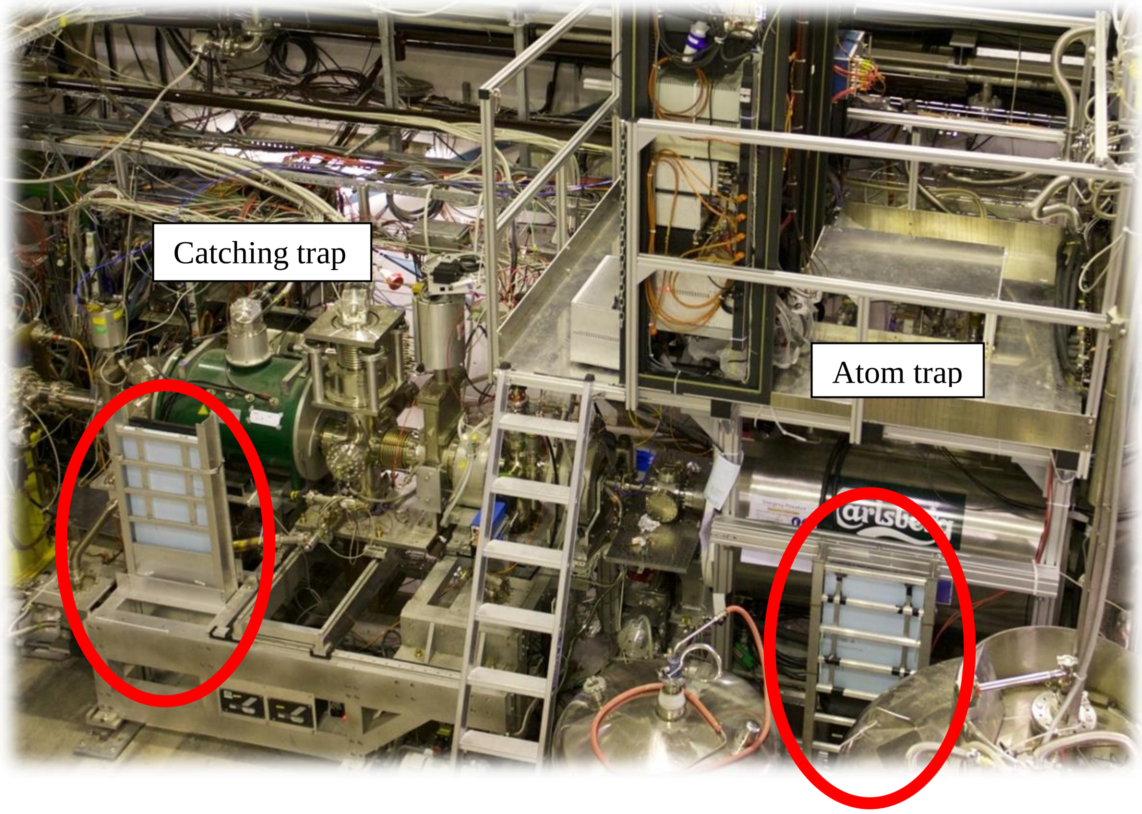

Figure 2.9: The locations of the scintillator panels are highlighted on the CT (left) and AT (right). The scintillators are positioned in pairs either side of the solenoids. Portable scintillator pairs are positioned next to the diagnostic sticks when additional information about the annihilation position is needed.

2.2.7 Silicon vertex detector

Antiproton annihilations result in typically 3-5 unstable pions being emitted, but there can in theory be as many as 13 [37]. These secondary particles travel at a reasonable fraction of the speed of light and can either interact with other material or decay naturally at a rate given by their lifetime. ALPHA uses a silicon vertex detector to detect and reconstruct the paths of these pions and their by-products to identify the point of antiproton/antihydrogen annihilation [38]. The detector consists of three layers of position sensitive silicon strips (shown end-on in Figure 2.10). As particles pass through the silicon they deposit a small amount of charge, which registers as a hit. If all three of the layers register hits, then a vertex can be traced out, taking into account any potential curvature from the magnetic field. If two or more vertices cross on or within the electrode walls, then the event is recorded as an antiproton annihilation, whilst vertices beyond the electrodes are recorded as cosmic events.

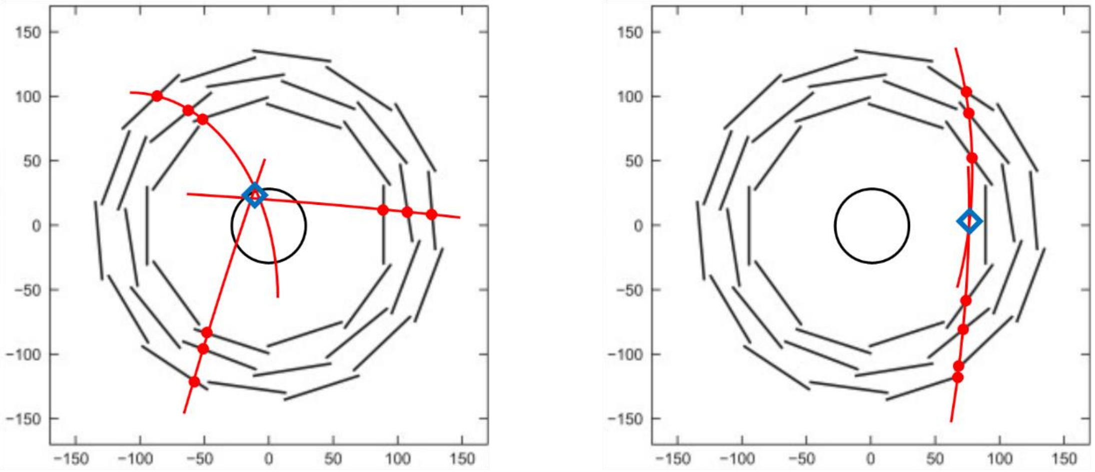

Figure 2.10: An example reconstruction of an antiproton annihilation (left) and a cosmic ray event (right). The blue diamond indicates the position of the reconstructed annihilation event, the red dots the positions of the detected hits, and the inner circle shows the radius of the Penning trap electrodes. Image adapted from [39].

The typical online analysis used to detect the annihilations based on the methods described above has a detection efficiency of 63.4% and a false-positive rate of 48.8 mHz, which can be reduced by limiting the search to specific parts of the trap. An offline multivariate analysis (MVA) allows a high degree of tuning of the background rate at the cost of detection efficiency (as demonstrated in Figure 2.11). The MVA is trained on annihilation events during the mixing process, and cosmic runs where no antiprotons or positrons were present in the apparatus.

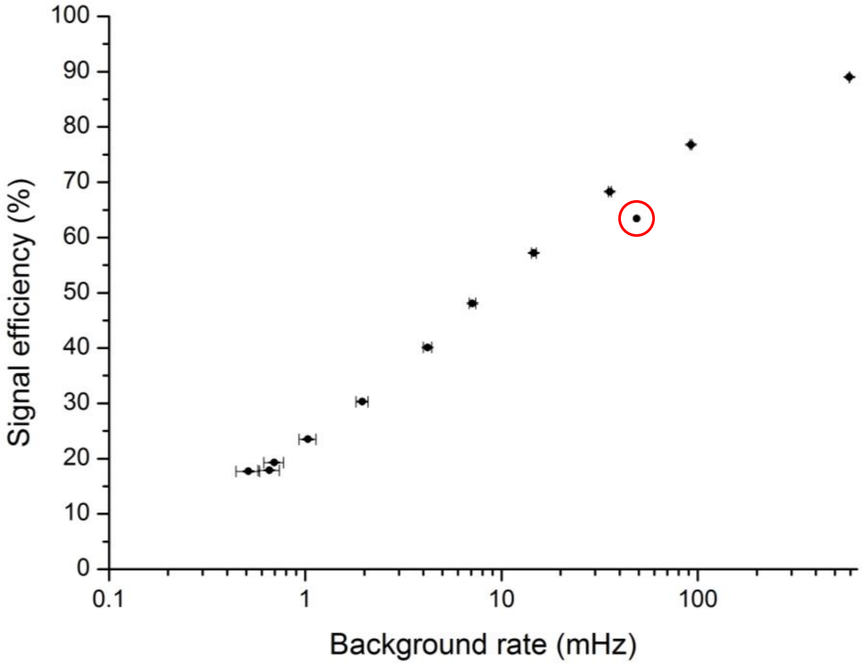

Figure 2.11: A plot of the detection efficiency against the accepted background rate for the MVA analysis. For reference, the performance of the standard online analysis is circled in red. The data displayed is from around 670 mixing cycles and 82 hours of cosmic data from 2014. The Y-axis error bars are negligible.

2.2.8 Temperature diagnostics

We have discussed the temperature of the plasmas held within the Penning traps without yet quantifying how they were measured. The temperature of a plasma can be diagnosed by directly sampling the energy distribution. This is done by measuring the charge that escapes when one side of the confining potential well is lowered and the particles are extracted to the MCP front. Although antiprotons can also be extracted to the MCP, as we discussed earlier a better signal can be attained by detecting the annihilations using the scintillator panels instead.

For a plasma in equilibrium, it has been demonstrated [40] that the number of particles (N) with charge (q) that escape the trap is approximately related to the change in the confining potential (V_c) by

$$\frac{\partial \ln(N)}{\partial V_c} \approx -\frac{|q|}{k_B T}, \tag{2.2}$$

where k_B is the Boltzmann constant and T is the plasma temperature. The equation is approximate for two reasons: Firstly, the approximation is only valid for the very first, highest energy particles to escape from the potential well, as the change in space charge of the remaining particles is neglected. Secondly, the manipulation of the potentials required to extract the plasmas necessarily change the shape of the well, causing the plasma to lengthen and adiabatically cool. The expected influence of these two factors can be numerically calculated and used to correct the measured plasma temperature. By incorporating these corrections, it has been demonstrated that the temperature of the plasma can be determined to within 20% [34]. However, this method has never been calibrated by ALPHA in an absolute sense.

2.2.9 Magnetometry

The magnetic field of the CT, AT, and positron accumulator are continuously monitored using Hall probes. However, for experiments such as the 1S-2S transition measurement, a more precise measurement is needed in the AT. This can be achieved by measuring the electron cyclotron resonance (ECR), which is the circular movement of an electron in a static and uniform magnetic field due to the Lorentz force. The frequency of this motion (f_{ECR}) is related to the magnetic field B by the equation

$$f_{ECR} = \frac{eB}{m}, \tag{2.3}$$

where e is the charge and m is the mass of the electron.

An electron plasma containing around 40 million particles with a diameter of 1.5 – 3 mm is loaded into a single electrode. Microwave pulses are then injected into the trap via a waveguide situated behind the downstream flapper, and the electric fields associated with these pulses heat the electron plasma when the frequency of the microwave radiation matches the electron cyclotron frequency [34]. Typical measurements inject a microwave pulse only every 15 seconds to allow the plasma to cool to its equilibrium temperature between each pulse. The temperature change can be inferred by monitoring the vibrational modes of the plasma. The quadrupole vibrational mode of the plasma is excited by applying high frequency Gaussian noise to a neighbouring electrode (typically centred around 25 MHz), and the response of the plasma is measured on the confining electrode through a high pass filter. This frequency increases in a manner which is approximately linearly proportional to the temperature of the plasma [41]. Figure 2.12 shows a trace of an ECR line shape which was taken during the 2016 run. The peak of the line shape is resolvable to around 10 MHz, which corresponds to a magnetic field accuracy of ± 0.5 mT. The technique is detailed in [42].

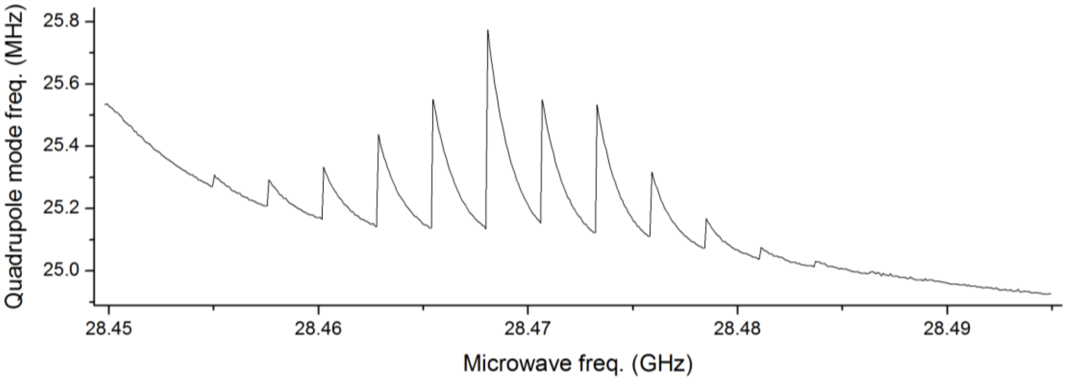

Figure 2.12: An example of an ECR line shape recorded during the 2016 beam period. The trace shows the quadrupole vibrational mode frequency of an electron plasma when excited by microwave pulses of increasing frequency.

2.3 Antihydrogen formation and trapping

The formation of antihydrogen by mixing antiprotons and positrons has been relatively routine since the early ATHENA and ATRAP experiments, but the formation of antihydrogen with a low enough kinetic energy to be confined by the magnetic trap is a much more difficult endeavour. Antihydrogen is thought to be created by a three-body recombination process where a ‘spectator’ positron carries away the excess energy of the ‘active’ positron – antiproton pair [43]. It is therefore beneficial to have the positron plasma as cold and dense as possible during the mixing process to maximise the three-body recombination cross section. In this section, we will discuss two different methods that have been employed to make cold, trappable antihydrogen, as well as a technique for bringing additional antiprotons and positrons into the trap for further antihydrogen production and antihydrogen accumulation. The silicon vertex detector has been (and remains) an essential tool for analysing and tuning the antihydrogen production techniques.

2.3.1 Autoresonant mixing

Autoresonance is an effect which has been observed in a variety of non-linear oscillators, including plasma modes [44]. When a swept frequency drive is applied to a non-linear oscillator whose frequency varies with its amplitude, the response can become phase-locked to the drive [45]. This technique can be applied to the antiproton plasma to gradually excite it into the positron plasma whilst being largely independent of the initial conditions of the positrons and antiprotons [34]. The antiproton bounce frequencies are typically too low for the autoresonant drive to have a direct effect on the positrons, however, the positrons are observed to heat from 20 K to around 50 K after antiproton injection is finished. Increasing the number of antiprotons would increase the positron heating, and result in a lower trapping rate. Autoresonant excitation was used up until the 2016 beam period and yielded a peak trapping rate of 2 atoms per trial and a maximum of 4 atoms detected within the trap simultaneously (using the standard online analysis method with a detection efficiency of 63.4%).

2.3.2 Slow merge mixing

During the 2016 run, an older mixing technique was revisited which lead to a trapping rate of 10.5±0.6 atoms per trial using an MVA analysis tuned to give a efficiency of 73.0±0.4%. In this scheme, the positron and antiproton electrostatic wells are slowly merged over 1 s, effectively allowing the two species to flow into each other. The positron plasma evaporatively cools to below 20 K during the merge, and increasing the antiproton number doesn't have the same adverse heating effect as it did during autoresonant mixing. This technique is potentially more sensitive to the initial plasma conditions, but the use of evaporative cooling during the earlier rotating wall compression stages allowed the plasmas to be prepared with a high degree of consistency [46]. A fraction of the positron plasma is retained after the mixing step for temperature diagnostics and sanity checks. Figure 2.13 shows a comparison of the autoresonant and slow merge mixing techniques.

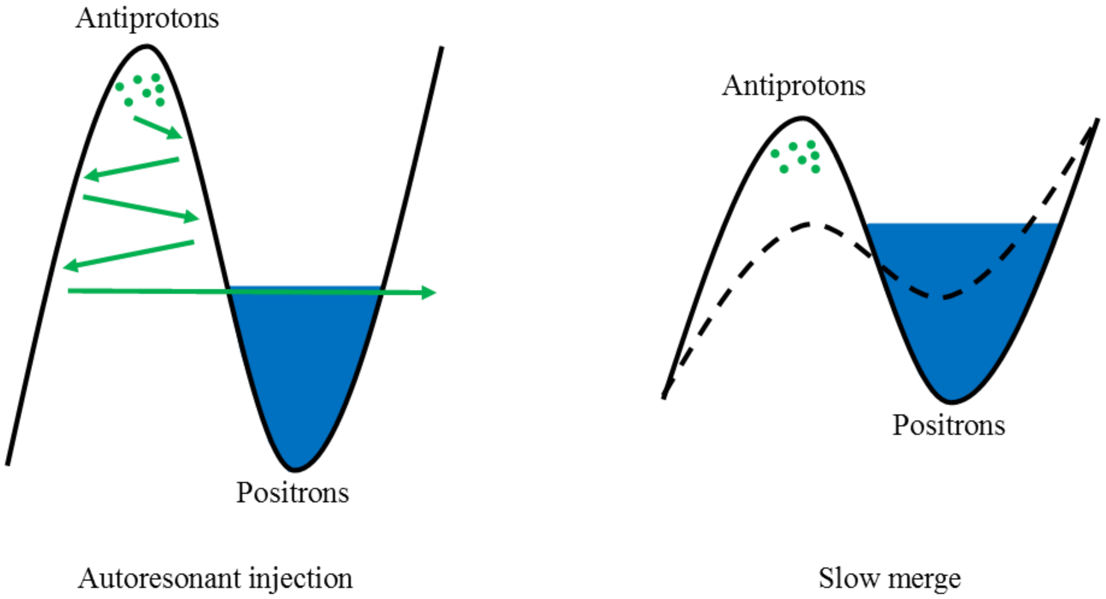

Figure 2.13: In the autoresonant scheme (left), the antiprotons are excited into the positrons by a chirped frequency. In the slow merge scheme (right), the initial wells (solid line) are reduced until the two species spill into each other (dashed line).

2.3.3 Antihydrogen accumulation

In 2016, the possibility of bringing additional batches of antiprotons and positrons into the neutral trap without first ramping down the trap magnets to repeat the mixing process and accumulate, or “stack”, additional antihydrogen atoms was investigated. The octupole field distorts the solenoid field of the Penning-Malmberg trap, which will guide particles towards the walls. The critical radius at which particles will be lost in this circumstance has been calculated [47] to be approximately 4.5 mm, which is significantly larger than the sub-mm radii of the electron, positron and antiproton plasmas typically used in ALPHA. Electrons used to cool the antiprotons are normally loaded directly into the re-catching trap from an electron gun on the AT stick. However, as this loading beam must pass through the mixing trap, it has the potential to ionise the trapped antihydrogen atoms. To reduce the likelihood of this, the electrons are instead loaded into the positron trap before being quickly shuffled by electrostatic potentials through the mixing trap and into the re-catching trap.

Preliminary trials, mixing between one and five successive stacks of positrons and antiprotons, showed that the number of antihydrogen atoms within the trap increased linearly with each successive mixing cycle (see Figure 2.14). The linear relationship suggests that no antihydrogen atoms are lost during the transfer of plasmas through the magnetic trap. Each stack of antihydrogen takes approximately 4 minutes to produce, meaning that the first stack has been trapped for as long as 16 minutes. The five stack experiment was only performed once and yielded a record 54 detected atoms, implying that around 74 atoms were trapped simultaneously when accounting for the detection efficiency of 73.0±0.4%. It was not possible to investigate higher numbers of stacks at this time due to temperature considerations of the octupole magnet power supply circuit.

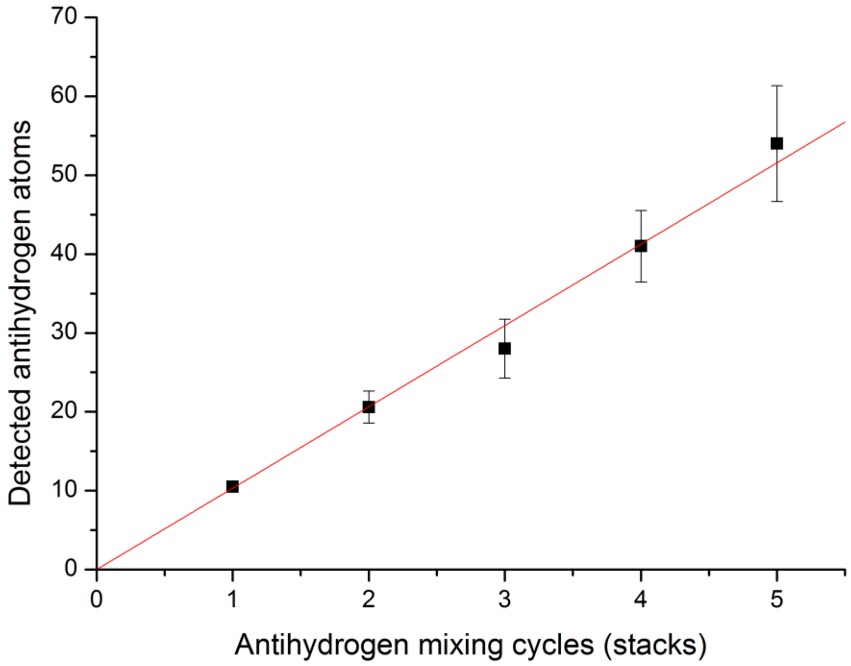

Figure 2.14: The number of trapped atoms increases linearly with each successive mixing cycle. The error bars show the $\sqrt{N}$ *counting statistics alone. The detection efficiency is 73.0±0.4%.*

2.4 Antihydrogen detection

There are not currently any non-destructive methods of detecting trapped antihydrogen, so we must instead turn off the trap and look for the annihilation of any atoms which were trapped. This can either be done by intentionally triggering the quench response of the magnets, or by ramping down the power supplies as fast as possible without triggering the quench response.

Triggering the quench response will shut down the magnets with a 1/e time constant of 9.5 ms [34]. To avoid damaging the magnets or generating excess heat in the cryostat, the current is extracted through a series of external resistors which are connected by an insulated-gate bipolar transistor (IGBT) when the control system detects a voltage across the magnets [34]. The quench response can be manually triggered, giving the 9.5 ms shutdown that is fast enough that there are essentially no false-positive events due to the cosmic background, and MVA protocols with detection efficiencies of 80% or higher can be safely used. The disadvantage of this technique is that eddy currents induced in the electrodes by the quenching magnets cause them to heat up, requiring a 15 minute wait before they reach thermal equilibrium with the cryostat and the experiment can be repeated.

Ramping down the magnets without triggering a quench can be achieved in 1.5 s, with negligible electrode heating. This lengthens the search time for annihilation events and increases the false positive signal accordingly. However, the rate of false positives is still less than 0.1 per ramp down, so with a sufficiently high trapping rate, the fast ramp down technique allows us to perform experiments with a higher duty cycle without introducing significant background.

To be certain that the annihilation events we detect are from antihydrogen and not just low energy antiprotons left over from mixing and trapped between the mirror coils, we pulse an electric potential across the mixing trap electrodes to kick out any charged particles. Furthermore, a sloped electrostatic potential is held during the shutdown of the trap to deflect any antiprotons to one side. The direction of the potential is alternated between trapping runs so that a comparison can be made. The lack of a correlation between the annihilation positions and the direction of the sloped potential not only rules out mirror-trapped antiprotons, but allowed an initial limit to be placed on the charge of antihydrogen [22].

3 Antihydrogen spectroscopy considerations

The 1S-2S transition in hydrogen is electric dipole forbidden, and as a consequence it cannot be driven by a single 121.5 nm photon. Instead, we must excite the transition with two photons at 243 nm. If the atom absorbs two counter-propagating photons, then the Doppler shift which arises due to the atom's motion with respect to the laser beam cancels to first order. This technique is known as two-photon Doppler-free spectroscopy, and is instrumental in overcoming thermal linewidth broadening without having to cool the atoms down to millikelvin temperatures.

The 1S-2S transition frequency has been measured in a cold sample of magnetically trapped hydrogen with a precision of 2×10^{-12} by the MIT group [48], and in a cold atomic beam with a precision of 4.2×10^{-15} by the Hänsch group [49]. Both experiments used counter-propagating beams of 243 nm light for Doppler-free spectroscopy, with the MIT group using a single mirror to retro-reflect a tightly focussed 4 mW beam and the Hänsch group using a Fabry-Pérot enhancement cavity to generate 300 mW of circulating power.

To achieve such high precision, the Hänsch group generates 243 nm light from a frequency quadrupled 972 nm laser, which is locked to an ultra-stable reference cavity and related to the SI second using a frequency comb and portable caesium fountain clock. The ALPHA laser setup described in chapter 5 is closely modelled upon this system. A velocity selection technique is used to overcome the second order Doppler shift, and the experiment is repeated with different optical intensities to allow correction of the AC Stark shift. Both hydrogen experiments used a sample of between 10^{10} and 10^{12} atoms per trial, and detect the 1S-2S transition by mixing together the 2S and 2P states using an electric field and detecting the Ly-α photon emitted from the resulting 2P-1S decay.

In ideal circumstances antihydrogen would be subject to the exact same experiments as hydrogen, without relying on theoretical models, and avoiding systematics. However, the large magnetic fields required to synthesise and trap antihydrogen, the limited number of antihydrogen atoms produced per trial, and the necessary geometry of the ALPHA apparatus make such a comparison impossible. Instead, we must design our experimental procedures relying on the single particle sensitivity of the silicon vertex detector and MCP, and utilise the high accuracy at which modern theories can predict the behaviour of hydrogen to predict the energy levels of antihydrogen in the ALPHA magnetic field configurations for comparison. Several assumptions have to be made, and the handling of these will be detailed in this chapter.

3.1 The hydrogen atom

In this section we will look at how the model of the hydrogen atom has evolved over the last two centuries to the level where we can use it to accurately predict the energy levels of antihydrogen in a magnetic field (assuming CPT theory holds), and how this evolution was inspired by experimental discoveries. The derivation of these models is beyond the scope of this thesis, so we will simply examine the results. Examples of the derivations can be found elsewhere [50] [51] [52] [53], which are the sources of the equations presented. SI units are used throughout.

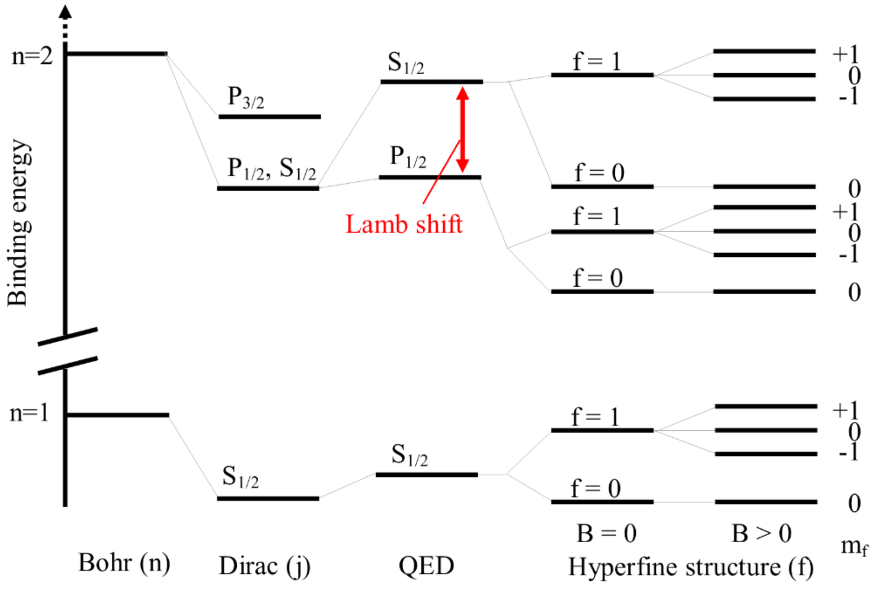

Figure 3.1: The energy levels of the hydrogen atom are illustrated as the accuracy of models which describe them improves. The horizontal axis shows the quantum numbers which describe the energy levels, and are introduced in the text. The vertical axis shows the energy of the levels, but the scale is illustrative only.

3.1.1 Historical observations

Dark lines in the solar spectrum were first recorded in 1802 by William Hyde Wollaston [54], and in 1814 were independently discovered by Fraunhofer, who systematically characterised the wavelength of over 570 such lines [55]. Around 45 years later, Kirchoff and Bunsen noticed that several of the lines observed by Fraunhofer coincided with bright lines emitted by heating chemical elements [56]. It was correctly deduced that the dark lines were created by the absorption of light by chemical elements in the solar atmosphere.

Although physicists could now observe emission and absorption lines, there was not yet a mathematical model for predicting where they should appear. Based on the visible spectra of hydrogen, Balmer developed an empirical equation in 1885 for predicting where these lines appear

$$\lambda = B\left(\frac{n^2}{n^2 - 2^2}\right), \tag{3.1}$$

where λ is the wavelength of the line, B is the continuum point with a value of 364.50682 nm, and n is an integer > 2.

This equation was generalised for all hydrogen series by Rydberg in 1888 as

$$\frac{1}{\lambda_{vac}} = R\left(\frac{1}{n_1^2} - \frac{1}{n_2^2}\right), \tag{3.2}$$

where R is the Rydberg constant and $n_1 < n_2$. It identifies the Balmer series as a special case where n_1 = 2, and successfully predicts the spectra of other series such as the Lyman series (n_1 = 1) in the UV and the Paschen (n_1 = 3) series in the IR.

3.1.2 The Bohr model

The physical explanation of the Rydberg formula was not understood until 1913, when the Bohr model of the atom was introduced. This model explained the spectra as the spacing between quantised energy levels, with the energies of the levels given by:

$$E_n = -\frac{Z^2 (k_e e^2)^2 m_e}{2\hbar^2 n^2}, \tag{3.3}$$

where $m_e c^2$ is the rest mass energy of the electron, $\frac{k_e e^2}{\hbar c} \equiv \alpha$ is the fine structure constant, and Z is the atomic number of the atom (although the equation is only accurate for hydrogen-like systems). The energy levels are denoted by the quantum number n, which is an integer greater than zero.

We have so far assumed that the electron orbits around a stationary nucleus, which in the case of hydrogen is a single proton. As the proton has a finite mass M, the electron and proton will both orbit the centre of mass of the system. In the rest frame of the proton, the electron will appear to have a reduced mass m, which is given by the relationship

$$m = \frac{m_e M}{m_e + M}. \tag{3.4}$$

3.1.3 Fine structure

As quantum mechanics developed, the Schrodinger equation introduced an additional quantization of the orbital angular momentum of the electron, with a corresponding quantum number l where $0 \leq l < n$, although states with the same n but different l still appear degenerate. At this point, it is convenient to introduce spectroscopic notation.

l	0	1	2	3
Spectroscopic notation	S	P	D	F

Table 3.1: Spectroscopic notation.

Energy levels can be identified by the principal quantum number n and a letter which corresponds to the orbital angular momentum l. The first four letters of spectroscopic notation stand for sharp, primary, diffuse and fundamental (for historical reasons), and continue alphabetically afterwards. For example, the ground state of the hydrogen atom is denoted as “1S”.

Importantly, photons also carry one unit of angular momentum. This means that transitions between energy levels involving a single photon must obey the selection rule $\Delta l = \pm 1$, which is why the single photon transition between the 1S and 2S levels ($\Delta l = 0$) of hydrogen is forbidden.

In addition to orbital angular momentum, the electron has an intrinsic angular momentum called "spin" corresponding to its magnetic moment. The quantum number s is associated with the spin, and for the electron $s = \frac{1}{2}$. As the two are necessarily coupled, the total angular momentum can be described by the quantum number j, where $j = |l - s|, |l - s| + 1 \ldots 0 \ldots l + s - 1, l + s$. The value of j is depicted in spectroscopic notation by a subscript below the orbital angular momentum letter. For example, the ground state of hydrogen can be denoted as "$1S_{1/2}$".

The Schrödinger equation neglects the relativistic effects of the electron, and whilst these can be included, it is easier to present the results of the Dirac equation, which is an attempt to unify the theories of quantum mechanics and special relativity:

$$E_{n,j} = mc^2 \left[1 + \frac{Z^2 \alpha^2}{\left(n - \left(j + \frac{1}{2} \right) + \sqrt{\left(j + \frac{1}{2} \right)^2 - Z^2 \alpha^2} \right)^2} \right]^{-\frac{1}{2}} . \tag{3.5}$$

This result correctly predicts the splitting of energy levels i.e. the $2P_{1/2}$ and $2P_{3/2}$ states, but note that the $2S_{1/2}$ and $2P_{1/2}$ states still appear degenerate.

3.1.4 The Lamb shift

The lamb shift is a splitting of the $2S_{1/2}$ and $2P_{1/2}$ states, first measured in the microwave spectrum of atomic hydrogen by the Lamb-Retherford experiment in 1947 [57]. The discovery of the Lamb shift led to the development of renormalisation theory and quantum electrodynamics (QED). The 1057 MHz frequency difference between the two states is primarily due to the vacuum polarisation effect (-27 MHz), the electron mass renormalisation effect (+1017 MHz), and the anomalous magnetic moment of the electron (+68 MHz), which are a result of the Feynman diagrams shown in Figure 3.2.

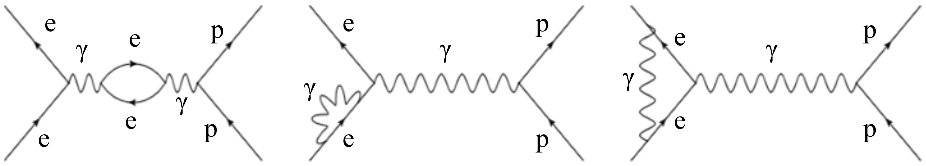

Vacuum polarisation Electron mass renormalisation Anomalous magnetic moment

Figure 3.2: Feynman diagrams showing the most significant contributions to the Lamb shift [50].

The energy shifts at the one-loop level for hydrogen are given for $l = 0$ by

$$\Delta E_{Lamb} = \alpha^5 \, mc^2 \frac{1}{4n^3}\{k(n,0)\}, \tag{3.6}$$

and for $l \neq 0$ by

$$\Delta E_{Lamb} = \alpha^5 \, mc^2 \frac{1}{4n^3}\left\{k(n,l) \pm \frac{1}{\pi\left(j+\frac{1}{2}\right)\left(l+\frac{1}{2}\right)}\right\}, \tag{3.7}$$

where $j = l \pm \frac{1}{2}$. $k(n,0)$ is a numerical factor which varies slightly with *n* from 12.7 to 13.2, and $k(n,l)$ is a much smaller numerical factor (<0.05) which again varies slightly with *n* and *l*. The Lamb shift mostly affects the S states, as these are the only states which the electron can be found at the nucleus.

3.1.5 Hyperfine structure

The theories we have considered so far have only considered quantisations of the electron, but the proton also has a spin of $s = \frac{1}{2}$. This leads to an additional quantum number *f* which has the possible values of $f = j + \frac{1}{2}, j - \frac{1}{2}$. The result of this is the splitting of each energy level into two, depending on the orientation of the electron and proton magnetic dipoles. The hyperfine energy shift for $l = 0$ states is given by

$$\Delta E_{HFS} = \frac{m}{M}\alpha^4 \, mc^2 \frac{4\mu_p}{3n^3}\left[f(f+1) - \tfrac{3}{2}\right], \tag{3.8}$$

where M is the proton mass and μ_p is the proton magnetic moment. The ground state hyperfine splitting of hydrogen, i.e. $\Delta E_{HFS}(f = 1) - \Delta E_{HFS}(f = 0)$, has been measured with a relative uncertainty of 6×10^{-13} [58]. For $l \neq 0$, the hyperfine energy shift is given by

$$\Delta E_{HFS} = \frac{m}{M} \alpha^4\, mc^2 \frac{\mu_p}{2n^3} \frac{\pm 1}{\left(f + \frac{1}{2}\right)\left(l + \frac{1}{2}\right)}, \tag{3.9}$$

where $f = j \pm \frac{1}{2}$.

3.1.6 The Zeeman Effect

So far we have only discussed atoms in a field-free environment. Each hyperfine state has a $2f + 1$ degeneracy associated with the quantum number m_f, which is the projection of the total angular momentum onto the z-axis and can take the values $m_f = -f, -f + 1 \ldots 0 \ldots f - 1, f$. The Zeeman effect is the breaking of this degeneracy due to the atoms interaction with a static magnetic field. For a moderate magnetic field B, the Zeeman splitting can be calculated with respect to the hyperfine centroid using the Breit-Rabi equation:

$$\Delta E_{n,f=j\pm\frac{1}{2},m_f} = -\frac{\Delta E_{HFS}}{4} - \mu_P m_f B \pm \frac{\Delta E_{HFS}}{2} \sqrt{1 + 2m_f x + x^2}, \tag{3.10}$$

$$x \equiv \frac{B(\mu_e(n) + \mu_P)}{\Delta E_{HFS}}.$$

In the case where $m_f = -1$, the square root contains an exact square and the positive solution is taken. Note that due to interactions with the nucleus, the magnetic moment of the electron $\mu_e(n)$ depends upon principle quantum number n, and for the $l = 0$ states is given by the relationship

$$\mu_e(n) = \mu_e \left(1 - \frac{\alpha^2}{3n^2}\right). \tag{3.11}$$

In spectroscopic notation, the hyperfine structure is commonly notated as a subscript after the angular momentum indicator, so for the hydrogen ground state would be $1S_a$, $1S_b$, $1S_c$, and $1S_d$, in order of increasing energy (see Figure 3.3).

3.1.7 Diamagnetic shift

An electron in an S state will circulate in an applied magnetic field (recall cyclotron motion from section 2.1.1), producing its own magnetic field which opposes the applied field. This field effectively shields the proton and causes the transition frequencies to shift upwards. This is known as the diamagnetic shift, and is given for the 1S and 2S states by

$$\Delta E_{dia}(1S) = \frac{e^2 a_0^2}{4m} B^2,\ \Delta E_{dia}(2S) = \frac{7e^2 a_0^2}{2m} B^2, \tag{3.12}$$

where a_0 is the Bohr radius.

3.1.8 Antihydrogen 1S-2S frequencies

The hydrogen 1S-2S transition frequency and the hyperfine splitting of both the 1S and 2S states have been measured with a precision meeting or exceeding what QED is able to predict [49] [58] [59]. As such, we only need to solve the Breit-Rabi and diamagnetic equations to calculate the Zeeman shift of the transition frequencies in the ~1 T magnetic field of the ALPHA apparatus. Only the c ($f = 1, m_f = 0$) and d ($f = 1, m_f = 1$) hyperfine states are trappable in a magnetic minimum trap, and the energy differences are given with an accuracy at the few kHz level by

$$v_{1S_d \to 2S_d} = v_{1S \to 2S} + \frac{1}{h}\left((\Delta E_{n=2,f=1,m_f=1} - \Delta E_{n=1,f=1,m_f=1}) + \frac{13e^2 a_0^2}{4m} B^2 \right), \tag{3.13}$$

$$v_{1S_c \to 2S_c} = v_{1S \to 2S} + \frac{1}{h}\left((\Delta E_{n=2,f=1,m_f=0} - \Delta E_{n=1,f=1,m_f=0}) + \frac{13e^2 a_0^2}{4m} B^2 \right), \tag{3.14}$$

where $v_{1S \to 2S}$ is the hyperfine centroid frequency [49] and h is the Planck constant. Frequency units are used instead of energy units to avoid accumulating factors of h. Figure 3.3 is a Breit-Rabi diagram of the 1S and 2S states, with arrows indicating the relevant transitions. Note that these are the total frequencies, and hence need to be halved for two-photon excitation.

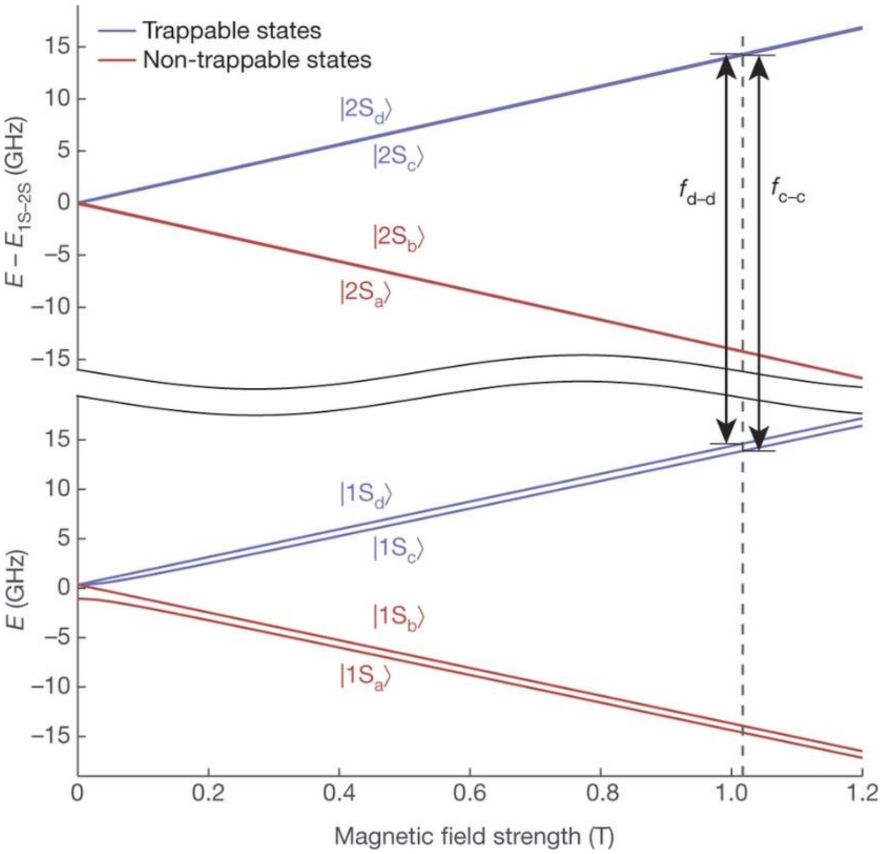

Figure 3.3: The calculated Breit-Rabi diagrams of the 1S (bottom) and 2S (top) states of antihydrogen. The blue lines show the low-field seeking trappable states and the red lines show the high-field seeking untrappable states. Image from [60].

At the measured magnetic minimum of 1.0168 T in the flattened trap configuration of 2016, the calculated transition frequencies are

$$v_{1S_d \to 2S_d} = 2\ 466\ 061\ 103\ 064\ \text{kHz}\,,$$

$$v_{1S_c \to 2S_c} = 2\ 466\ 061\ 707\ 104\ \text{kHz}\,.$$

There are of course additional systematic shifts imposed by the experimental conditions, which we will discuss in the next section.

3.2 Systematic shifts and broadenings

The transition frequencies will be subject to a number of systematic shifts and broadenings which must also be considered. As before, the values quoted correspond to the total 1S-2S transition frequency, and should be halved when compared to the 243 nm laser frequency which drives the transitions.

3.2.1 Residual Zeeman Effect

The Zeeman shifts of the 1S and 2S states almost cancel, but there is still a small dependence on the magnetic field which we call the residual Zeeman effect. Around the 1 T magnetic field of the trap, this scales as 9.6 Hz/mT for the d-d transition and 190 Hz/mT for the c-c transition. Whilst this shift is calculated in equation 3.10, magnetic field deviations will make a small contribution to the transition frequency uncertainty. The precision of the ECR technique discussed in section 2.2.9 therefore represents an uncertainty of ± 347 Hz and ± 6446 Hz for the d-d and c-c transitions respectively.

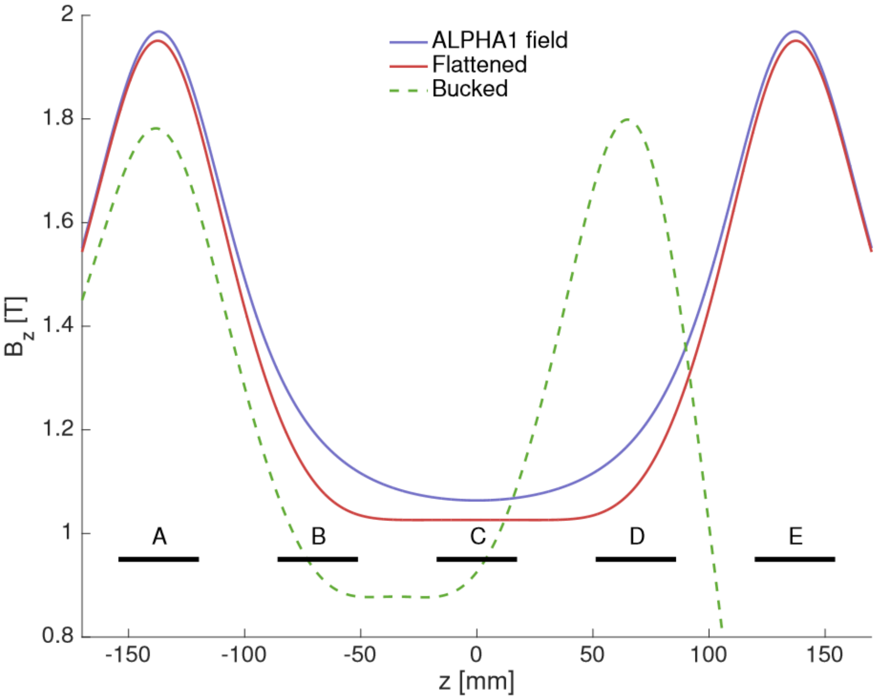

Figure 3.4: A plot of three possible magnetic field configurations. The black markers labelled A-E show the approximate sizes and locations of the mirror coils. Image from [52].

The shape of the magnetic field means that the line shape will be asymmetric, as the atom won't always cross through the laser beam at the magnetic minimum. The magnetic trap is described in chapter 2 and consists of an octupole for radial confinement and five mirror coils for axial confinement. The mirror coils can be operated with current running in either direction, allowing the shape of the trap to be carefully tuned. Figure 3.4 shows three possible configurations of the magnetic field.

The original ALPHA field is shown in blue, and comprises of just the octupole and the end mirror coils. The line shape asymmetry can be reduced by running reverse current through, or ‘bucking’, mirrors B, C, and D to flatten the field and increase the volume of the magnetic minimum region as shown in red. By running sufficient reverse current through mirror E, the field generated will cancel out the field of the external solenoid to create a zero field region (not shown) which is still within the coverage region of the silicon vertex detector (we will discuss why this could be useful soon). As a result the volume of the trap is reduced, as shown by the green dashed line.

3.2.2 Stark effect

The Stark effect is the shifting and splitting of energy levels with the application of an external electric field, due to the pulling of the nucleus and electrons in opposite directions. There exists both a DC and an AC Stark effect, and the two can be treated separately.

The DC Stark effect is responsible for broadening the transition due to the range of electric fields the atoms will experience from their ~90 m/s movement within the magnetic trap, as well as any potentials applied to the Penning trap electrodes. For the 1S-2S transition, the magnitude of the effect has been calculated [52] to be around 300 Hz, which is below the current accuracy requirements.

An AC stark shift occurs due to the oscillating electric field of the laser. For the target intensities within the ALPHA enhancement cavity, the shift in the middle of the beam was calculated [52] to be approximately 10 kHz. The shift is typically compensated for by measuring the line shape at several different circulating powers and extrapolating to zero power.

3.2.3 Transit time broadening

Heisenberg’s uncertainty principle tells us that there is a fundamental limit to the accuracy at which complimentary observables can be measured. In our case, the complimentary observables are the time at which the transition to the 2S state occurs, and the energy of the 2S state (i.e. the transition frequency).

As the waist of the enhancement cavity is relatively small ($\omega_0 = 196$ µm), and the atom travels through it relatively quickly (v ~90 m/s), the transit time is quite short. Therefore, there is a fundamental limit placed on the accuracy at which we can determine the 1S-2S transition frequency. The full-width half-maximum (FWHM) of this broadening [52] at 121 nm is given by the Fourier transform

$$\Delta v_{transit} = \sqrt{\ln(2)}\frac{\mathrm{v}}{\pi\omega_0} \approx 120\ \mathrm{kHz}\,. \tag{3.15}$$

This is the most significant source of broadening for the current 1S-2S experiment, and must be addressed if we wish to improve the precision of the measurement. Transit time broadening can be reduced by either enlarging the beam waist, or by cooling the atoms such that their transverse velocity is lowered.

3.2.4 2S lifetime reduction

The natural linewidth of the 1S-2S transition is inversely proportional to the lifetime of the 2S state. As such, any effect that acts to reduce the lifetime of the 2S state will accordingly broaden the transition linewidth. For 2 W of circulating power within the enhancement cavity, the main source of lifetime reduction was calculated [52] to be ionisation from the 2S state by a third 243 nm photon, which contributes approximately 8 kHz to the transition linewidth.

Table 3.2 gives a summary of the shifts and broadenings of 1 kHz or more towards the total 1S-2S transition frequency, using the parameters we have discussed above.

Effect	Contribution
Residual Zeeman	± 0.35 kHz (d-d) error ± 6.45 kHz (c-c) error
AC Stark	0-10 kHz shift
Transit time	120 kHz FWHM broadening
2S lifetime reduction	8 kHz FWHM broadening

Table 3.2: A summary of the shifts and broadenings which contribute >1 kHz towards the total 1S-2S transition frequency

3.3 Simulated transition rates

A simulation[1] by C. Rasmussen and F. Robicheaux was used to predict the transition rate and the loss mechanism for the atoms within the magnetic minimum trap. The simulation models the movement of the atoms within the trap as they interact with the laser. Once excited to the 2S state, the atoms can either decay back to the 1S state via two-photon emission, become ionised via a third 243 nm photon, or mix with the 2P states via the electric fields generated by the atom's movement through the magnetic field. The 2P state can decay to either a trappable 1S hyperfine state where 243 nm excitation can occur once again, or to an untrappable hyperfine state and annihilate on the trap walls. The simulation is described in detail in [52].

Figure 3.5 shows a plot of the relative fraction of antihydrogen atoms against the detuning of the 243 nm laser frequency using the simulation described above for the summed c-c and d-d transitions in the flattened magnetic trap configuration. The beam circulating within the enhancement cavity is assumed to have a waist of 200 μm and a power of 1 W. The laser linewidth is assumed to be 10 kHz. As discussed in section 3.2.1, the transition profile is asymmetric due to the shape of the magnetic field. Note from the inset figure that the time required to reach an excitation fraction of 0.5 is of the order of 100's of seconds.

---

[1] At the time of writing, Figure 3.5 differs from the figure shown in source [60] due to a factor of two error in the simulation of the linewidth. The corrected simulation is presented here, and a corrigendum to the original paper is being prepared.

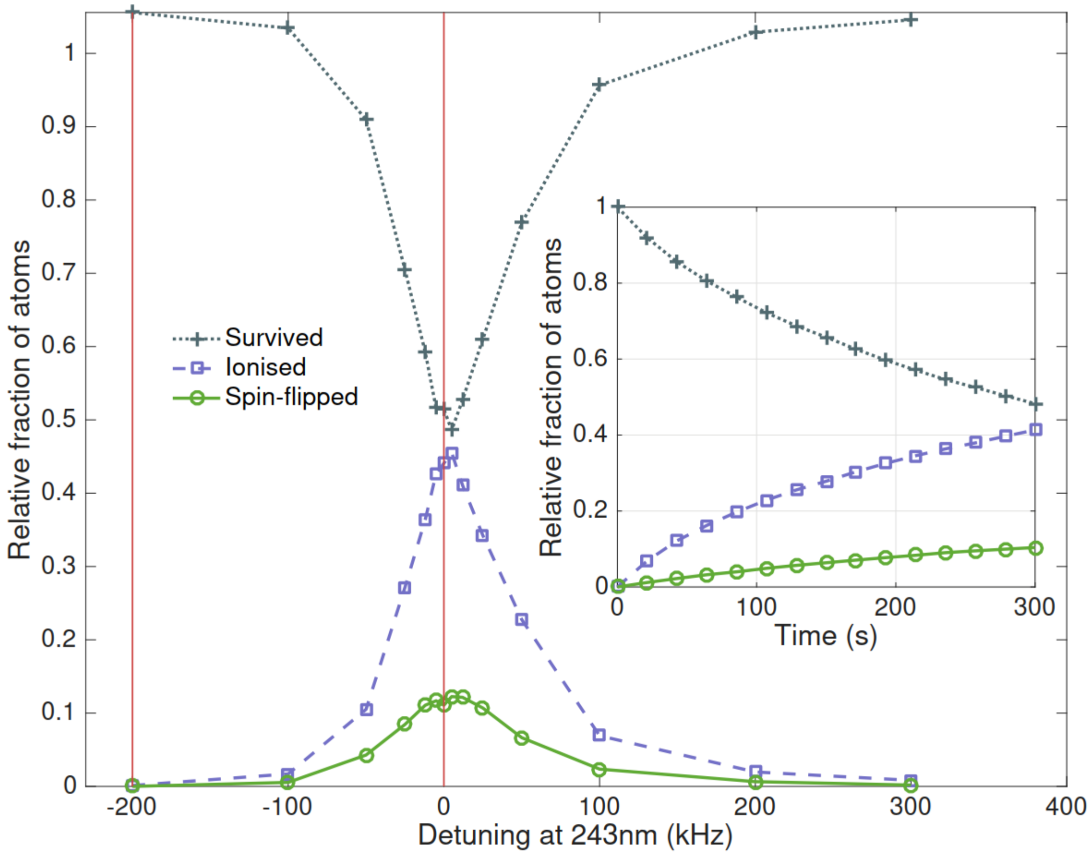

Figure 3.5: A simulation of the interaction between the antihydrogen atoms within the flattened trap yields the excitation rate and the linewidth of the summed c-c and d-d transitions. The inset shows the time dependence of the excitation period. Image from [60].

3.4 Detection schemes

3.4.1 Ly-α detection

The hydrogen 1S-2S experiments discussed earlier used a sample size of more than 10^{10} atoms, whereas ALPHA is currently limited to just a few trapped antihydrogen atoms at a time. Although the 121 nm Ly-α photons emitted by the decay from the 2P state can be detected with high efficiency using PMT's, the few photons emitted by the antihydrogen atoms are unlikely to register above the dark noise of the detectors over excitation times of 100's of seconds. Furthermore, the nested Penning-Malmberg and Ioffe-Pritchard traps within the ALPHA apparatus and the essential cryogenic hardware severely restricts the solid angle ($\sim 10^{-5}$) available for placing detectors, ruling out Ly-α detection as a viable method.

3.4.2 Annihilation - disappearance mode

Both the spin-flip and ionisation mechanisms reduce the number of atoms in the trap, so one can compare the apparent trapping rate between trial runs with different laser frequencies by simply counting the atoms left when the trap is shut down. As the trap can be shut down quickly, the cosmic background rate is almost negligible. This method requires the trapping rate to be roughly constant between consecutive runs, and that the excitation rate is sufficiently high or that there is sufficient data to be able to distinguish the laser runs from a control test. As this is the standard method of antihydrogen detection for ALPHA, no new techniques need to be developed.

3.4.3 Annihilation - appearance mode

After laser excitation to the 2S state, the dominant source of loss from the trap is ionisation by a third 243 nm photon. If the cold antiproton left behind could be detected with high sensitivity and low noise it would complement the disappearance measurement, and could significantly improve the efficiency of the experiment if the excitation rate is low.

The silicon vertex detector records events not only during the trap shut down, but throughout the long laser exposure periods too. As described in section 2.2.7, the MVA protocol can be tuned to maximise the signal to noise ratio for a given background rate. The background rate can be significantly reduced by only looking at the data during specific time periods (as was done for the microwave ground state hyperfine splitting experiment [25]), and can be further reduced by setting a region of interest within the trap. A weak electrostatic potential can be formed within the mixing trap to hold the antiprotons resulting from laser ionisation, and they can be ejected axially at well-defined times. If mirror E is bucked as we discussed in section 3.2.1, the antiprotons should follow the magnetic field lines to the wall and annihilate under mirror E. As these annihilations will have both a predictable time and location, the detector background can be almost zero.

The MCP is also capable of imaging single antiprotons [36], although the efficiency is unknown and difficult to estimate due to the large spread in energy deposited. On rare occasion, the secondary particles from the annihilation on the multi-channel plate can pass through neighbouring channels, triggering electrons to be emitted here as well, and leaving identifiable tracks (example: Figure 3.6). Similar to the process described before, the antiprotons resulting from laser ionisation could be captured in an electrostatic potential and ejected towards the MCP at regular intervals.

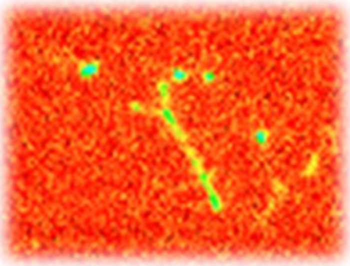

Figure 3.6: A close-up image of an antiproton annihilation on an MCP which has left identifiable tracks. The surrounding bright spots are also due to antiproton annihilations.

There is a caveat to these two techniques, which is that the antiproton plasmas trapped in an electrostatic potential which spans the entire mixing trap have been observed to become quickly unstable, with all particles lost after a few seconds. However, if the trapping and excitation rates are high enough, the annihilation of these lost antiprotons could be detectable over the background noise regardless.

4 The 1S-2S Enhancement Cavity

Commercial laser systems are only able to produce around 100 mW [61] of continuous wave power at 243 nm, so an enhancement cavity is required to build up a higher intensity within the ALPHA apparatus. A Fabry-Pérot cavity consists of two (or more) mirrors, within which constructive interference amplifies the optical intensity when the cavity length is tuned to resonance. Photons propagate in both directions, forming a standing wave within the cavity. Cavities within which photons only propagate in one direction also exist, and are known as ring or travelling wave cavities. The Fabry-Pérot configuration is more beneficial for spectroscopy, as the atoms within the cavity which absorb two counter-propagating photons will not experience a Doppler shift (to 1st order).

Two different Fabry-Pérot cavity geometries have been trialled within the ALPHA apparatus - an internal cavity, using mirrors mounted within the cryogenic region, and an external cavity, with mirrors mounted just inside the vacuum viewports at the ends of the apparatus. Whilst the external cavity is simpler to construct, at 2.7 m it is triple the length of the internal cavity and more susceptible to environmental noise. The internal cavity is a rigid, pre-aligned cavity whose only degree of freedom is length. However, as the mirrors are installed in the cryogenic, UHV region of the apparatus, they must fulfil strict criteria. The mirrors must not break or deform when the experiment is baked at 80 °C and cooled down to 7 K, and must maintain their alignment and not need servicing during the ~5 month antiproton beam period. The mirror mounts must not be made from or include any magnetic or superconducting material, as this can influence the shape of the magnetic field and potentially be damaged when the trap magnets are ramped. The mounts must also be made using only very low outgassing materials, so as not to degrade the lifetime of the trapped antiprotons, positrons, and antihydrogen by contaminating the vacuum. Finally, the mounts must fit within the few cm of space between the particle beam line and the inner diameter of the vacuum chamber. The tight space constraints severely limit the use of flexure mounts and of any kind of active alignment, and attempts to simply epoxy the mirrors to a solid mount resulted in them breaking due to the mismatched coefficients of thermal contraction.

In this chapter we will examine how light behaves in a simple Fabry-Pérot cavity, before looking at the development of an athermal mirror cell which solves the aforementioned problems and enables the use of an internal cavity. We will also look at the design of the external cavity, and compare the performance of the two designs.

4.1 Enhancement cavity theory

Let us consider the interaction between a laser beam of wavelength λ and a Fabry-Pérot cavity consisting of two mirrors separated by distance *d*. The mirrors have a field amplitude reflection coefficient *r* and a transmission coefficient *t*, and the incident light has field amplitude E_0.

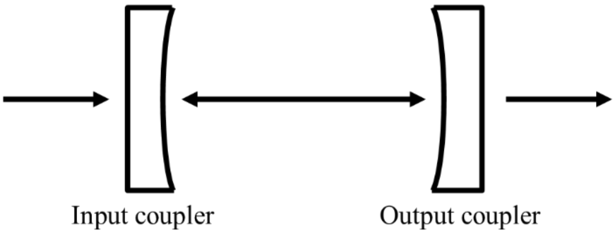

Figure 4.1: A two-mirror Fabry-Pérot cavity

We can write the field amplitude transmitted through the first mirror (or 'input coupler') simply as

$$E = t_1 E_0 \,. \qquad (4.1)$$

After one complete round trip within the cavity the light will have an amplitude

$$E = t_1 E_0 r_1 r_2 e^{i4\pi d/\lambda} \,, \qquad (4.2)$$

where the exponent contains the accumulated phase shift. After N complete round trips within the cavity without interference, the resultant field amplitude of the light will be

$$E = t_1 E_0 (r_2 r_2)^N e^{i4\pi dN/\lambda} \,. \qquad (4.3)$$

If the incident light is continuous, then the circulating field inside the cavity can be written as a sum of the waves which have made 0, 1, 2, …N round trips,

$$E_{circ} = t_1 E_0 \sum_{N=0}^{\infty} (r_1 r_2)^N e^{i4\pi dN/\lambda} = \frac{t_1}{(1 - r_1 r_2 e^{i4\pi d/\lambda})} E_0 \, . \tag{4.4}$$

The reflected field includes contributions from both the incident field reflected directly from the input coupler and the field transmitted through the input coupler from the cavity:

$$E_r = \left[-r_1^* + \frac{r_2 t_1^2 e^{i4\pi d/\lambda}}{(1 - r_1 r_2 e^{i4\pi d/\lambda})} \right] E_0 \, . \tag{4.5}$$

To calculate the enhancement factor of the cavity, it is more practical to convert into units of power. The mirrors have a power reflectivity $R \equiv |r|^2$ and transmission $T \equiv |t|^2$. Note that the mirrors are not perfect and will also have a loss L associated with them, which can be due to absorption within the mirror coating or surface imperfections scattering the incident light. Conservation of energy dictates that the sum of these parameters must equal 1, i.e.

$$R + T + L = 1 \, . \tag{4.6}$$

We can write the power circulating within the cavity as

$$P_{circ} = |E_{circ}|^2 = \frac{T_1}{\left|1 - \sqrt{R_1 R_2} e^{i4\pi d/\lambda}\right|^2} P_0 \, . \tag{4.7}$$

The reflected power is given by

$$P_r = |E_r|^2 = \frac{\left|-1 + \left(1 + \frac{T_1}{R_1}\right) \sqrt{R_1 R_2} e^{i4\pi d/\lambda}\right|^2}{\left|1 - \sqrt{R_1 R_2} e^{i4\pi d/\lambda}\right|^2} R_1 P_0 \, , \tag{4.8}$$

and the power transmitted through the cavity is simply

$$P_t = T_2 P_{circ} \, . \tag{4.9}$$

4.1.1 Resonance

When the cavity length is a half-integer ($n/2$) number of wavelengths of the laser, the exponent $e^{i4\pi d/\lambda} = e^{i2\pi n} = 1$. This is the resonant condition of the cavity, where the circulating power is at a maximum and the reflected power is at a minimum. We can define the enhancement factor b as the ratio between the circulating power on resonance and the input power, i.e.

$$b = \frac{P_{circ}}{P_0} = \frac{T_1}{\left(1 - \sqrt{R_1 R_2}\right)^2} . \tag{4.10}$$

For certain mirror configurations, the reflected power becomes zero when the cavity is on resonance. This condition is known as 'impedance matched', and is given to first order by

$$T_1 = T_2 + L_1 + L_2 . \tag{4.11}$$

The spacing between resonances is known as the free spectral range (FSR). A free spectral range can be spanned either by scanning the cavity length by $\lambda/2$ or by changing the laser frequency by $c/2d$, where c is the speed of light. The linewidth of the cavity is defined as the FWHM of a resonance, and for high reflectivity mirrors (R > 0.9) has an approximately Lorentzian profile. Like the free spectral range, it can be expressed in terms of both the cavity length and the laser frequency. The cavity length interpretation is important as it gives us an idea of how accurately we need to control the length of the cavity to keep it on resonance, and the laser frequency interpretation is important as if the laser linewidth is greater than the cavity linewidth, it will be an additional source of loss.

The ratio between the free spectral range and the linewidth gives us a parameter called the finesse F. For high reflectivity mirrors (R > 0.9), the finesse is well approximated by

$$F \equiv \frac{\text{FSR}}{\text{Linewidth}} \approx \frac{\pi (R_1 R_2)^{\frac{1}{4}}}{1 - \sqrt{R_1 R_2}} . \tag{4.12}$$

Note that the finesse depends only upon the mirror reflectivity and not the cavity length or laser frequency. The enhancement factor can be expressed in terms of the finesse as

$$b \approx T_1 \left(\frac{F}{\pi}\right)^2 , \tag{4.13}$$

which is convenient as it can be difficult to accurately measure mirror reflectivity when it approaches 1, whereas the finesse is relatively straightforward to measure.

4.1.2 Transverse mode matching

So far we have only discussed the longitudinal properties of the cavity, but we must of course consider the transverse properties of the cavity as well. Gaussian beams can be characterised by the beam waist at the focal point w_0, and the laser wavelength λ. The beam radius along the direction of propagation (z) is given by [62]

$$w(z) = w_0 \sqrt{1 + \left(\frac{z}{z_0}\right)^2}\ , \tag{4.14}$$

and the radius of curvature $\mathcal{R}$ of the wavefront is given by [62]

$$\mathcal{R}(z) = z \left[1 + \left(\frac{z_0}{z}\right)^2\right]. \tag{4.15}$$

The wavefront curvature decreases from infinity at $z = 0$ to a minimum at $z = z_0$ before increasing linearly for large z. z_0 is known as the 'Rayleigh range', and is related to the beam waist by [62]

$$z_0 = \frac{\pi w_0^2}{\lambda}\,. \tag{4.16}$$

Let's consider a Gaussian beam with $w_0 = 0.2$ mm located at $z = 0$, $\lambda = 243$ nm, and $z_o = 0.517$ m as illustrated in Figure 4.2. A cavity with this beam profile could be formed by placing mirrors at any z where the radius of curvature of the mirror matches the radius of curvature of the wavefront. Note that the waist does not necessarily have to be within the cavity, as a cavity could be formed using a convex and concave mirror on the same side of the waist. However, if we place a pair of concave mirrors with $\mathcal{R}_1$ and $\mathcal{R}_2$ either side of the waist at z_1 and z_2, we can equate $\mathcal{R}_1 = \mathcal{R}(z_1)$ and $-\mathcal{R}_2 = \mathcal{R}(z_2)$, where the negative radius of curvature of mirror 2 is because the mirror is facing the opposite direction. Writing out equation 4.15 explicitly,

$$\mathcal{R}_1 = z_1 + \frac{z_0^2}{z_1}\ , -\mathcal{R}_2 = z_2 + \frac{z_0^2}{z_2}\,, \tag{4.17}$$

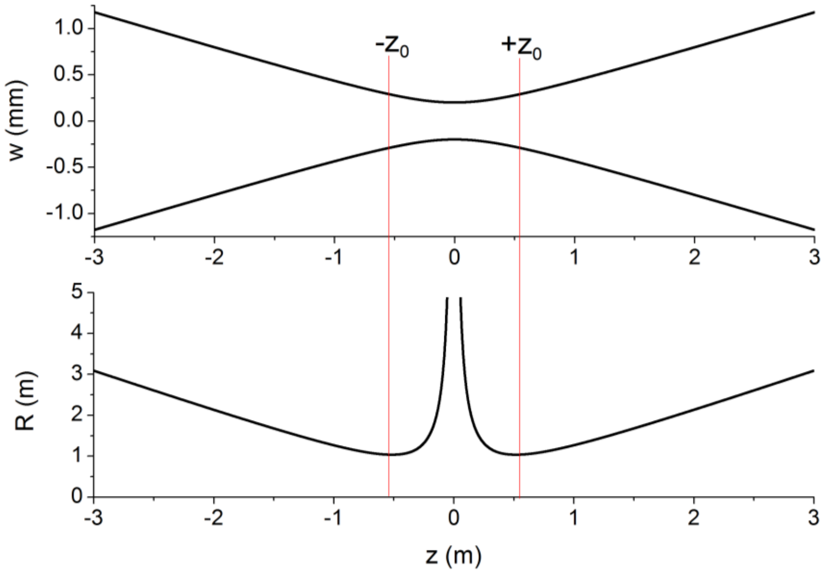

Figure 4.2: A plot of the beam waist (top) and the wavefront radius of curvature (bottom) for a Gaussian beam with $w_0 = 0.2\ mm$*,* $\lambda = 243\ nm$*, and* $z_0 = 0.517\ m$ *over a 6 m propagation length.*

and using our earlier definition of the cavity length,

$$d = z_2 - z_1 \,, \tag{4.18}$$

this gives us a set of equations which we can solve for z_1, z_2, and z_0:

$$z_1 = \frac{-d(\mathcal{R}_2 + d)}{\mathcal{R}_2 + \mathcal{R}_1 + 2d} \,, \quad z_2 = z_1 + d \,, \tag{4.19}$$

$$z_0^2 = \frac{-d(\mathcal{R}_1 + d)(R_2 + d)(\mathcal{R}_2 + \mathcal{R}_1 + d)}{(\mathcal{R}_2 + \mathcal{R}_1 + 2d)^2} \,. \tag{4.20}$$

Since we have a method for calculating z_0 and the location of the waist, everything about the cavity can be determined. The size of the beam waist can be calculated by re-arranging equation 4.16 to give $w_o = \sqrt{\frac{\lambda z_o}{\pi}}$, and the beam size at the mirrors can be calculated using equation 4.14. For the beam to be confined by the cavity, z_0 must be real, and hence z_0^2 in equation 4.20 must be positive. It can be shown that the condition $z_0^2 > 0$ is equivalent to

$$0 \leq \left(1 - \frac{d}{\mathcal{R}_1}\right)\left(1 - \frac{d}{\mathcal{R}_2}\right) \leq 1. \tag{4.21}$$

This condition is known as the confinement condition, and is commonly expressed in terms of two g factors;

$$g_i = 1 - \frac{d}{\mathcal{R}_i}\,, \quad i = 1, 2\,. \tag{4.22}$$

Figure 4.3 shows the stable region (blue) where the confinement condition is satisfied for various cavity geometries. Points along the dashed red line represent symmetrical resonators, i.e. where $g_1 = g_2$.

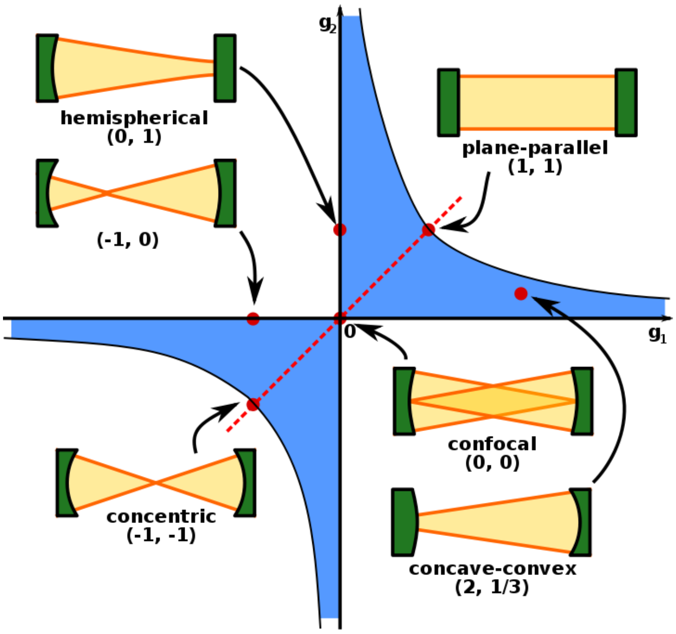

Figure 4.3: The stability of different cavity configurations as defined by their g factors (g_1,g_2). Only the configurations under the blue shaded region are stable. Image by [63].

For a perfectly aligned and mode matched cavity, the only resonant spatial mode will be the fundamental Gaussian mode, sometimes labelled as the TEM_{00} mode. The peak intensity I_0 of such a beam is related to the optical power P by [62]

$$I_0 = \frac{2P}{\pi w_0^2}\,, \tag{4.23}$$

and the relative intensity at any point within the beam is given by [62]

$$\frac{I(x,y,z)}{I_0} = \left(\frac{w_0}{w(z)}\right)^2 e^{\frac{-2(x^2+y^2)}{w^2(z)}}\,. \tag{4.24}$$

However, a cavity can often support many different spatial modes, and these will have a different intensity profile. Hermite-Gaussian modes typically result from a misaligned or distorted input beam, and Laguerre-Gaussian modes typically arise from a mismatch between the laser and cavity beam waists (see Figure 4.4 for examples), but these depend greatly on the cavity geometry. In general it is desirable to eliminate these higher order modes, so we will not examine their spatial profile in more detail.

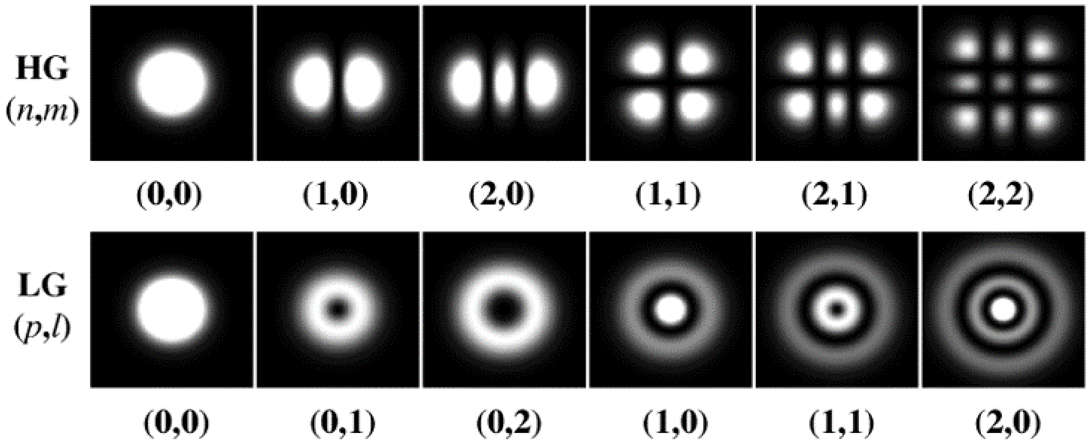

Figure 4.4: Hermite-Gaussian (top) and Laguerre-Gaussian (bottom) modes. Image from [64]

4.1.3 Cavity locking techniques

For many applications, it is desirable to lock the cavity on resonance. This can either be done by locking the cavity length to a laser or by locking the laser frequency to the cavity. The former is useful for building up the intensity of the laser beam for spectroscopy or non-linear processes such as frequency doubling, whilst the latter is useful for stabilising a laser by locking it to an ultra-stable cavity with an extremely narrow linewidth. Both applications require an error signal which has a zero crossing point to be generated. A servo loop can then control an actuator (such as a piezo behind a cavity mirror, or the temperature of the laser) to actively minimise the error signal.

The most basic form of lock is a side-of-peak lock. In this case, the error signal is simply the transmission signal of the cavity with a DC offset subtracted. This locking technique is not capable of locking to the top of a resonance however, as the error signal here would be unipolar and the servo would not know in which direction to actuate. The lock is extremely susceptible to amplitude noise, including DC sources such as changes in the ambient background light.

A large improvement can be realised by applying a small modulation to the cavity length at a frequency higher than any expected noise sources (typically > 10 kHz). The difference signal derived from electronically mixing the drive modulation and the modulation present in the cavity transmission is proportional to the phase difference between the two signals (more precisely, it is the derivative of the peak), and has a zero crossing point at the peak of the resonance. This error signals allows the cavity to be locked at the top of the resonance and is relatively insensitive to sources of noise. This technique is known as an ‘amplitude modulation’ (AM) lock, or ‘dither’ lock.

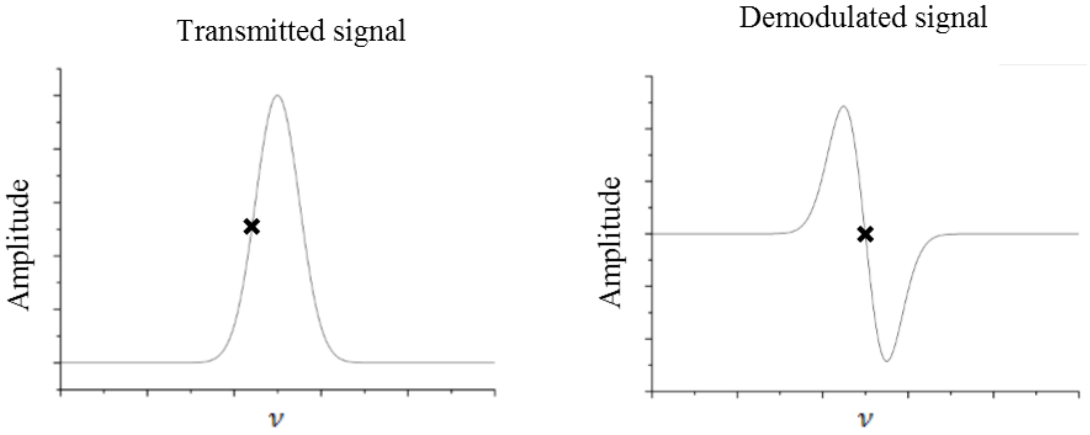

Figure 4.5: The ‘x’ shows the lock points for the side of peak lock (left) and the amplitude modulation error signal (right). The frequency scale is the same for both plots.

A further improvement can be gained by modulating the frequency of the laser instead. With the Pound-Drever-Hall (PDH) locking technique [65], sidebands are added to the laser frequency by either directly modulating the laser frequency or passing the beam through an external electro-optic modulator (EOM). The sidebands are typically many MHz away from the carrier frequency and can span a significant fraction of the cavity free spectral range. As the sidebands are outside of the cavity linewidth they will not be resonant at the same time as the carrier frequency and instead get reflected. By electronically mixing the modulation frequency with the beat frequency between the reflected sidebands and carrier, an error signal with a sharp zero crossing point similar to the amplitude modulation technique can be generated.

However, the error signal now extends all the way out to the sidebands, greatly increasing the capture range of the lock.

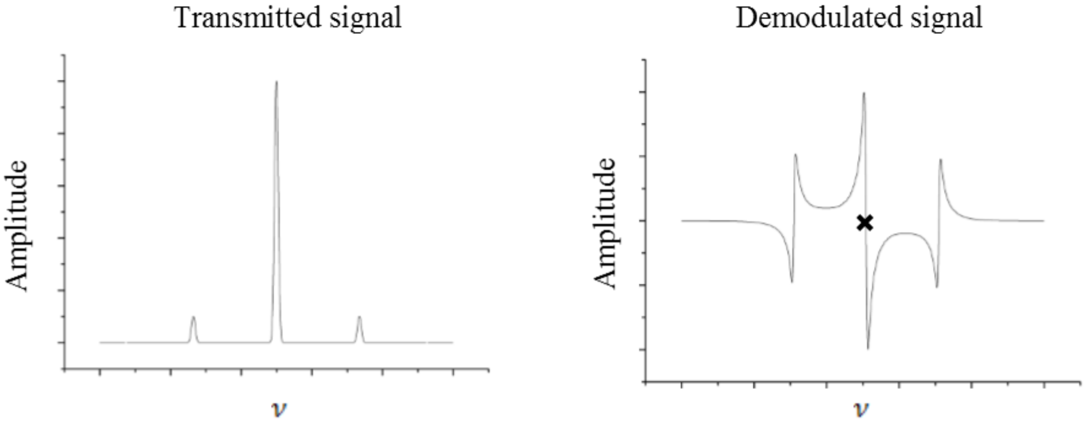

Figure 4.6: The frequency/phase modulation adds sidebands to the beam, which are visible in the transmitted signal (left). The capture range of the PDH error signal extends to the sidebands, yet maintains a sharp slope to lock to (right). The 'x' indicates the lock point.

4.1.4 Cavity power

We can write the average circulating power within the cavity as

$$P_{avg} = b\gamma Q_{lock} P_0 \,. \tag{4.25}$$

In this equation, we have introduced a spatial mode matching constant γ, which we define as the ratio of the fundamental mode to all other modes coupled into the cavity. Q_{lock} is a fraction representing the quality of the lock.

As the PDH scheme uses only the reflected light to lock the cavity, this allows a power meter to be placed after the output coupler to accurately measure the transmitted power. If the transmission of the output coupler is well known, the average circulating power can be calculated by rearranging equation 4.9 to get

$$P_{avg} = \frac{P_t}{T_2} \,. \tag{4.26}$$

4.2 Athermal mirror cell development

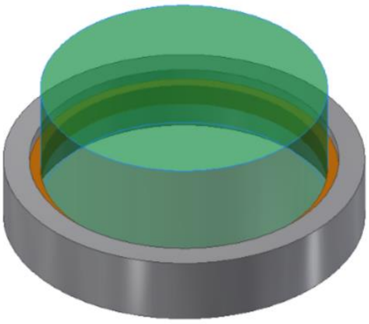

Figure 4.7: An athermal mirror cell consisting of an optic (green) bonded within a metal ring (grey) using an epoxy (orange). Autodesk Inventor model.

An athermal mirror cell consists of an optic bonded inside a metal ring using an epoxy, where the materials and dimensions have been chosen such that there is zero stress applied to the optic at all temperatures within a given range. For this to be true, the coefficient of thermal expansion (CTE) of the ring a_r must be greater than the CTE of the optic a_o, and the CTE of the epoxy bond a_b must be greater than the CTE of both the cell and the optic. Equivalently;

$$a_b > a_r > a_o \, . \tag{4.27}$$

This condition alone is not sufficient, so the cell must then be fine-tuned by varying the thickness of the epoxy bond. There exist several published methods for calculating the optimal thickness h of the epoxy bond for an optic of diameter d_o [66]. The simplest of these is the Bayar equation [67];

$$h_{Bayar} = \frac{d_o(a_c - a_0)}{2(a_b - a_r)} \, . \tag{4.28}$$

However, this equation neglects the Poisson's ratio of the epoxy bond σ_b, which is the ratio of the transverse contraction to longitudinal expansion of a material when it is stretched or compressed. A more complete description of the bond (including σ_b) is given by the DeLuzio equation;

$$h_{DeLuzio} = \frac{d_o}{2} \frac{1 - \sigma_b}{1 + \sigma_b} \frac{a_r - a_o}{(a_b - a_o) - \frac{(7 - 6\sigma_b)(a_r - a_o)}{4(1 + \sigma_b)}} \, . \tag{4.29}$$

DeLuzio also provides an equation [66] for calculating the radial stress applied to the optic $S_{o.r}$ for a given bond thickness;

$$S_{o.r} = \frac{E_b \Delta T}{4(1-2\sigma_b)(1+\sigma_b)} \left[\left[\frac{-1}{\ln\left(\frac{\frac{d_o}{2}+h}{\frac{d_o}{2}}\right)} + (10-8\sigma_b)\frac{\left(\frac{d_o}{2}+h\right)^2}{\left(\frac{d_o}{2}+h\right)^2 - \left(\frac{d_o}{2}\right)^2} \right] (a_r - a_o) + 4(1+\sigma_b)(a_o - a_b) \right], \qquad (4.30)$$

where E_b is the modulus of elasticity of the bond and ΔT is the change in temperature experienced.

4.2.1 Design and Prototyping

One of the key difficulties with athermal mirror cells is forming the bond. Some groups have had success by engineering the metal ring with epoxy injection holes [68] [69]. However, a finite element modelling study by Kihm et al. [69] shows that the epoxy in the injection holes can adversely influence the mirror surface. A series of tests were performed to prototype simpler methods using an M6 bolt head to represent the optic and an M8 washer to represent the metal ring. EPO-TEK's H77 epoxy was used for the initial trials as it is NASA certified as a low outgassing material [70]. Two different approaches were investigated:

First, the bolt head and washer were firmly clamped to an aluminium base coated in PTFE tape, and the gap between them was flooded with epoxy. Whilst this technique reliably bonded the bolt head to the washer, the epoxy had a tendency to seep beneath the components. The PTFE tape would also be weakly bonded to the epoxy and had to be scraped off, which is unsuitable for use in a UHV system.

Second, the bolt head and washer were gently clamped to a clean aluminium base, and a bead of epoxy was used to bridge the gap, held in place by surface tension. Initially, the air trapped behind the epoxy would bubble up causing the bond to fail. This was solved by adding small vents in the aluminium base under the gap. A single vent caused the epoxy bond to be slightly deeper on one side, whereas with 4 vents (a cross cut into the aluminium as shown in Figure 4.8), the epoxy bond formed uniformly.

The second approach was chosen as it would preserve the back surface of the mirror. However, this meant that the epoxy had to be viscous enough to span the gap between the mirror and the ring, so a more viscous epoxy with the same low-outgassing certification was sought after and identified. Table 4.1 compares the properties of EPO-TEK H77 with EPO-TEK T7109. In addition to the higher viscosity, T7109 also has a higher elasticity and a greater CTE.

EPO-TEK Epoxy	CTE (average m/m per K)	Storage modulus (Pa) (α elasticity^{-1})	Viscosity (cPs @ 20 rpm)	Poisson ratio
H77	3.30×10^{-8}	6.55×10^{9}	6,000-12,000	0.3 – 0.35
T7109	4.60×10^{-8}	1.78×10^{9}	14,000-20,000	0.3 – 0.35

Table 4.1: A comparison of the properties of EPO-TEK H77 and EPO-TEK T7109 epoxies. Data from the H77 [70] and T7109 [71] datasheets. It is important to note that the CTE data for the epoxies was only available down to 228K and must be extrapolated down to 7K.

The H77 epoxy was measured to be able to reliably span a radial gap of 0.5 mm or less, whereas the more viscous T7109 epoxy could reliably span a gap of 1 mm. Leaving the uncured epoxy to sit for several hours would increase the viscosity at room temperature, but when heated in an oven to cure, the epoxy would return to its less viscous state and the bond would fail.

Table 4.2 shows the calculated optimum gap sizes for cells made using H77 and T7109 epoxy with both titanium and steel rings, using data from [72]. Based on the epoxies' ability to span gaps, the combination of a titanium ring with T7109 epoxy appeared to be most favourable. Note that the optic is necessarily fused silica as it must have high transmission of 243 nm light. Tungsten was ultimately ruled out as a ring material as although it would allow for a cell with a smaller gap, it is difficult to machine.

Ring	Epoxy	h_{Bayar} (mm)	$h_{DeLuzio}$ (mm)
Titanium	H77	1.24	0.62
Titanium	T7109	0.84	0.42
Steel	H77	2.13	1.07
Steel	T7109	1.40	0.71

Table 4.2: A calculation of optimal radial bond thicknesses using the Bayar and DeLuzio equations for four potential mirror cells.

A trial cell was made, using a THORLABS WG40530 UV fused silica window ($Ø_{\text{outer}}$ = 12.7 mm) and a steel M12 washer ($Ø_{\text{inner}}$ = 13.0 mm) and cooled down to 20 K on a coldhead. Even though the 0.15 mm radial gap was almost an order of magnitude smaller than the value calculated by equation 4.12, the optic did not break, thus proving the viability of the technique. Three athermal cells were produced and tested in parallel to have a working design ready for the 2014 antiproton beam period:

1) 0.5 mm radial gap H77 titanium cell – slightly smaller than the predicted ideal gap but encouraged by the prototype results
2) 0.5 mm radial gap T7109 titanium cell – close to the predicted ideal gap
3) 1.0 mm radial gap T7109 titanium cell – the larger gap is inspired by the dimensions used in [69], where the elasticity of the epoxy is claimed to prevent deformations of the mirror surface

The optic chosen for these test cells was the THORLABS PF05-03 fused silica mirror blank, as only the top surface is polished, allowing interferometric measurements of the deformation to be made without suffering from secondary reflections.

4.2.2 Mirror cell assembly

To ensure that the optic was well centred within the ring, and that the top surface of the optic was parallel with the bottom surface of the ring, an alignment jig was made. The jig (shown in Figure 4.8) features a central cup which supports the optic, and a ring holder which maintains the centring of the ring. The mirror cup is raised 0.5

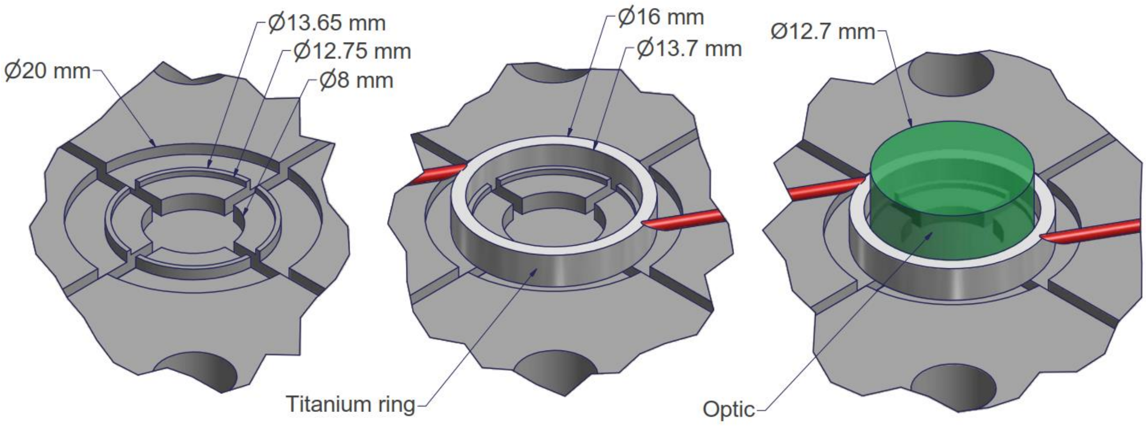

Figure 4.8: A close up view of the cell making jig, showing the locations where the ring and optic sit (Autodesk Inventor drawing).

mm above the bottom of the ring holder to prevent the optic coming into contact with the surface the cell is finally attached to. Crossed channels are cut into the jig to prevent pressure building up underneath the epoxy when heated, and the central 8 mm is bored out to prevent the back surface of the optic becoming scratched. Figure 4.9 shows the optic and the cell placed on the jig, which are then clamped down before the epoxy is applied.

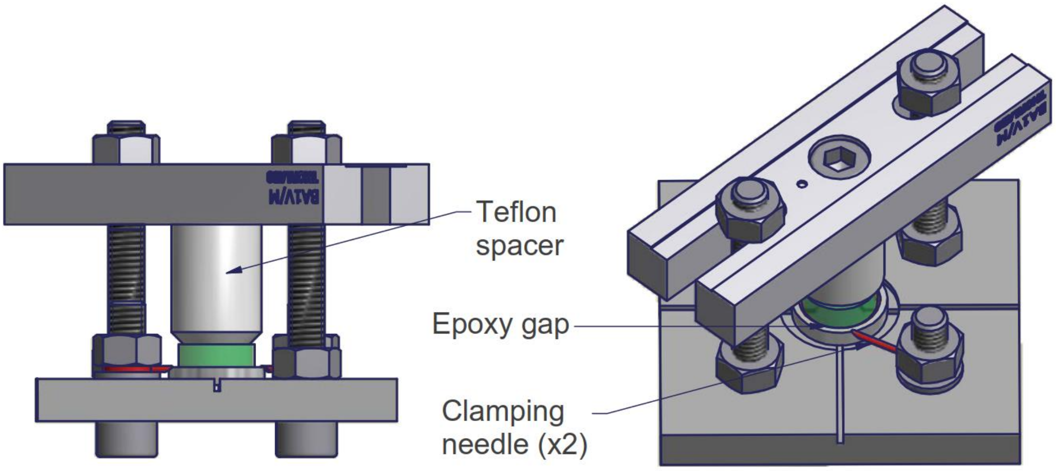

Figure 4.9: The optic and ring are placed onto the jig. The ring is clamped via two slash-cut needles and the optic is clamped via a Teflon spacer whilst the epoxy cures (Autodesk Inventor model).

Two slash-cut needles (shown in red) are used to firmly clamp the ring in place, whilst pressure is applied to the optic from above through a Teflon spacer. A third slash-cut needle is used to pick up a 1 mm bead of epoxy and apply it to the gap. The epoxy must not be forced into the gap, but should instead be applied carefully to the top of the gap, where it will naturally sink in slightly until it becomes suspended by surface tension. Beads of epoxy are placed all the way around the optic to form a continuous bond. The assembly is then placed into an oven to cure in a 2 step sequence. It is first heated at 40°C for 30 minutes to remove air bubbles from the epoxy, and then heated at 150°C for 1 hour to cure the epoxy. After cooling back to room temperature, the cell is removed from the jig and is ready for use.

4.2.3 Optical deformation measurements

To achieve a high finesse cavity, it is essential that the mirrors do not significantly deform. An interferometer was constructed to measure the deformation with a target precision of around 100 nm peak to peak (see Figure 4.12 for the optical layout). The mirror cells are epoxied to an adapter piece of the same material and dimensions as used within the ALPHA apparatus, and mounted to a coldhead. The coldhead consists of 20 K inner stage with a copper heat sink, temperature sensor, and heater element, as well as an outer stage which hosts a radiation shield. The mirror adapter can be mounted directly to the inner stage heat sink, as shown in Figure 4.10. The coldhead is mounted in a vacuum chamber which sits on vibration dampening feet next to the interferometer optical table. Two clamping arms connect the vacuum chamber to the optical table to minimise the measurement noise. The chamber is pumped out using a turbomolecular pump, but during measurements and cooldowns this is valved off and shut down, and the vacuum is maintained by an ion pump. The chamber has a window to allow optical access, and achieves a vacuum of 1×10^{-6} mbar at room temperature and 1×10^{-8} mbar when cold. The cooldown rate is shown in Figure 4.11.

.

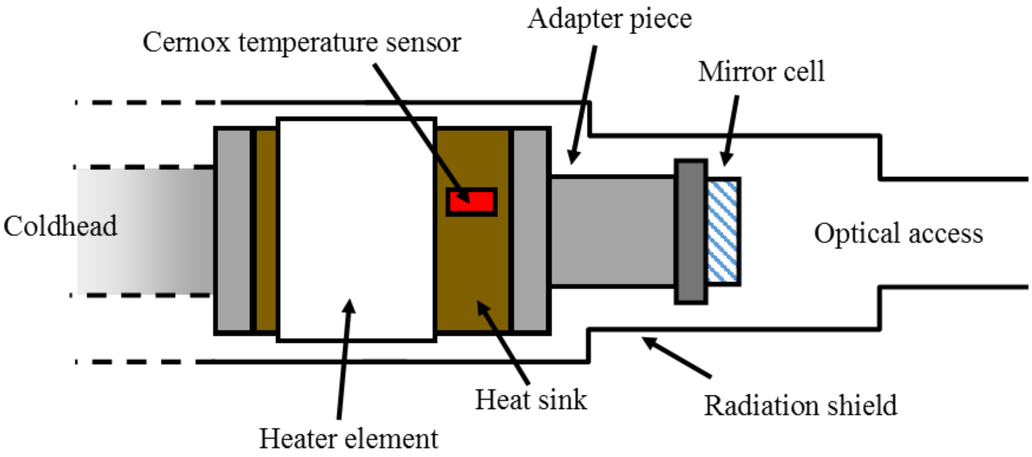
Adapter piece
Cernox temperature sensor
Mirror cell
Coldhead
Optical access
Heat sink
Radiation shield
Heater element

Figure 4.10: The mirror cell is epoxied to a stainless steel adapter piece using the same epoxy and curing process as the cell manufacture. The adapter piece threads into a copper heat sink which is cooled to 20 K by the inner stage of a coldhead. The heat sink is equipped with a Cernox temperature sensor and a heater element. Connected to the outer stage of the coldhead is a copper radiation shield, which has a Ø 12 mm hole for optical access.

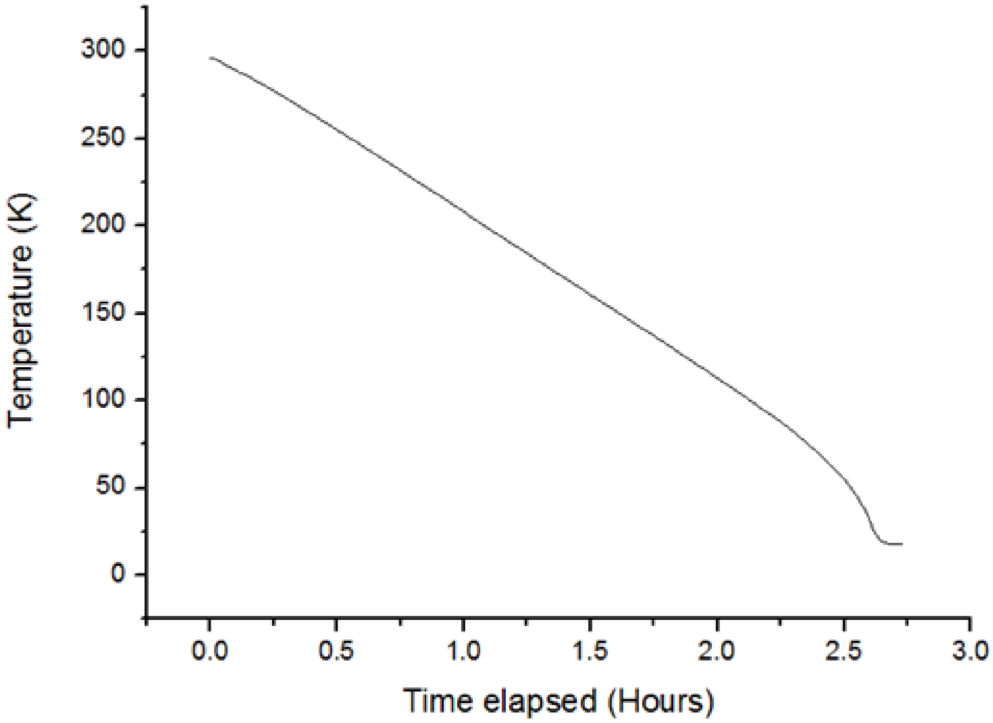

Figure 4.11: The coldhead cools from room temperature to 20 K in just under 3 hours, which is similar to the cooldown rate of the ALPHA apparatus.

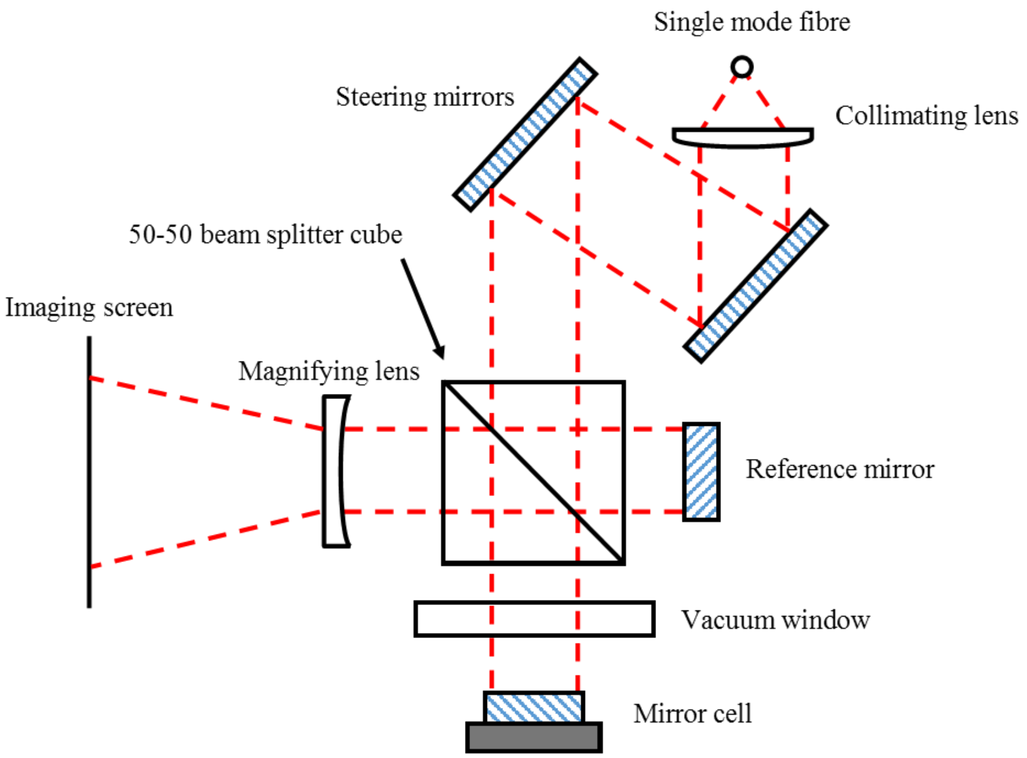

Figure 4.12: A 767 nm single mode laser is coupled into a fibre and output onto an optical bench. The light is collimated at Ø 10 mm and split into two beams using a 50-50 beam splitter. One beam is reflected from the mirror cell under test, whilst the other is reflected from a flat reference mirror. The vacuum window and the beam splitter have THORLABS –B NIR anti-reflection coatings to prevent multiple images. The test and reference mirrors are both THORLABS PF05-03 mirror blanks, which have a ground back surface to prevent multiple reflections. Recombining the beams creates an interference pattern which is imaged on a screen. A webcam placed behind the screen saves the image for analysis.

The image produced by the interferometer is a function on the phase difference between the waves travelling in each arm. For a perfectly aligned interferometer with perfect optics, the image will merely show the Gaussian profile of the laser beam multiplied by the phase difference between the arms. Any deformations of the mirror cell will distort the reflected wavefront and be imaged as lighter or darker regions in the interference pattern, which can be thought of like contours. However, in this configuration it would be difficult to quantitatively measure the flatness of the test surface, and impossible to determine the axial direction of any deformation. Instead, the reference mirror can be titled in a known direction to cause fringes to appear in the interference pattern. If the tilt angle is greater than the expected deformation, then it is possible to reconstruct the direction and magnitude of the deformation.

A commonly used unit in interferometry is “waves”. One wave is the optical path length corresponding to the 360° phase difference between two successive interference fringes, and is proportional to the laser wavelength λ. In the example shown in Figure 4.13, a tilt of 6 waves would allow the characterisation of wavefront deformations up to $6\lambda = 4602$ nm (which corresponds to surface deformations of 2301 nm). By measuring the distances between successive fringes, as well as the curvature of the fringes, it is possible to reconstruct the surface of the optic. Whilst introducing further tilt would increase the measurement range, it would reduce the resolution of the measurement as the fringes would be more difficult to trace.

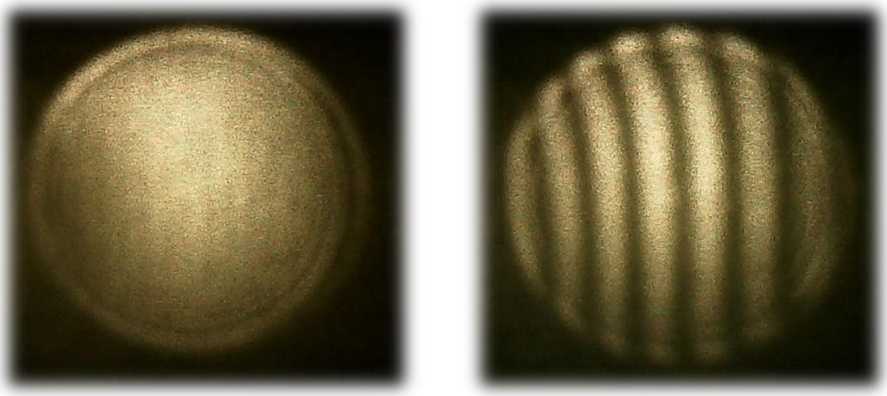

Figure 4.13: An example of two interference patterns generated by the interferometer. The image on the left has no tilt between the two mirrors, whereas the image on the right has a tilt of 6 waves. The edge of the images corresponds to the edge of the Ø10 mm laser beam.

An open source software package called OpenFringe [73] was used to trace the dark fringes and reconstruct the mirror surface in the form of Zernike coefficients (see Figure 4.14). Zernike polynomials are a set of mathematical functions that represent typical modes of deformation of a disk, and are commonly used in the optics industry. However, the extreme edges of the Zernike fits are generally considered unreliable, so when discussing the mirror deformation, we will only consider the central 95% of the Zernike fit.

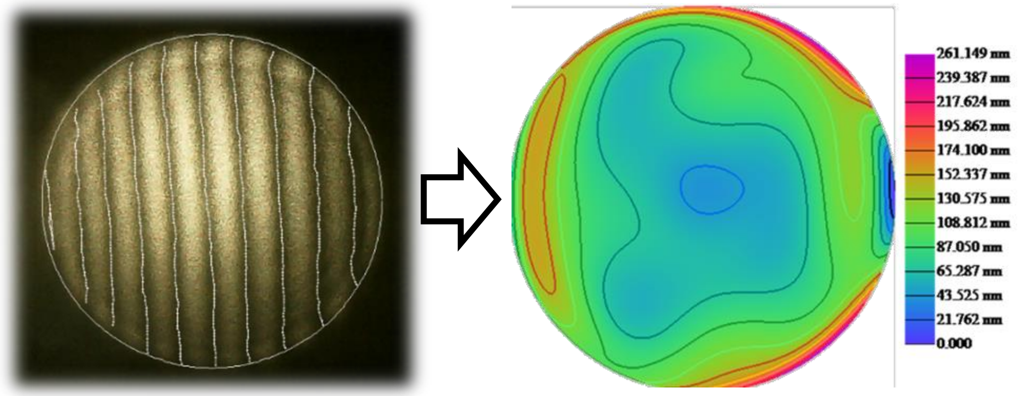

Figure 4.14: The image on the left shows the interference pattern with the dark fringes traced, and the image on the right shows a reconstruction of the surface using Zernike polynomials.

The 0.5 mm H77 titanium cell was installed in the cryostat and a measurement of the initial surface was made (Figure 4.15). The surface appears flat to within ± 100 nm which is in agreement with the 63 nm pp quoted flatness of the test and reference mirror blanks, but when cooled down to 20 K, the test mirror bulges outwards by more than 1100 nm (Figure 4.16) – recall that the image is only of the central 10 mm of the Ø12.7 mm substrate. By looking at the Zernike terms, we can identify that this deformation is almost purely a change in focal length of the mirror. This would change the beam waist within the cavity slightly, but could be fully compensated for by changing the mode matching externally. The cell was thermally cycled 3 times, with the surface measured at each room temperature and 20 K point. The defocus at 20 K appeared consistently during each cycle, but by the end of the third thermal cycle, the mirror appeared to have acquired a residual deformation of around 400 nm (Figure 4.17) at room temperature. The cell was removed from the cryostat for a visual inspection, but no damage could be identified.

The 0.5 mm T7109 titanium cell was subjected to the same tests. However, it is worth noting that the alignment of the interferometer optics and the imaging system were improved after the H77 cell tests, which may explain why this cell appears initially flatter. Figure 4.18 shows the reconstructed surface upon installation of the cell, Figure 4.19 shows the mirror surface when cooled to 20 K, and Figure 4.20 looks for residual deformation when the mirror cell is back at room temperature after thermally cycling. Within the precision of the interferometer (± ~100 nm), there was no sign of any deformation of the mirror surface during the thermal cycles. The cell was cycled a total of 5 times without showing any deformation, before it was removed and inspected for damage. After a final check to confirm that the mirror surface was unchanged between atmospheric pressure and vacuum, the cell design was approved to make the 2014 internal cavity mirrors.

The 1.0 mm gap T7109 titanium cell was also tested and showed initial promise, but the cell was discovered to have fractures around the bond line upon removal and inspection. It appears that under compression, the optic bulges but does not break. However, under tension, the optic fractures around the bond line.

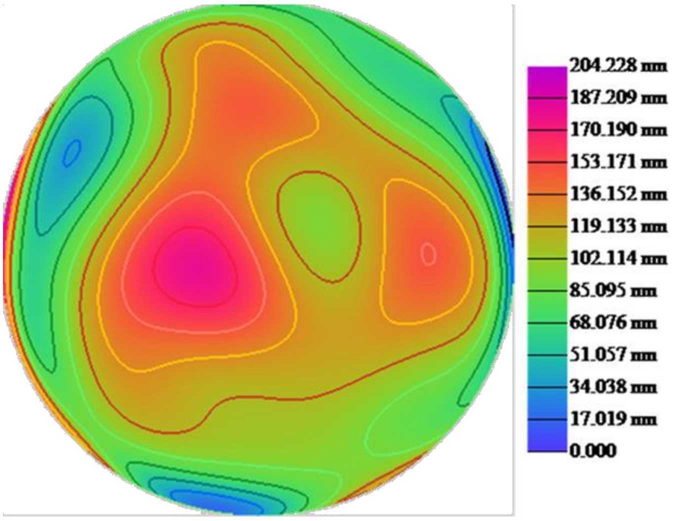

Figure 4.15: An initial measurement of the 0.5 mm H77 titanium cell. The chamber is at room temperature and under a vacuum of 1× 10^{-6} *mbar.*

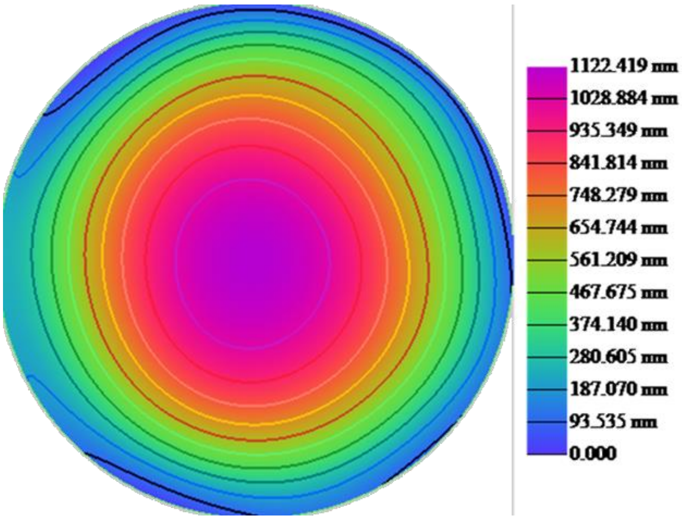

Figure 4.16: A measurement of the surface of the 0.5 mm H77 titanium cell when cooled to 20 K for the first time. The mirror appears to have bulged outwards by >1100 nm. The surface looked similar for the subsequent two cooldowns. The vacuum reaches 1× 10^{-8} *mbar when the coldhead is at 20 K.*

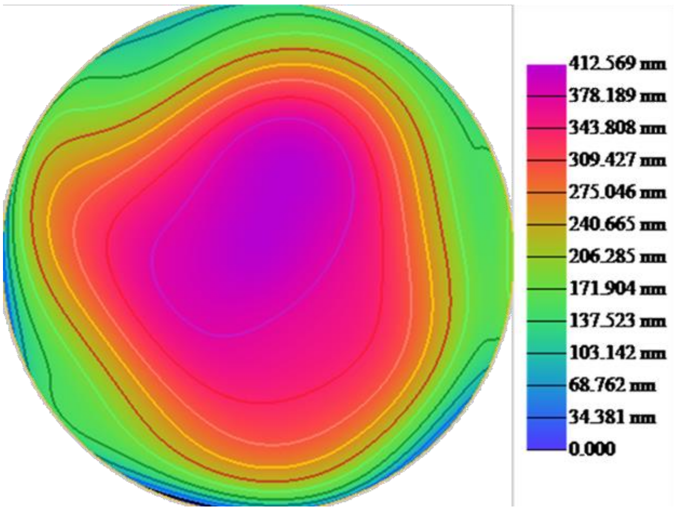

Figure 4.17: A measurement of the surface of the 0.5 mm H77 titanium cell at room temperature and still under vacuum after 3 thermal cycles. There appears to be a residual deformation of around 400 nm.

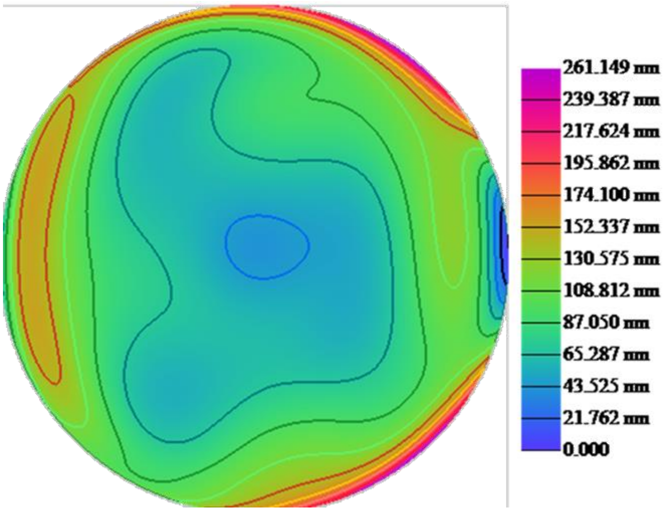

Figure 4.18: An initial measurement of the 0.5 mm T7109 titanium cell. The chamber is at room temperature and under a vacuum of 1$\times 10^{-6}$ mbar.

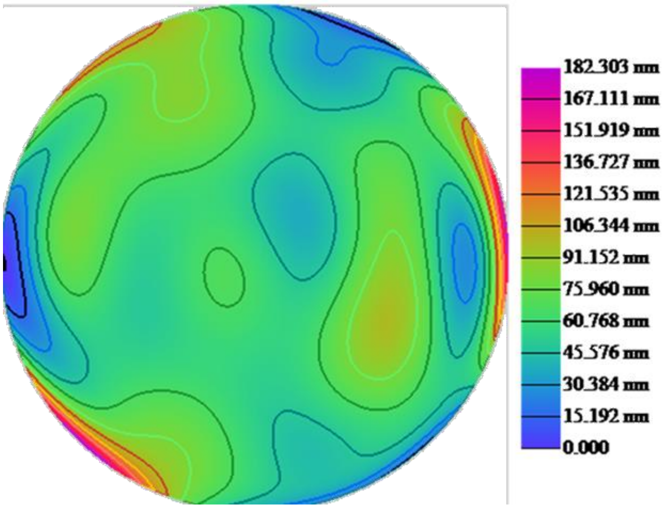

Figure 4.19: A measurement of the surface of the 0.5 mm T7109 titanium cell when cooled to 20 K. There is no obvious deformation within the precision of the interferometer.

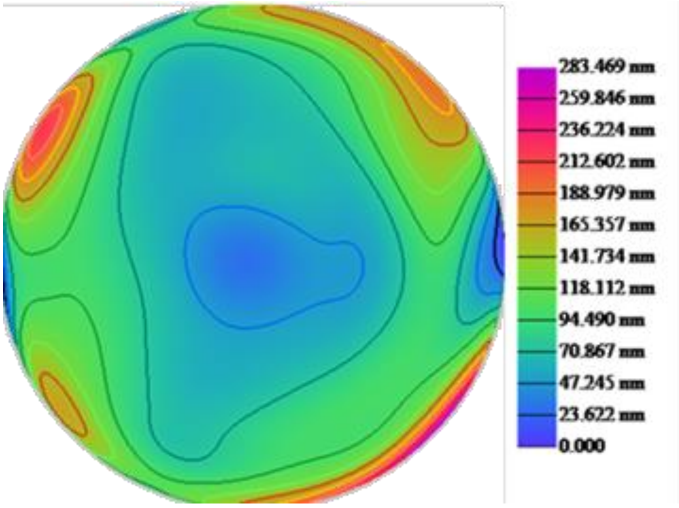

Figure 4.20: A measurement of the surface of the 0.5 mm T7109 titanium cell at room temperature and still under vacuum after thermally cycling. There is no obvious change from the initial surface.

4.2.4 Improved interferometry

After the initial success of the athermal mirror cell tests at Swansea University, and with no damage observed after multiple cooldowns of the 2014 internal cavity mirrors within the ALPHA apparatus, the test cryostat was shipped to CERN and an improved interferometer was developed. To remove the fluctuations between the laser table and the cryostat, a small optics bench was mounted directly to the cryostat. The 767 nm laser was replaced with a shorter wavelength 633 nm HeNe laser, and later a 532 nm laser (THORLABS CPS532-C2). To achieve single mode operation of the 532 nm laser, a simple temperature control circuit was implemented consisting of thermocouple and heater coil attached to the laser, and a NI USB-6001 module running a PID controller. The imaging was improved by replacing the screen and instead directly imaging on a CMOS camera chip. A 640x480 pixel webcam chip was initially used, but was later replaced by a 1280x1024 pixel (THORLABS DCC1545M) camera. An apodising filter (THORLABS NDY10B) was placed in front of the camera to convert the Gaussian wavefront into a square wavefront to increase the gain at the edge of the image whilst avoiding saturation in the middle. The reference mirror is mounted on a piezo to scan the length of the reference arm. The optics setup is shown in Figure 4.21.

In addition to controlling the laser, the NI USB-6001 module is used to control the piezo. After aligning the interference pattern with no tilt on to the camera, the piezo is scanned over several wavelengths and a video is acquired. As each pixel of the camera will record a sine wave, a fit can be used to extract the phase at the pixel. By plotting the phase differences between pixels, a 2D phase map of the wavefront and thus the mirror surface can be generated without relying on fringe tracing. A LabVIEW implementation of the Goldstein algorithm [74] is used to unwrap the phase (remove the discontinuities between 359° and 0°) and reconstruct the mirror surface. In this form, it is easy to remove tilt from the image and surface maps can be accurately

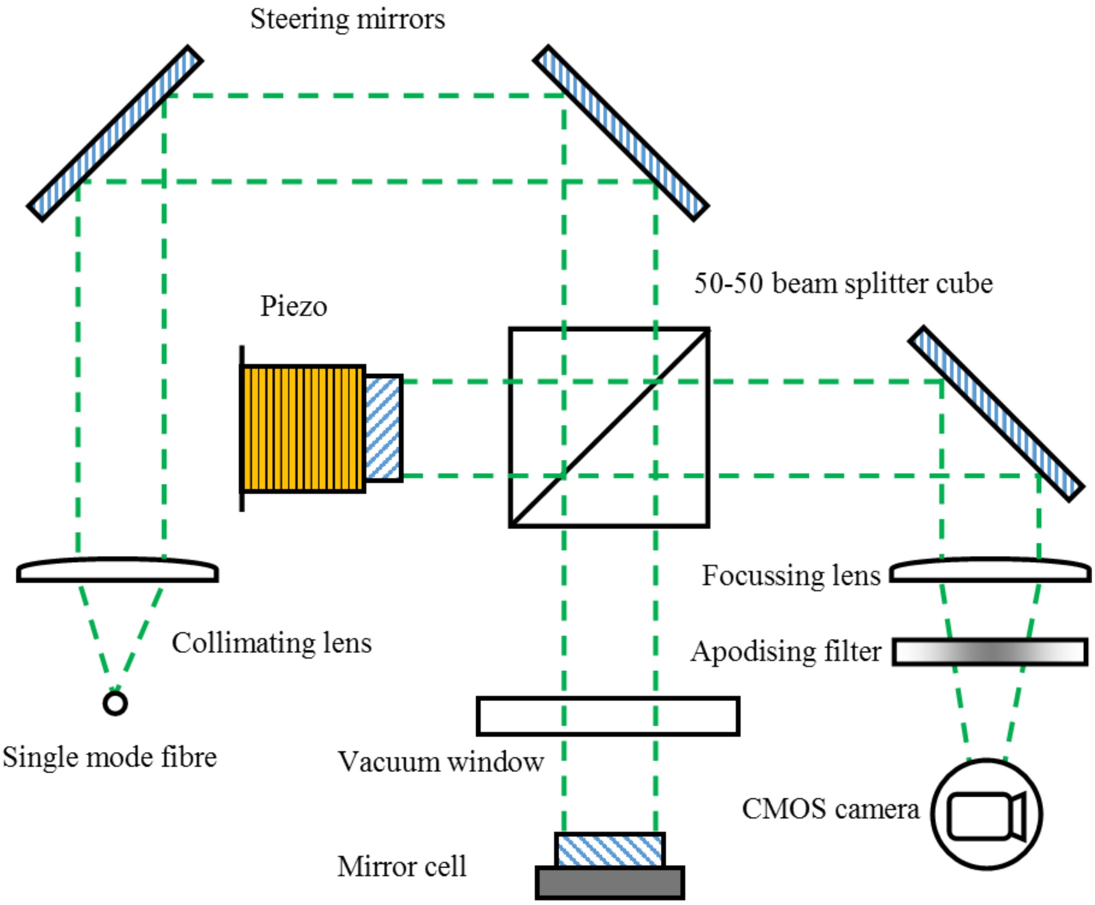
Steering mirrors
50-50 beam splitter cube
Piezo
Focussing lens
Apodising filter
Collimating lens
Single mode fibre
Vacuum window
CMOS camera
Mirror cell

Figure 4.21: In this improved interferometer setup, a stabilised 532 nm laser is coupled into a single mode fibre and output onto an optical bench which is directly mounted to the cryostat. Not shown are a 400 V piezo driver and a laptop equipped with a NI-DAQ module for controlling the piezo and acquiring images from the camera. The optics are coated for visible light and the vacuum window is wedged to prevent interference patterns from the window surfaces being imaged. The setup is designed to be as compact and lightweight as possible to avoid coupling vibrations into the cryostat.

averaged or subtracted to compare the initial and final surface shape without being limited by the quality of the reference mirror surface. Figure 4.22 and Figure 4.23 show the deformation of a mirror cell measured using this technique at 20 K and the residual deformation once the cell has returned to room temperature. The ring-like features in Figure 4.23 are due to diffraction in the test arm from the coldhead radiation shield aperture, and the striped feature is an unwanted interference pattern from other optics in the path. These effects currently limit the interferometer resolution to around 25 nm.

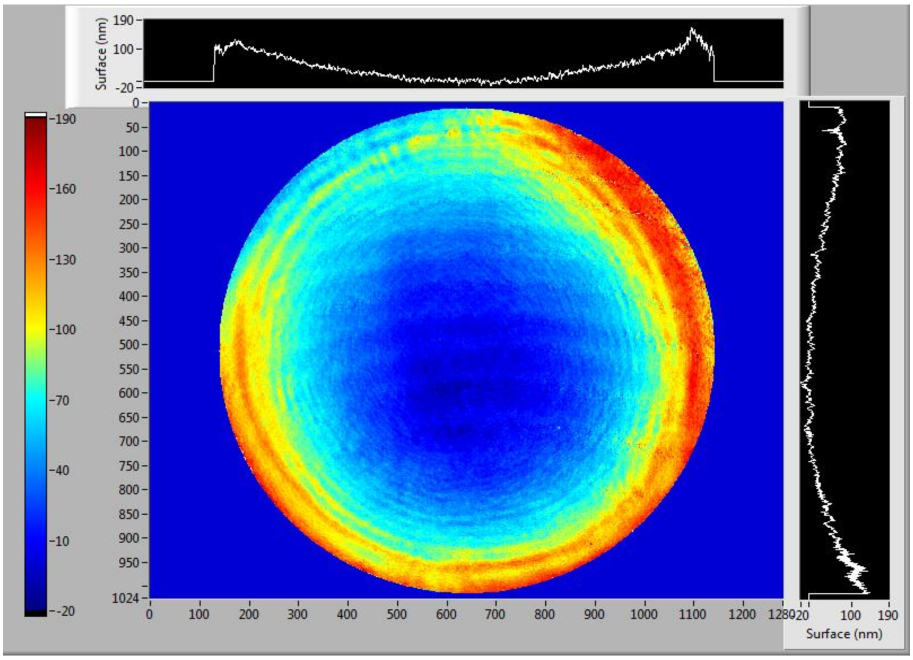

Figure 4.22: The deformation of a mirror blank in a 0.5 mm athermal cell cooled to 20 K.

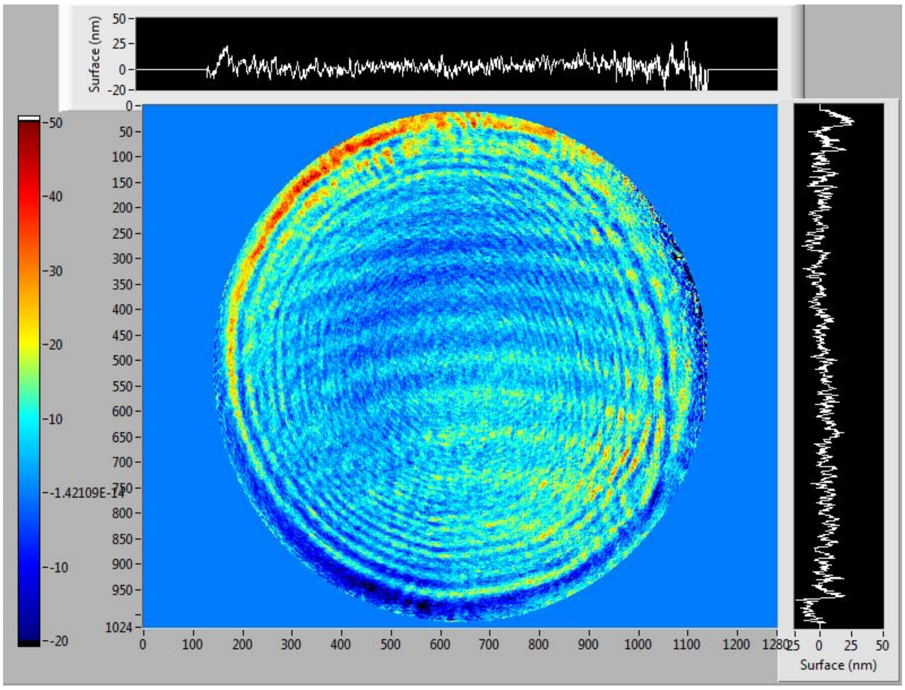

Figure 4.23: The residual deformation of a mirror blank after being thermally cycled between room temperature and 20 K.

A new batch of epoxy was ordered for manufacturing the athermal mirror cells of the 2015 cavity, which would replace the input mirrors from 2014. However, tests revealed that the 0.5 mm gap size that performed well in 2014 caused the mirrors to fracture in every case. An additional batch of epoxy was ordered and for the same gap size of 0.5 mm mirror cell design, the optic deformed by 100 nm inwards. There is a clear difference between otherwise identical cells made using different batches of epoxy, as summarised in Table 4.3.

EPOTEK T7109 batch	Optic deformation in 0.5 mm cell (nm)
2014	0 ± 100
2015 batch 1	Mirror fractures
2015 batch 2	50 ± 25
2016	-100 ± 25
2017	-130 ± 25

Table 4.3: A summary of the deformation of a 0.5 mm T7109 titanium athermal mirror cell when cooled from room temperature to 20 K, for different batches of the same epoxy.

A measurement campaign starting in 2015 and continuing in 2016 was undertaken to measure the deformation of cells with a range of radial gaps from 0.1 mm to 0.9 mm. The expiration date of the epoxy (1 year from manufacture) meant that the < 0.5 mm cells were made with the second 2015 epoxy batch, whereas the > 0.5 mm cells were made using the 2016 batch of epoxy. The results are shown in Figure 4.24.

It is thought that the mirror surface bulges due to the stress applied when the radial gap is too small, and dips due to the tension applied when the radial gap is too big. No mirrors were observed to break during this measurement run so the cause of failure is still uncertain. However, the original measurements in Swansea where the 0.5 mm cell survived but the 1.0 mm cell broke imply that the fused silica substrate fails when placed under sufficient tension.

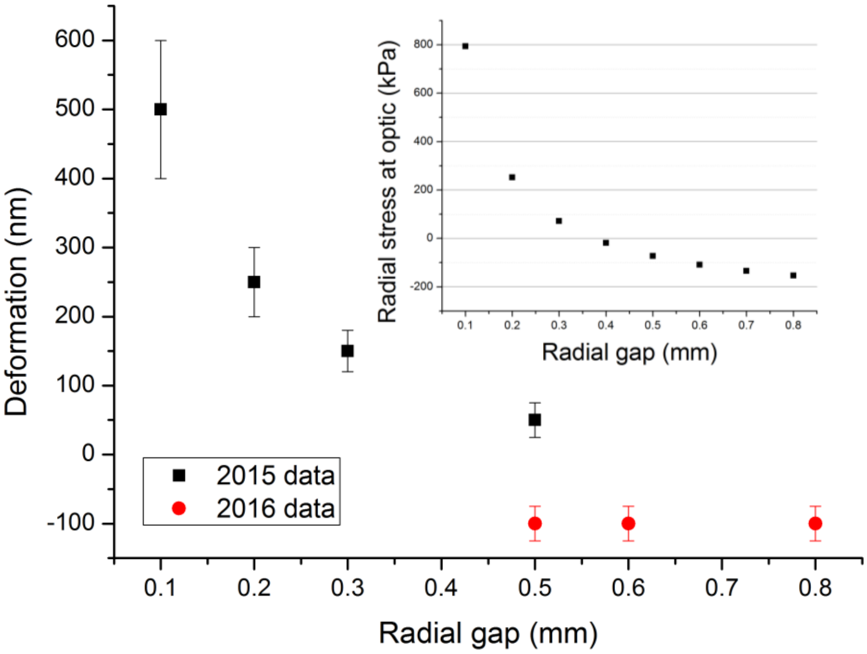

Figure 4.24: A plot of the radial gap size of an athermal cell vs the cooldown deformation of the central Ø 12 mm of the optic. A positive deformation indicates a bulging of the mirror surface. In each case, the deformation was almost purely a defocussing of the mirror. For small deformations the error is approximately the resolution of the interferometer, whereas for larger deformations, the error is dominated by knowledge of the beam size and image edge. Inset is the result of the DeLuzio stress calculation based on equation 4.30, which is in rough agreement with the trend and the zero-crossing point.

4.3 Internal cavity mechanical design

The internal cavity mirrors are situated symmetrically around the magnetic minimum trap and are separated by 90 cm. At the ends of the magnet form (shown in Figure 2.8) are a pair of structures with three precision mounted ball bearings. Triangular mirror mounts are located against the ball bearings to ensure precise and reproducible alignment (see Figure 4.25). The top leg of each triangle has a spherical surface, the left leg has a slotted surface, and the right leg has a flat surface. The upstream (with respect to the antiproton beam) triangle is held in place using a set of three bolts which contact the back of each leg. By tightening them down in the sequence top, left, right, the triangle can be reproducibly located. The bolts are made from titanium, and the magnet form and triangle are made from steel, meaning the triangle will always be held tightly in place during thermal contraction due to the smaller coefficient of thermal expansion of titanium. The downstream triangle is threaded onto a set of guide rods (visible in Figure 4.30), and beryllium-copper springs located behind the triangle apply force to keep the legs in contact with the ball bearings. The triangles contain angled slots for mounting the cavity mirrors at a 2.3° angle with respect to the trap axis. They contain two additional paths for laser access, as well as a central aperture for particles to be loaded into the trap.

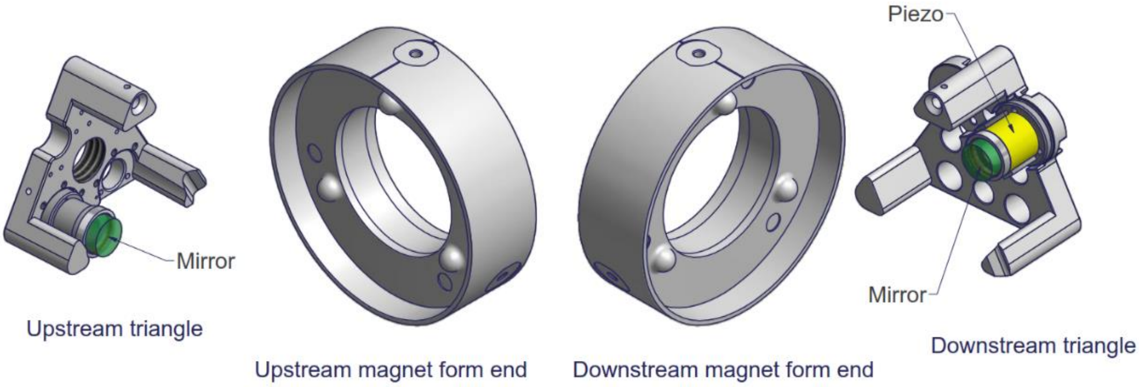

Figure 4.25: From left to right: The upstream triangle, the upstream end of the magnet form, the downstream end of the magnet form, and the downstream triangle. Both triangles contain two slots for mounting a mirror assembly, but are shown with only one mirror assembly installed.

Both cavity mirrors are bonded into an athermal mirror cell. The upstream mirror cell is epoxied directly to a stainless steel adapter piece using a thin bead of epoxy applied to the edge of the mated surfaces. The downstream mirror is epoxied atop a piezo, which is then epoxied to a shorter adapter piece. Both epoxy joints are cured simultaneously. The precise alignment required between the adapter pieces and the mirrors is achieved by making the bonds within a precision alignment jig as shown in Figure 4.26. The adapter piece is clamped from the bottom with a stainless steel base and the mirror is clamped from the top with a thin sheet of Teflon plastic. The bolt holes on the back of the jig are used to secure a thermocouple needed for monitoring the temperature of the epoxy during the curing process.

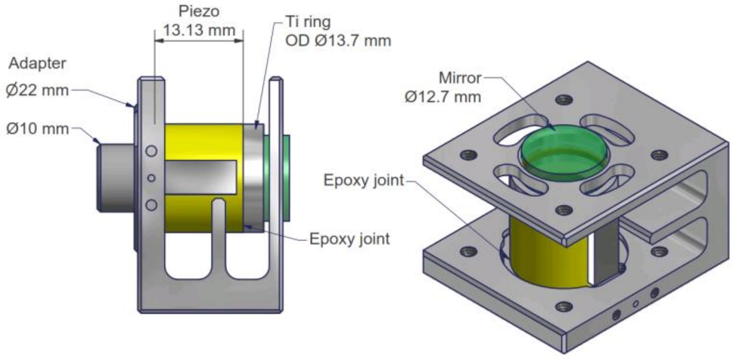

Figure 4.26: The mirror cell, piezo (yellow with grey electrodes), and downstream adapter piece mounted within the alignment jig. A similar jig is used to ensure the alignment of the upstream assembly.

The adapter pieces (shown in Figure 4.27) have a clear aperture with a diameter Ø = 8 mm, so the mirror assemblies must be aligned with a precision of approximately 4 mrad.

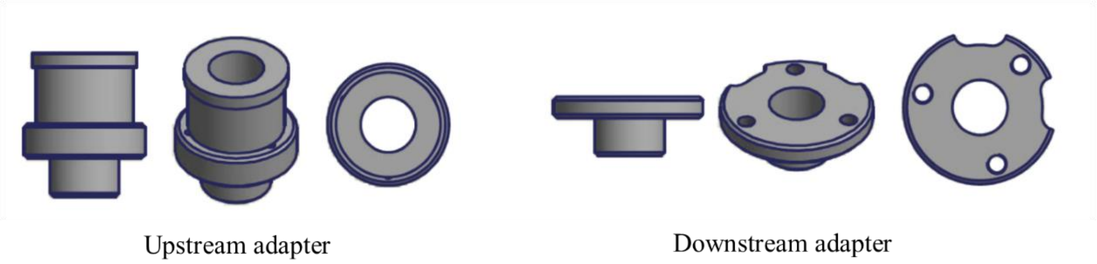

Figure 4.27: The upstream and downstream mirror adapter pieces.

For the 2014 run, a 633 nm cavity for laser-safe diagnostics and a 243 nm cavity for 1S-2S spectroscopy were installed. Both of the downstream mirrors were well aligned, but the upstream 243 nm mirror was slightly misaligned. To solve this, the mirror assembly was rotated until the misalignment direction was parallel to the axis between the top and left legs of the triangle, and the right (flat) leg was shimmed by placing several layers of aluminium foil beneath it (at the cost of misaligning the 633 nm cavity). This successfully aligned the 243 nm cavity, but a jig was manufactured to test the alignment of future cavity pieces before installation, by measuring the deflection of a laser beam as the mirror assembly was rotated in the jig.

Whilst the adapter pieces shown in Figure 4.27 worked well in 2014, after baking and cooling the apparatus in 2015, the downstream mirror (which had remained untouched since the 2014 run) had become misaligned. It was this failure which lead to the creation of an external cavity, as it was deemed too high risk to remove the Penning trap to access the mirror at the time. Upon removing the downstream triangle at the end of the 2015 beam period, both piezos were discovered to have broken away from their adapter pieces (see Figure 4.28).

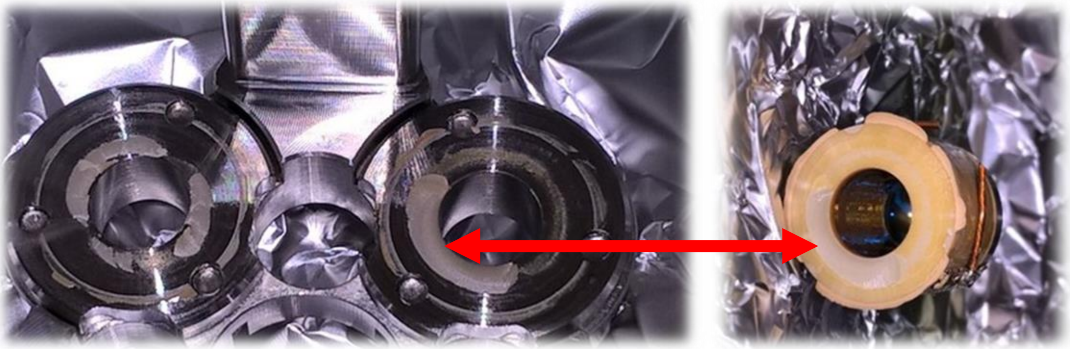

Figure 4.28: The downstream adapter pieces still mounted into the triangle (left) and one of the piezo assemblies (right). The piezos were attached to the adapter pieces by placing beads of epoxy around the outer diameter, but the piezo also seems to have bonded close to the inner diameter. Piezo material can be seen still bonded to the adapter pieces.

Although epoxy had only been applied to the outer diameter of the piezo, there was material bonded close to the inner diameter. It would appear that epoxy had either seeped beneath the piezo to form the bond, or the piezo itself had melted during the curing process. A piezo sandwiched between two metal plates was baked in an oven mimicking the curing process to test the second hypothesis, but no bond was formed. The problem was solved by simply removing material from the adapter piece to mimic the dimensions of the successful cell-piezo joint, as shown in Figure 4.29.

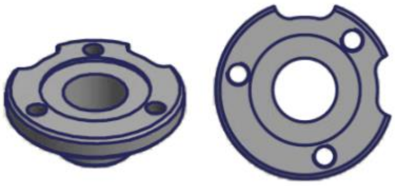

Figure 4.29: The modified downstream adapter.

For the 2016 run, the downstream Penning trap insertion structure was redesigned to make servicing the cavity possible without removing the Penning traps. During the installation with this new structure, it was realised that 4 rods which ran through the triangle to support the trap were coming into contact with the piezos (see Figure 4.30), which could also have caused the shearing of the piezos in 2015. The insertion structure was further modified to remove the rods which were coming into contact with the piezos.

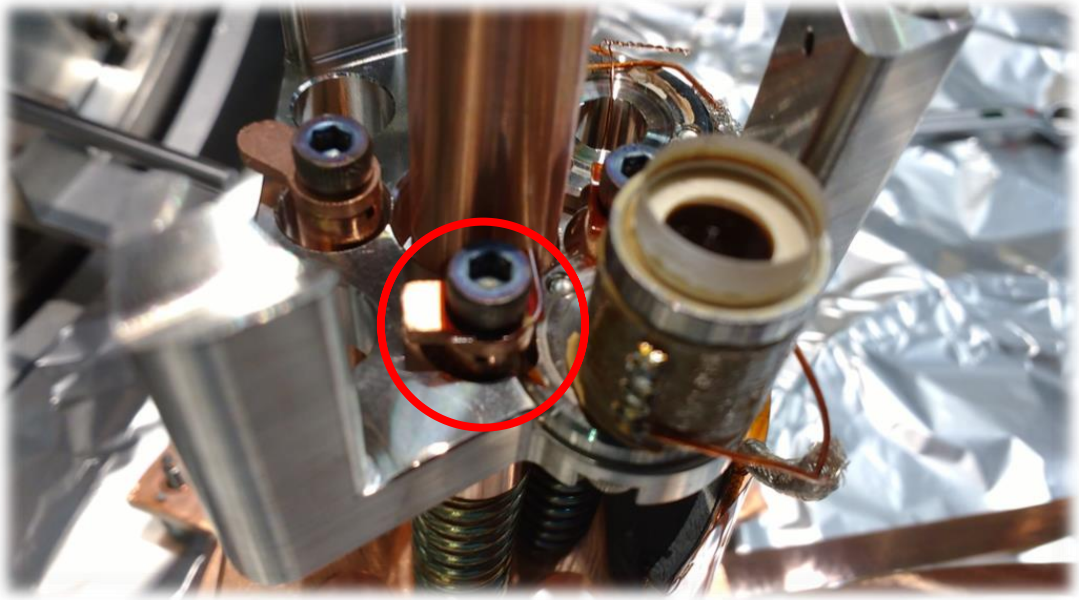

Figure 4.30: As the triangle was inserted, one of the support rods (highlighted) came into contact with the piezo assembly and sheared it off. A kapton bumper was installed to protect the piezo against knocks during installation, but this had also been sheared and epoxy had been scraped off the piezo, implying that the damage was done when holding tension was applied to the back of the triangle.

The experiment was cooled down for the 2016 run with two 243 nm cavities installed. However, one of these cavities was trialling a new method of shimming the alignment of the adapter pieces by placing small washers between them and the triangle bolt holes. This trial cavity failed to maintain its alignment, and the piezo was found to have again sheared off the adapter piece on the downstream end due to thermal gradients newly introduced by the shims. The standard cavity maintained its alignment throughout the beam period.

The piezo used is a cryogenic, UHV compatible version of the PI Ceramic PAHH+0050 with a height of 13 mm, giving a nominal 10 nm/V travel at room temperature. The travel was measured at 20 K to be 2.5 nm/V (see Figure 4.31), which is sufficient to scan the 121.5 nm free spectral range of the cavity, given the voltage limitation of 140 V set by the internal circuitry. The frequency response of the piezo-mirror assembly was measured using a network analyser whilst it was at 7 K within the ALPHA apparatus, and no resonances were observed below 10 kHz (see Figure 4.32).

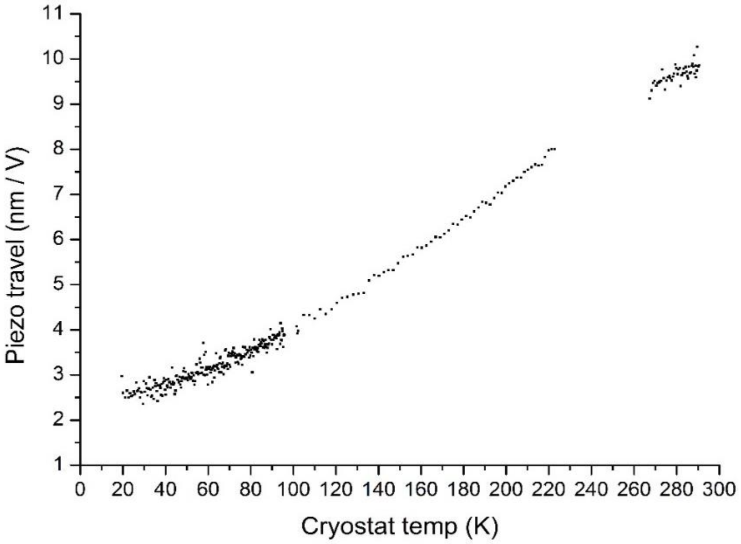

Figure 4.31: A 13 mm PI Ceramic's PAHH+0050 piezo was cooled down to 20 K on a coldhead. The travel was measured interferometrically as the piezo warmed up.

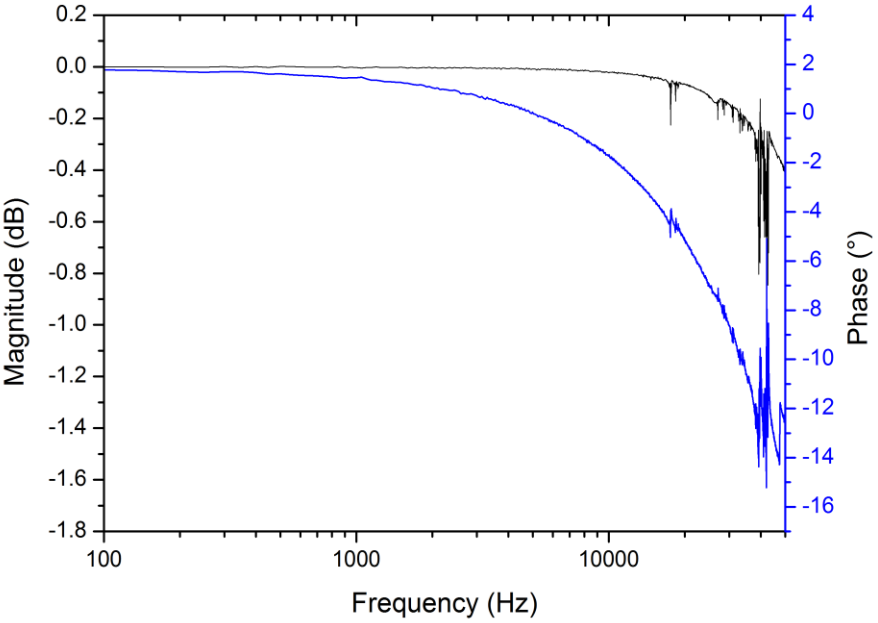

Figure 4.32: A Bode plot of the piezo electrical response at 7 K. The black curve shows the magnitude and the blue curve shows the phase of the response relative to the drive signal.

4.4 External cavity mechanical design

When the internal cavity failed during the 2015 beam period, an external cavity was quickly designed and constructed. As the cavity would now be much longer, lower reflectivity mirrors were chosen to compensate for the corresponding decrease of the linewidth and the additional noise which would be coupled into the cavity - both of which could make maintaining peak build-up more difficult.

Identical mirror assemblies were installed on both sides of the apparatus. The cavity mirror is epoxied to a piezo, which itself is epoxied to a small steel adapter piece. This adapter piece is then attached to the mirror flange, which sits between two bellows. The front bellows is bolted to the window flange of the apparatus and the rear bellows is secured to the optical table using a fixed clamp. A modified commercial mirror mount is attached to an additional flange clamp near the middle of the assembly, and is used to align the mirror. A copper support rod attached to the mirror flange guides the cabling from the piezo past the mirror to a feedthrough on another window port of the apparatus (see Figure 4.33 and Figure 4.34).

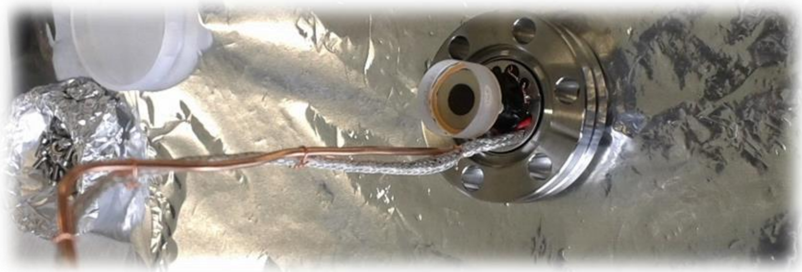

Figure 4.33: A photograph of the assembled mirror flange. The flange adapter contains holes to allow the space in the bellows behind it to be pumped, but it is an acknowledged pumping restriction. The mirror, piezo, and adapter are bonded using EPOTEK T7109 epoxy.

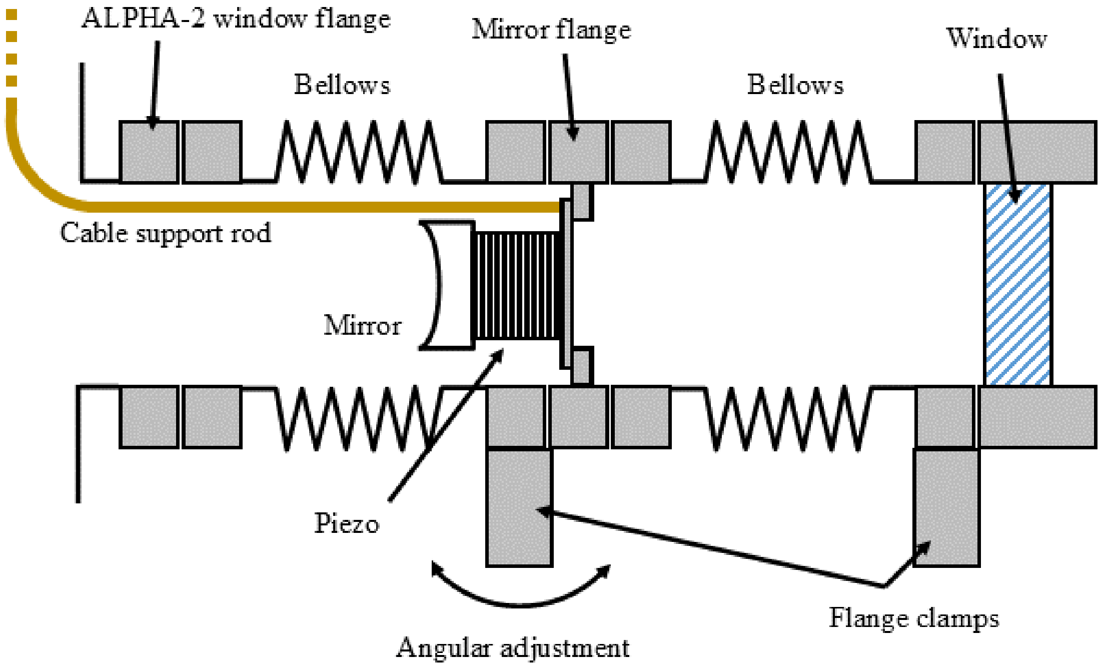

Figure 4.34: The mirror is mounted on a piezo between two bellows. The window is clamped in place, allowing the mirror flange to be titled using a modified commercial mirror mount.

However, there were two major problems with this design: Firstly, the bellows were much stiffer than anticipated, and the springs in the mirror mount were not strong enough for it to be able to apply any force on the mirror flange. Secondly, the vibrations and slow drifts of the optical tables would cause the cavity to become misaligned after minutes, and be impossible to lock. These problems were solved by removing the connection to the optical table and instead securing the end bellows to the beamline as shown in Figure 4.35. M4 threaded rods were used to connect the two flange clamps, and create a basic but effective alignment mechanism (see Figure 4.36).

Even with the improved mounting structure, locking the cavity was still challenging. By locking the laser to the cavity, the FWHM of the length fluctuation was measured to be around 400 nm over 100 s (see Figure 4.37). For comparison, the length fluctuation of the internal cavity was around 10 nm. By driving one piezo with a slow but quiet amplifier to correct the large fluctuations, and driving the other piezo with a carefully filtered fast driver, the cavity was successfully locked with > 90% efficiency.

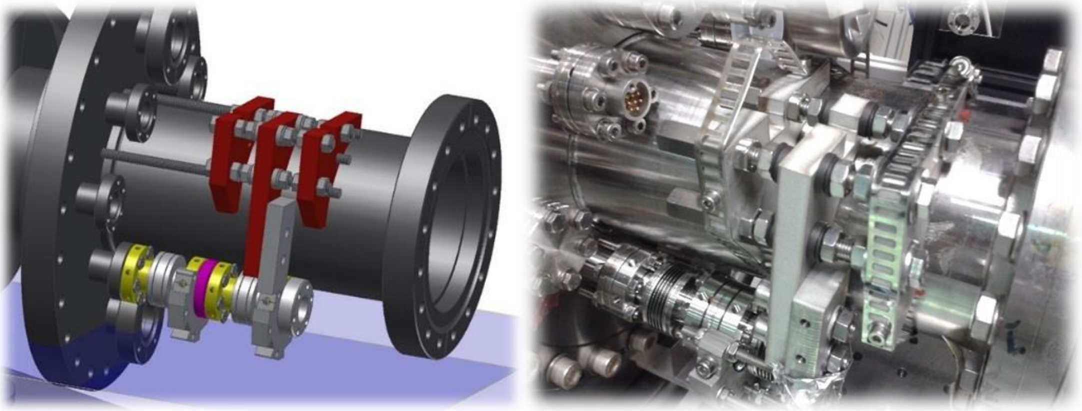

Figure 4.35: An Autodesk Inventor rendering (left) and photograph (right) of the structure designed to clamp the external cavity assembly to the beamline. The vacuum window is not shown.

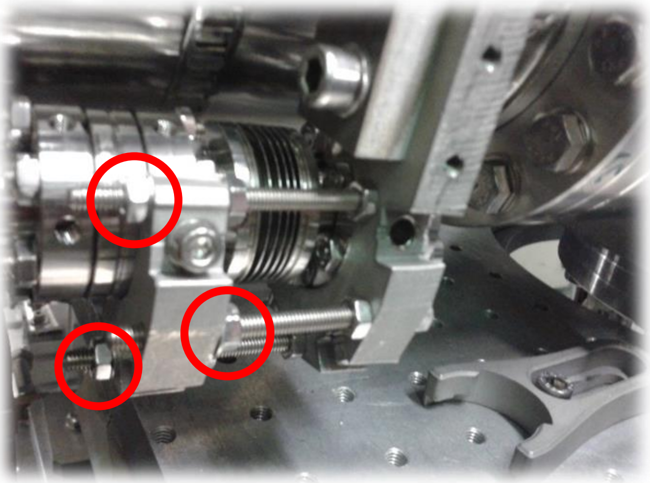

Figure 4.36: The highlighted nuts on the M4 threaded rods were loosened or tightened to adjust the alignment of the cavity mirror.

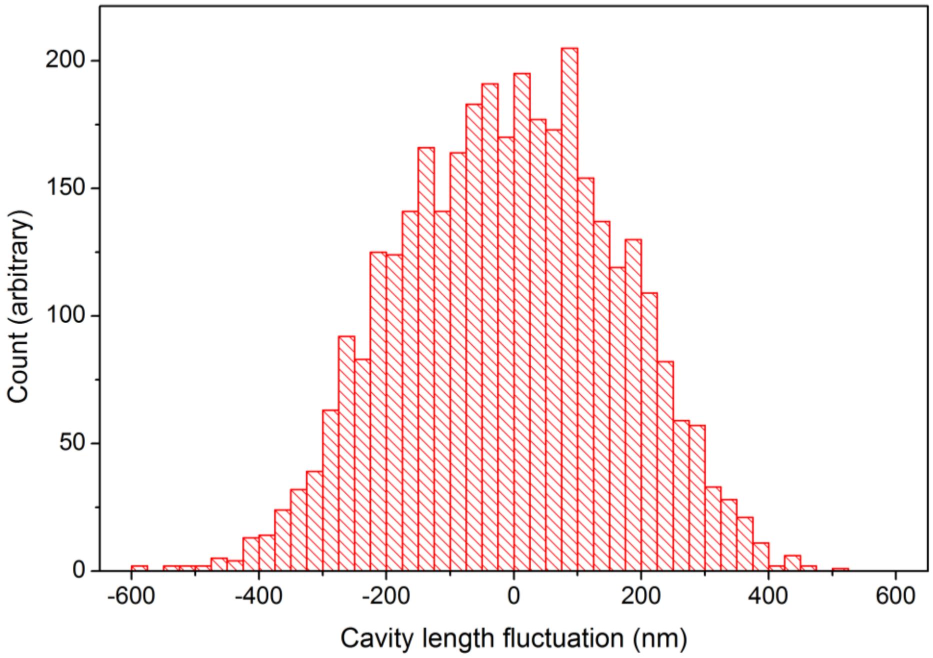

Figure 4.37: A histogram of the cavity length fluctuation in nm over 100 s, as measured by a wave meter when the laser was locked to the external cavity.

4.5 Optical design

The 243 nm cavity mirrors are from the manufacturer LASEROPTIK GMBH. The internal cavity mirrors have a radius of curvature of 1 m, forming a sub-confocal cavity when separated by only 90 cm. Similarly, the external cavity mirrors have a 3 m radius of curvature and the cavity has a length of 270 cm. This is useful because transverse modes become separated in the frequency domain (see Figure 4.38), allowing for much simpler alignment and elimination of undesired modes within the cavity. Whilst the transverse modes of a confocal cavity could be identified with a camera, forming a perfectly confocal cavity within the ALPHA apparatus is difficult due to the tight space constraints, and hence, inability to install any active alignment. This is important because a cavity which is extremely close to being confocal will have modes which are not fully frequency degenerate and interfere with the fundamental mode, reducing the effectiveness of many locking schemes (e.g. PDH).

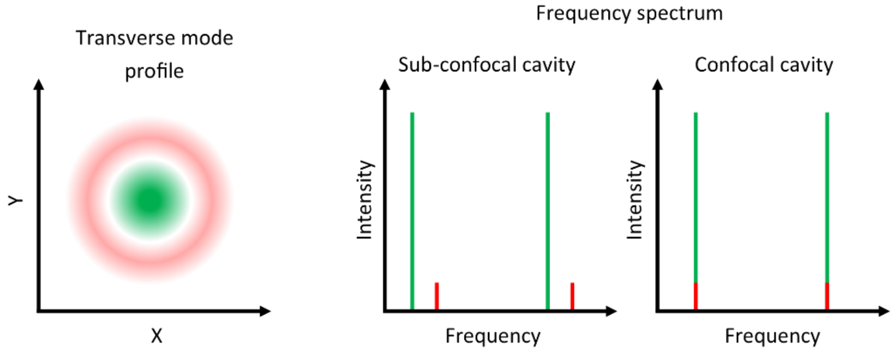

Figure 4.38: In a confocal cavity, transverse modes (red) are frequency degenerate as all path lengths are equal. As the cavity is made longer or shorter, the transverse modes will separate.

In 2014, two identical 0.995 reflectivity mirrors were used to form the internal cavity, giving a design finesse of 627. However, it was discovered that these mirrors had a transmission of only 0.00043, and as such, a maximum enhancement factor of only 17 was predicted. With 50 mW of laser power, even in perfect conditions the cavity would have been unable to produce more than 850 mW of circulating power.

The input coupler was replaced for the 2015 antiproton beam period, but the failure of the piezo joint meant that an external cavity was installed and operated instead. This cavity used two 0.985 reflectivity mirrors with a transmission of ~0.015. Lower reflectivity mirrors were chosen as it was believed locking the external cavity would be significantly more difficult due to mechanical noise. These mirrors were predicted to form a cavity with a finesse of 208 and an enhancement factor of 65, so with 50 mW of laser power, a maximum circulating power of 3.25 W was attainable. Accounting for mode matching and lock quality considerations, we aimed for a circulating power of 2 W.

In 2016, the piezo joint problem was solved, and an internal cavity consisting of an input coupler with a reflectivity of 0.99 and transmission of 0.0075 and a 2014 output coupler ($R = 0.995$) was installed. This cavity was designed to have a finesse of 417 and an enhancement factor of 132, meaning that with 50 mW of incident laser power, a maximum circulating power of 6.6 W would be achievable (again, with the aim to run the cavity at 2 W). The design parameters are summarised in Table 4.4.

	2014	2015	2016
Configuration	Internal	External	Internal
Length	90 cm	270 cm	90 cm
Mirror reflectivity	Input: 0.995 Output: 0.995	Input: 0.985 Output: 0.985	Input: 0.990 Output: 0.995
Mirror transmission	Input: 0.00043 Output: 0.00043	Input: 0.015 Output: 0.015	Input: 0.0075 Output: 0.00043
Design Finesse	627	208	417
Enhancement factor	17	65	132
w_0	0.196 mm	0.340 mm	0.196 mm

Table 4.4: The enhancement cavity design parameters.

4.6 Performance

2014 marked the first successful cooldown of an internal cavity and injection of 243 nm light into the apparatus. The finesse was measured to be 717 ± 80, and there was no evidence of mirror degradation throughout the year. An error signal was produced using the amplitude modulation technique, but the lock quality was very poor at just 15% of the peak power. The low transmission of the input coupler meant that less than 3% of the laser power was coupled into the cavity, and the maximum circulating power was < 0.13 W. P_0 was measured to be 50 mW before the vacuum window, but the actual power reaching the cavity was likely to be lower than this due to laser induced damage of the window which was not discovered until 2015.

2015 saw the use of an external cavity with a high level of environmental noise. Although making a finesse measurement with a cavity fluctuating by several free spectral ranges was difficult, comparing the cavity linewidth with the sideband spacing imposed by the electro-optic modulator placed the finesse at 125 ± 15, which was significantly lower than expected. The laser power reaching the cavity was reduced by a factor of 2 due to degradation of the vacuum windows, which were not made of a sufficiently good UV grade fused silica. Combined with the reduced finesse, this ultimately limited the circulating power to 0.45 ± 0.05 W. The average circulating power as calculated from the transmitted power method (equation 4.26) agrees well with both the measured finesse and the average circulating intensity as calculated using the enhancement factor method (equation 4.25), if the reflectivity of both mirrors has fallen to 0.972.

In 2016 an internal cavity was installed, and the vacuum windows were replaced with an improved grade of UV fused silica glass. The measured finesse of the cavity was initially around 400, but degraded to around 200 after the apparatus was baked. During subsequent bake-outs, the finesse fell further to 110. The finesse was recovered to 230 by running the cavity in an oxygen rich environment (which we will discuss in section 4.7), and the laser power was increased to 140 mW by replacing a damaged frequency doubling stage. However, even with this increased power, only 45 mW was estimated to reach the enhancement cavity due to additional losses along the beam path. The average circulating power as calculated using the transmitted power method can again be made to agree with the measured finesse and the average circulating power as calculated using the enhancement factor method if the input coupler reflectivity has fallen to 0.975. Table 4.5 summarises these measurements.

	2014	2015	2016
Configuration	Internal (90 cm)	External (270 cm)	Internal (90 cm)
Estimated P_0	< 50 mW*	25 ± 5 mW	45 mW
Measured finesse	717 ± 80	125 ± 17	230 ± 20
Measured coupling	0.03	0.65	0.7
Enhancement factor	17	19	33
Lock type	AM	PDH	PDH
Measured Q_{lock}	0.15	0.9	0.75
Measured P_t	Not measured	7 ±1 mW	0.45 ± 0.03 mW
Estimated P_{avg}	< 0.13 W*	0.45 ± 0.05 W	1.05 ± 0.1 W
Estimated I_0	< 215 W/cm^2*	250 ± 25 W/cm^2	1740 ± 165 W/cm^2

Table 4.5: A summary of the cavity performance. Values marked with (*) were not well characterised as contributing effects were not discovered until later. The measured coupling is the ratio of injected to reflected light, and hence is a function of both the impedance mismatch and spatial mode matching.

4.6.1 Loss versus reflectivity

The 2014 mirrors were observed to have a higher than expected loss (compared to typical visible-light cavity mirrors), which meant that relatively little light could be coupled into the cavity. To compensate for this in subsequent years, the reflectivity of the input coupler was lowered and the mirror was annealed by heating it after the coating process.

Table 4.6 shows the measured reflectivity and transmission of the mirrors received from LASEROPTIK. Lowering the reflectivity seems to additionally reduce the loss. Annealing the mirrors is also beneficial. This observation implies that choice of mirror reflectivity is already reasonably well optimised. The transmission measurements were made with a 243 nm beam at a 0° angle of incidence by placing a calibrated diode power meter before and after the mirrors.

Batch	Specified reflectivity	Measured transmission	Loss (1-*R*-*T*)
2014 non-annealed	0.995	0.00043	0.00457
2015 non-annealed	0.985	0.0135	0.0015
	0.99	0.074	0.0026
2015 annealed	0.985	0.015	0
	0.99	0.0075	0.0025
2017 annealed	0.985	0.015	0
	0.99	0.0077	0.0023
	“HR”	0.00033	-

Table 4.6: Measurements of the mirrors delivered to ALPHA. The “HR” mirror was specified for maximum reflectivity. The measured transmission is an average over several mirrors from each batch in new condition, including substrate losses. The variance between mirrors is approximately ± 5%.

4.6.2 Laser induced damage

After the 2015 run with the external cavity, a loss of power of 50% in the upstream window and 20% in the downstream window was discovered. There were likely to be similar losses in the 2014 upstream window. The source of these losses was UV induced degradation of the glass. Figure 4.39 shows a large 243 nm beam passing through the 2015 upstream window. The damaged section is clearly visible, as it fluoresces less.

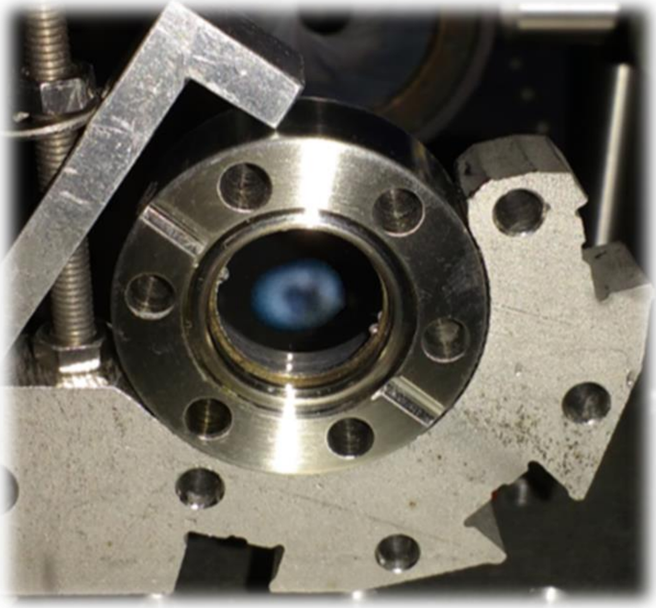

Figure 4.39: A photograph of the 2015 upstream window mounted on the bench. A large diameter 243 nm beam was sent through and the transmission was measured using a CCD camera. The laser induced damage can already be seen by the dark spot within the blue fluorescence.

The UV degradation occurred because the windows were made from a standard grade of fused silica glass. Several UV-compatible grades of fused silica are available, of which Corning 7980 KrF has the best transmission at 243 nm, coupled with good resistance to laser induced damage [75]. Although the 2016 windows were manufactured from this glass, the transmission had dropped by 30% where the beam had been passing through when they were measured at the end of the year.

In addition to the damage to the window, a small burnt spot was discovered on the antireflection coating of the 2016 input coupler (shown in Figure 4.40). Transmission through this part of the mirror was 30% lower than the transmission through other parts of the mirror. No damage was observed on the high reflectivity side of the mirror, or on either side of the output coupler.

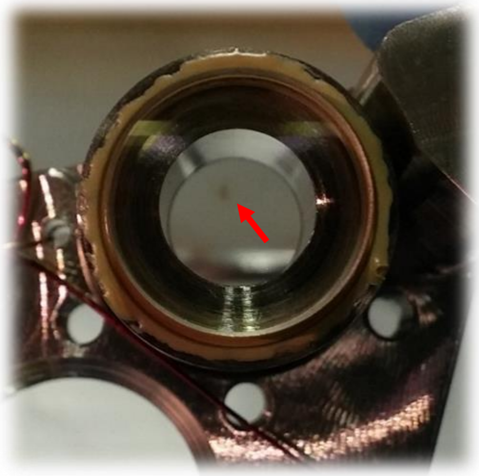

Figure 4.40: A small burn spot is present on the AR coating of the upstream mirror.

4.6.3 Spatial mode matching

The spatial mode matching was generally good for both the internal and external cavities. Figure 4.41 shows the mode structure of the 2016 cavity as the piezo is scanned to cover a free spectral range, which is typical of all three years. The upper trace shows the demodulated PDH signal, and the lower trace shows the intensity transmitted through the cavity. A small number of transverse modes are present, with a summed intensity of less than 10% the intensity of the fundamental mode. The PDH signal is skewed slightly due to the presence of a nearby transverse mode.

The transmitted beam is split so that one half is focussed onto a photodiode and the other half is imaged on a paper screen by a webcam. The webcam is used to aid alignment and confirm that the cavity is operating at the fundamental mode, although the image saturates when the cavity is locked. After locking the cavity for more than 10 seconds, higher order transverse modes begin to be excited (as shown in Figure 4.42). This is thought to be due to thermal lensing in the path between the laser lab and the apparatus, which we will discuss in more detail in chapter 5. The amplitude of these higher order modes was later measured to be 4% of the fundamental mode using a non-saturated beam profiler.

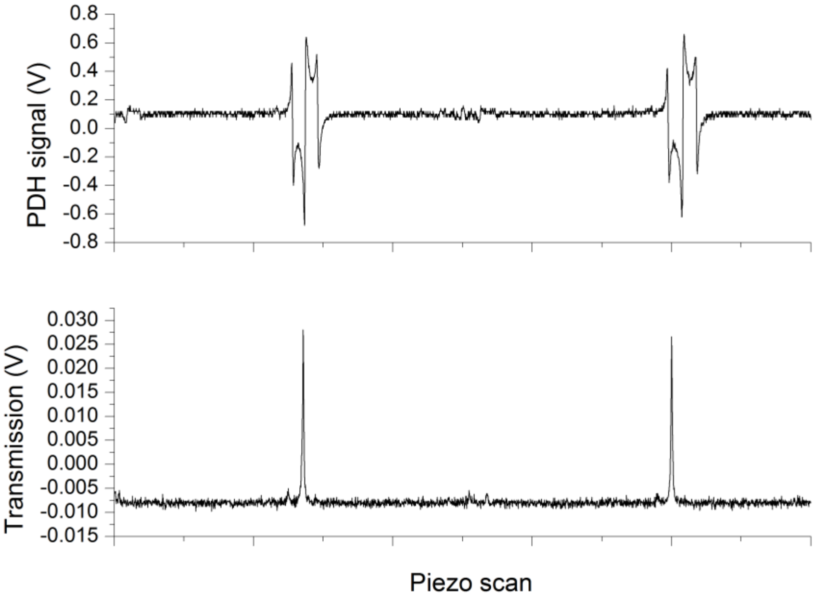

Figure 4.41: The PDH error signal (upper) and the transmitted intensity (lower) as the piezo is scanned linearly over 50 V to cover a full free spectral range of the cavity.

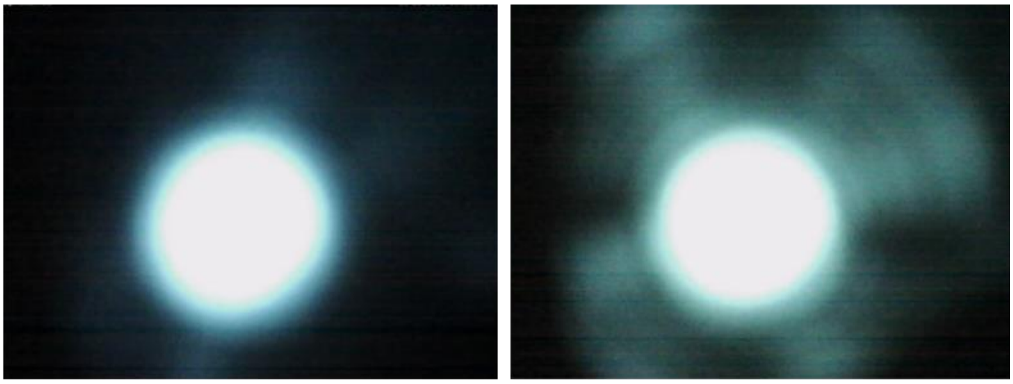

Figure 4.42: A saturated image of the transmitted beam when the cavity has been locked on resonance for 1 s (left) and 30 s (right).

4.7 Mirror degradation and recovery

Both the external cavity in 2015 and the internal cavity in 2016 suffered from a reduction in finesse. A study by Gangloff et al. in 2015 [76] found that high finesse cavities which used oxide based mirror coatings suffered from vacuum degradation, due to oxygen depletion on the surface. They typically observed finesse losses of factors of 3 or more, and the loss was not proportional to the light intensity. The loss rate was significantly higher at elevated temperatures however, which agrees well with the observation of the finesse falling after baking the ALPHA apparatus, but not during the experimental runs at 7 K.

A technique for regenerating the mirrors using a pure oxygen environment is also presented in the paper. The regeneration is supposedly enhanced by higher temperatures and higher pressures, and greatly accelerated by shining UV light on the mirrors. In an attempt to regenerate the 2016 cavity mirrors, the apparatus was filled with synthetic air consisting of 75 mBar of nitrogen and 25 mBar of oxygen. The temperature was increased to 80°C and the cavity was locked for 2 hours. After pumping out the gas and cooling down to 7 K, the finesse was measured to have improved by a factor of 2 from 110 ± 10 to 230 ± 20.

The paper also found that a 1 nm final coating of SiO_2 could significantly reduce the rate of degradation, and a 100 nm layer could prevent it completely. It is important to note that the $R = 0.995$ mirrors used in the 2014 internal cavity did have a final SiO_2 coating and were not observed to degrade, whereas both mirrors of the 2015 external cavity and the upstream mirror of the 2016 cavity lacked the final SiO_2 layer, and were observed to degrade.

5 The 1S-2S Laser System

The antihydrogen 1S-2S laser system is based on the setup used by Hänsch et al. [49] for hydrogen spectroscopy. At the heart of the setup is a Toptica TA-FHG pro laser, which can produce up to 200 mW of 243 nm light. The laser is locked to a reference cavity for stability, and related to atomic time using a GPS-disciplined frequency comb. The 243 nm beam is delivered along a 7 m actively stabilised path to the enhancement cavity, which is locked to the laser frequency using the PDH technique. Figure 5.1 shows a schematic of the setup.

5.1 243 nm light generation

A commercial Toptica TA-FHG pro laser (shown in Figure 5.2) generates high intensity 243 nm light by twice frequency doubling a tuneable 972 nm DL pro extended cavity diode laser. The standard DL pro consists of a diode in a Littrow configuration cavity which boasts a free running linewidth of 100 kHz [61]. The laser frequency can be tuned by changing the temperature of the diode (coarse), changing the angle of the extended cavity diffraction grating (coarse), or changing the diode current (fine). The DL pro has a mode hop free tuning range of >20 GHz [61], meaning the frequency can be tuned without suddenly jumping a free spectral range to a different cavity mode with higher gain. Our custom DL pro has a longer cavity to reduce the free running linewidth and reach sub-Hz performance when locked to an ultra-stable reference [77], but the mode hop free tuning range is reduced to around 1.5 GHz. This is still sufficiently large that the laser can be ramped between the c-c and d-d transition frequencies without mode hopping.

A tapered amplifier (TA) driven at 4 A boosts the 972 nm intensity from 50 mW to 2.5 W. Optical isolators are placed after the DL pro and TA to prevent feedback. A single EOM placed after the TA adds 5 MHz sidebands to the light, which are used to actively stabilise the length of two frequency doubling cavities via the PDH locking

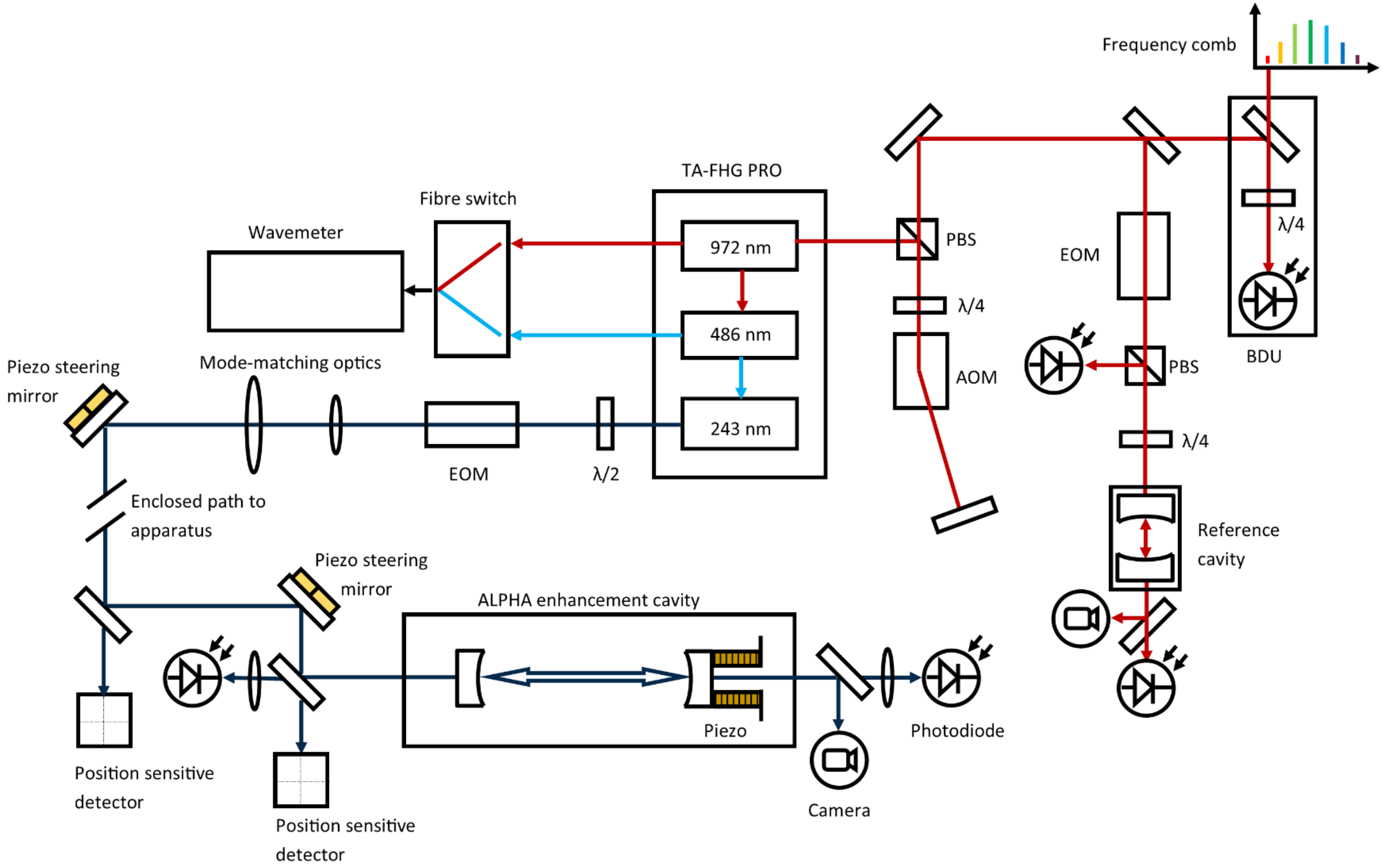
Frequency comb
TA-FHG PRO
Fibre switch
Wavemeter
972 nm
486 nm
243 nm
PBS
λ/4
AOM
EOM
BDU
λ/4
PBS
λ/4
Reference
cavity
Piezo steering
mirror
Mode-matching optics
EOM
λ/2
Enclosed path to
apparatus
Piezo steering
mirror
ALPHA enhancement cavity
Piezo
Photodiode
Camera
Position sensitive
detector
Position sensitive
detector

Figure 5.1: A schematic of the optical elements in the 1S-2S spectroscopy setup. The red, cyan, and navy blue lines show the propagation of the 972, 486, and 243 nm light respectively. Some steering mirrors have been removed for simplicity.

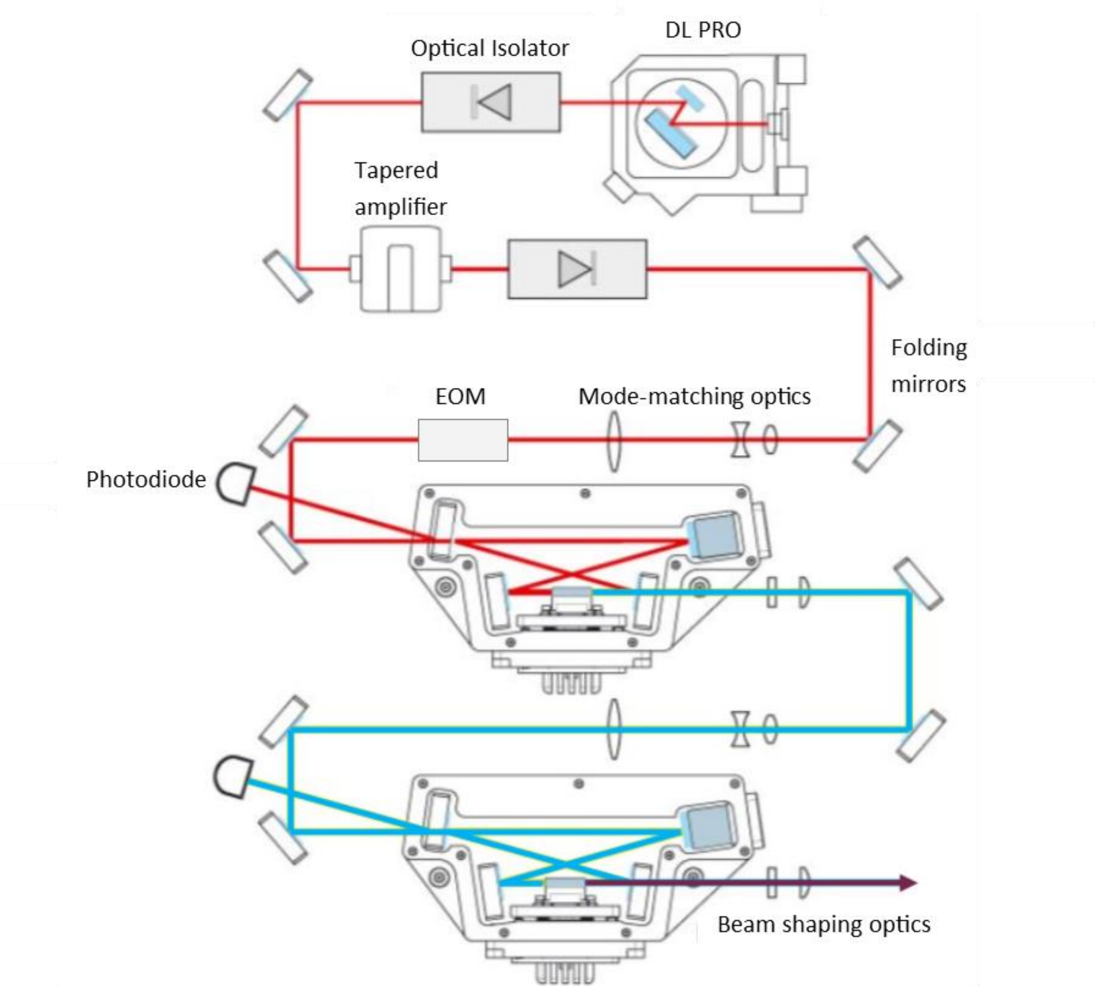
DL PRO
Optical Isolator
Tapered amplifier
Folding mirrors
EOM
Mode-matching optics
Photodiode
Beam shaping optics

Figure 5.2: The internal layout of the Toptica TA-FHG pro laser, which generates the high power 243 nm light for antihydrogen spectroscopy. Image modified from [61].

technique [65]. The second harmonic generation (SHG) cavity produces 1.2 W of 486 nm light and the fourth harmonic generation (FHG) cavity can produce as much as 200 mW of 243 nm light (when new). In practice, the FHG cavity output is reduced to 140 mW or lower to obtain a high quality beam and reduce damage to the crystal and output optics. To minimise the impact of damage to the FHG optics, the beam is periodically walked within the cavity to an undamaged spot. The entire FHG cavity was replaced in 2016 once it was no longer possible to tune the output power to above 100 mW. Meanwhile, the SHG cavity output power has dropped by less than 10% in 3 years of operation. The sidebands from the internal EOM are not present at any detectable level in the 243 nm beam. Using a THORLABS BC106N-UV beam profiler, the 243 nm beam was measured to have a beam waist ($1/e^2$ radius) of 228 µm at a distance of 1.28 m from the laser face, and an M^2 value close to 1.

5.2 Frequency control and metrology

The 972 nm laser light is shifted to the reference cavity frequency using an acousto-optic modulator (AOM) in double-pass configuration. The frequency of the reference cavity is continuously monitored by a frequency comb and fed into a frequency controller. This is a LabVIEW program which calculates the 1S-2S transition frequencies (equations 3.13 and 3.14) using the latest measurement of the magnetic field within the apparatus, subtracts the reference cavity frequency, and corrects the AOM frequency accordingly at a rate of 1 Hz. Two state selection bits allow triggering of the frequency controller to ramp the AOM between the c-c and d-d transitions, and select if the laser frequency is exactly set to the calculated resonance, or offset by a pre-programmed value.

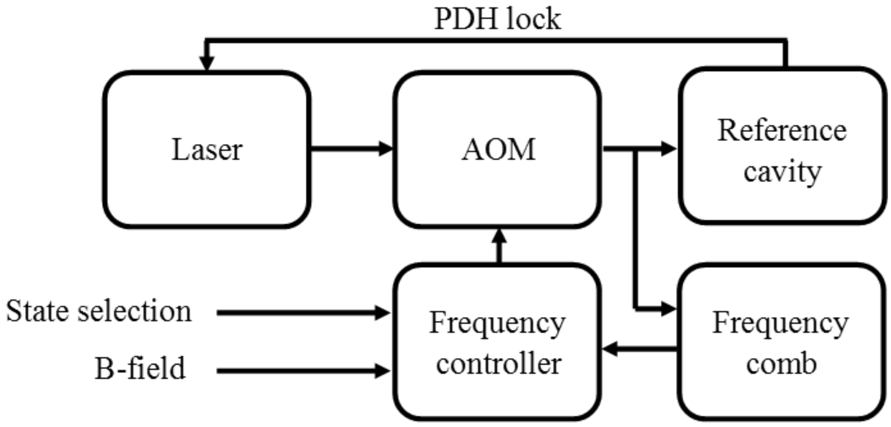

Figure 5.3: A flow chart of the frequency control setup.

5.2.1 Reference cavity

The laser is locked to a high finesse reference cavity made with an ultra-low coefficient of thermal expansion (ULE) glass. The cavity was manufactured by Menlo Systems and is based on the ORS 1500. The cavity is suspended within a temperature controlled vacuum chamber, which itself is located within an acoustically dampened enclosure, and sits upon an active vibration control module (Accurion Vario series).

The 972 nm light is brought by fibre onto a bench mounted to the vacuum chamber, which holds an EOM and mode matching optics, as well as polarisation optics and a detector for generating the PDH error signal. The cavity has a linear drift (due to length contraction) of 53 mHz/s, which is typical for ULE glass as it shrinks due to a recrystallization process [78]. To lock the laser to the reference cavity, a Toptica Digilock 110 module is used to servo the high frequency noise by acting on the diode current, and the larger amplitude, low frequency shifts (e.g. when the AOM is being ramped) by acting on the internal grating of the DL pro.

The short term linewidth of the laser can be estimated by making the assumption that the frequency fluctuations of the locked laser are the dominant source of the linewidth broadening and not the frequency fluctuations of the cavity. By shifting the set point of the lock by ± 1 FWHM of the measured noise of the PDH error signal (DC-40 MHz sensitivity), a frequency difference of 1.0 kHz was measured by the frequency comb, giving the laser a FWHM linewidth of 500 Hz at 972 nm and, in a worst-case extrapolation through the frequency doubling cavities, 2.0 kHz at 243 nm. The measurement data is shown in Figure 5.4.

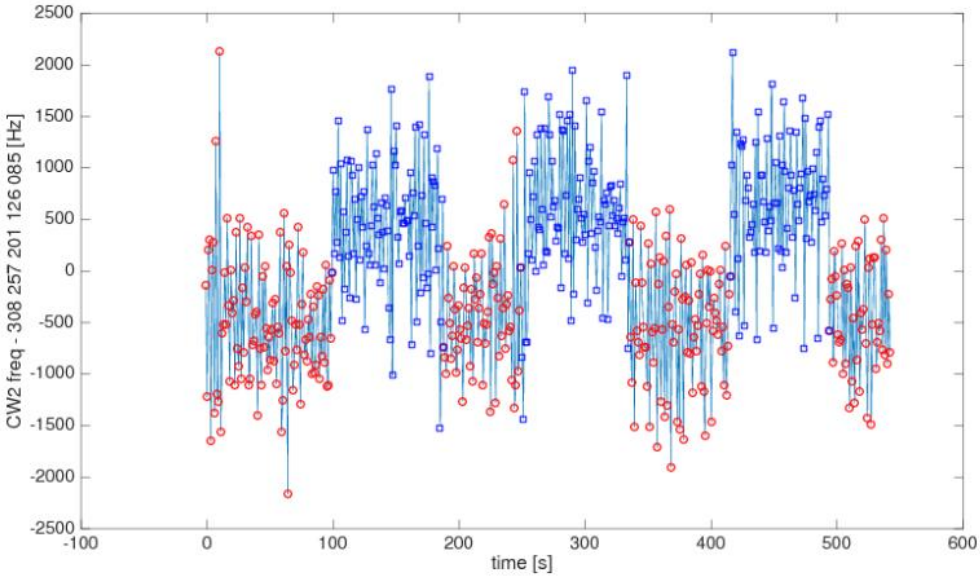

Figure 5.4: The set point of the PDH lock to the reference cavity was adjusted at 100 s intervals to ± 1 FWHM of the measured noise of the locked cavity, the frequency of the laser is measured using the frequency comb. The difference between the blue and red points gives 2 x the FWHM of the laser linewidth, assuming the dominant source of broadening of the linewidth is the quality of the lock.

5.2.2 Frequency comb

A frequency comb (Menlo Systems FC1500-250-WG) is used to monitor the frequency of the reference cavity and relate it to the SI second. The comb is generated by a femtosecond laser, which is mode-locked using the Kerr-lensing effect. The laser has a repetition rate of 250 MHz, and inherits the stability of a GPS-disciplined oven controlled quartz oscillator (OCXO) (K+K Messtechnik GPS6) via a phase-locked loop. As the comb spectrum spans a complete octave, the comb can be characterised completely. Figure 5.5 shows how the nth line of the comb is frequency doubled and beat against the 2nth line to determine the offset frequency of the zeroth line v_0, i.e.

$$v_0 = 2v_n - v_{2n}\,. \tag{5.1}$$

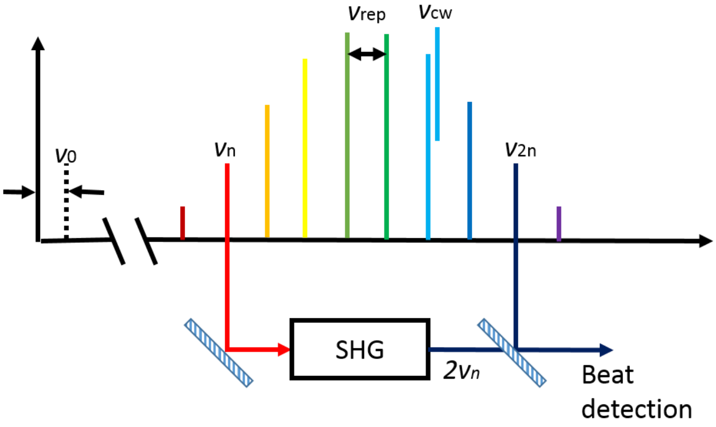

Figure 5.5: A schematic diagram of a v-2v frequency comb. The repetition rate (v_{rep}) is referenced to a microwave clock, and the offset of the zeroth line (v_0) can be determined by measuring the beat note between the frequency-doubled red end of the comb and the blue end.

The frequency of a CW laser v_{cw} beat against the nth comb line is therefore given by:

$$v_{cw} = n.v_{rep} \pm v_0 \pm v_{beat}\,, \tag{5.2}$$

where v_{beat} is the beat frequency between the CW laser and the nearest comb line. The sign of v_{beat} and v_0 can be determined by varying v_{rep} and v_0 respectively and observing whether v_{beat} increases or decreases. For example, if increasing v_{rep} causes v_{beat} to decrease, then we know that the laser v_{cw} is above the nearest comb line (as shown in Figure 5.5) and v_{beat} is positive. Next, if we increase v_0 and see v_{beat}

decrease again we know that v_0 must also be positive (as shown in Figure 5.5), as it shifts the comb to higher frequencies.

The comb line n, can then be determined trivially if it is possible to measure v_{cw} to a precision of $\frac{v_{rep}}{2}$ or better using a wavemeter, by choosing the closest integer value which satisfies equation 5.2. If a wavemeter is not available, then the measurement can be repeated for a significantly different v_{rep}, and a search can be made for a pair of integer numbers which satisfy equation 5.2 for both values of v_{rep}. Because v_{cw} is constant,

$$n_1.v_{rep1} + v_{01} + v_{beat1} + \Delta v_{cw1} = n_2.v_{rep2} + v_{02} + v_{beat2} + \Delta v_{cw2}\,, \tag{5.3}$$

where Δv_{cw} is the measurement uncertainty of v_{cw}. Letting $m = n_2 - n_1$ and solving for n_1,

$$n_1 = \frac{m.v_{rep2} + v_{02} + v_{beat2} - v_{rep2} + v_{02} + v_{beat2}}{v_{rep1} - v_{rep2}} \pm \frac{\sqrt{\Delta v_{cw1}{}^2 + \Delta v_{cw2}{}^2}}{v_{rep1} - v_{rep2}}\,. \tag{5.4}$$

The change in v_{rep} must be large enough that the last term (the measurement uncertainty) does not contribute much. With the further condition that n_1 and n_2 are both integers, n_1 and v_{cw} can be determined by searching for two frequency solutions which correspond to integer values of n_1 and n_2 within the estimated uncertainty.

The frequency comb is equipped with 20 MHz pi-type counters for accurately measuring v_0 and v_{beat}, which are read out every second. However, as the 972 nm laser is beat against the frequency doubled component of a comb centred at 1550 nm, v_0 effectively doubles to 40 MHz and a HighFinesse WS-U wavemeter with 2 MHz precision [79] can be used to identify not only n, but the sign of v_0 and v_{beat} uniquely. The technique using two significantly different repetition rates is reserved to periodically confirm the correct operation of the wavemeter.

5.2.3 Frequency shifter

An AOM with a centre frequency of 250 MHz placed between the laser and the reference cavity (shown in Figure 5.1) shifts the 972 nm light from the 1S-2S transition to the closest resonance of the reference cavity. As we wish to probe both the c-c and d-d transitions in a single trapping sequence, the AOM is configured to be able to ramp the 76 MHz spacing without unlocking the laser. Figure 5.6 shows the frequency offsets, along with the gain profile of the AOM. In the double-pass configuration, the AOM has a bandwidth (FWHM) of 100 MHz. The gain profile is programmed into the frequency controller to make the frequency shift invisible to the reference cavity, although the absolute power delivered to the reference cavity is not yet actively controlled. A Keysight 81160A synthesiser [80] was selected to drive the AOM as it boasts glitch free and drop-out free operation when shifting frequencies, and has μHz precision when referenced to the OCXO.

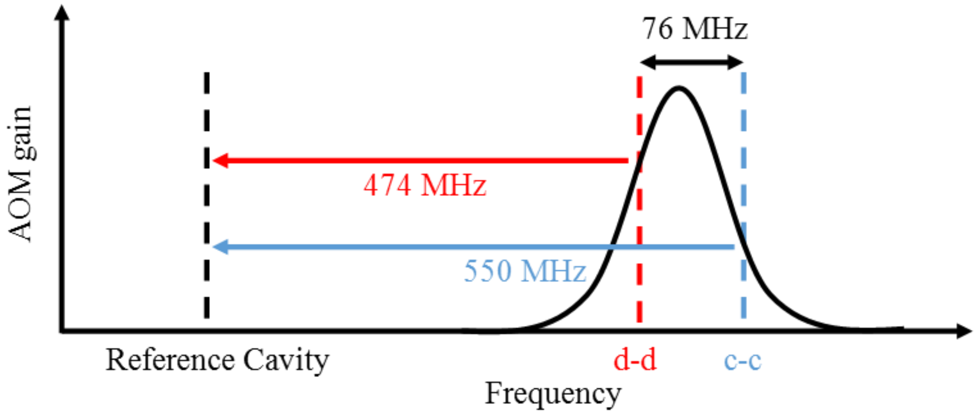

Figure 5.6: An AOM in double-pass configuration is used to shift the 972 nm light to the reference cavity frequency (not to scale). The black curve illustrates the gain profile of the AOM, which must be accounted for when normalising the output power.

The frequency control program communicates with the experimental sequencer via 2 input bits and 1 output bit. The first input bit sets the frequency to that of the c-c or d-d transition, and the second input bit chooses if the frequency is on resonance or off resonance by a pre-programmed amount. The output bit functions as a ‘laser ready’ signal, to inform the opening and closing of the shutter.

When the AOM is not ramping between different transitions, the control program updates the AOM frequency to compensate for fluctuations of the reference cavity with respect to the comb. The fluctuations are averaged over 20 seconds, which is the turning point of the Allan deviation as shown in Figure 5.7. At this timescale, the 53 mHz/s drift of the cavity is negligible. The Allan deviation (which is the square root of the Allan variance) is a standard measure of frequency stability over time [81]. For example, the Allan deviation of 2.45×10^{-13} at a gate time of 20 s (as in Figure 5.7) corresponds to a frequency instability between any two sets of 20 s measurements with a root-mean-square (RMS) fractional uncertainty of 2.45×10^{-13}, or 75 Hz at the 972 nm laser frequency.

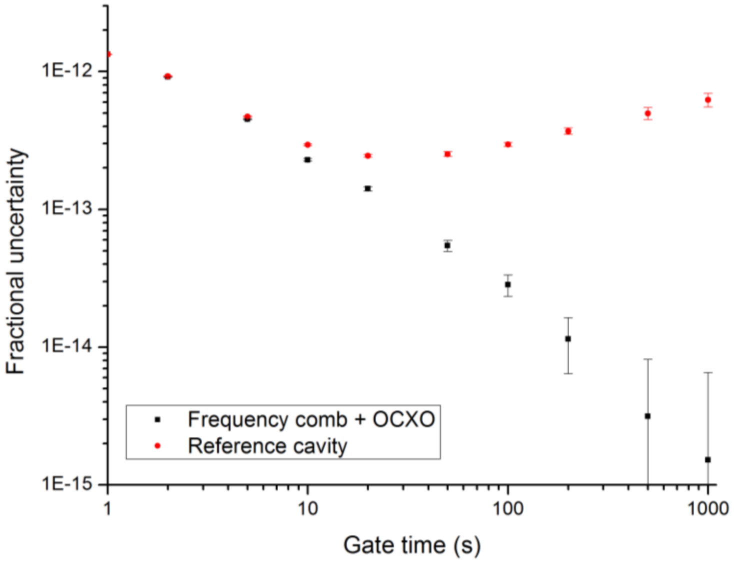

Figure 5.7: A non-overlapping Allen deviation measurement of the fractional uncertainty of the comb locked to the OCXO (black dots) and the light sent to the reference cavity (red dots). The turning point at 20 s corresponds to a fractional uncertainty of 2.45×10^{-13}*, or equivalently, 75 Hz at 972 nm.*

5.3 Beam transport

The 243 nm light must propagate along a 7 m path from the controlled atmosphere of the laser lab through an enclosed periscope onto the laser table attached to the nose of the ALPHA cryostat, before being coupled into the enhancement cavity. Power is lost along the path due to absorption within the optical elements and the air itself.

5.3.1 Optical components

The transport mirrors are from manufacturer LASEROPTIK and have a reflectivity of 99% for both s and p polarisations at angles of 45° or less. The telescope lenses are from the same manufacturer, but during 2016 were upgraded to Corning 7980 KrF glass after we observed that standard UV-grade fused silica would start fluorescing bright red (see Figure 5.8) after several hours of exposure to a $I_0 = 130$ W/cm^2 beam, and the transmission would drop. The cavity mode matching is done inside the laser lab using a Galilean telescope, before the beam is sent to the apparatus. As the laser lab is kept at a higher pressure than the experimental zone in which the apparatus sits to discourage dust from entering, a window is required between the two ends of the periscope to prevent loss of pressure. The window is 2” in diameter, 10 mm thick, and is also made from Corning 7980 KrF glass.

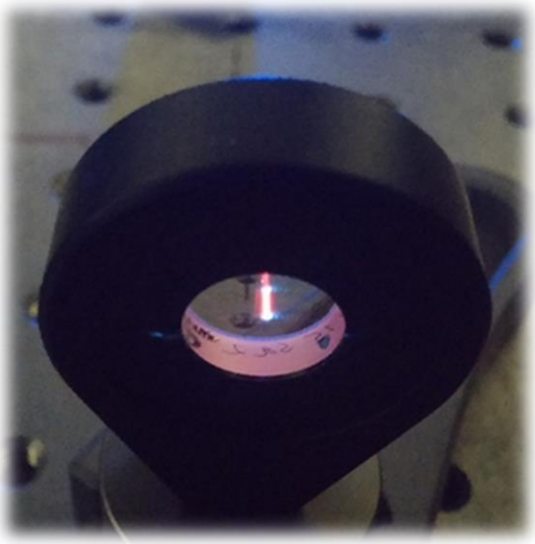

Figure 5.8: The fluorescence observed from a 243 nm beam passing through a standard UV grade fused silica substrate changes from pale blue to bright red after several hours of exposure, and the transmission through the substrate falls.

A QUBIG EOM placed close to the laser adds 6.25 MHz sidebands to the beam for use in a PDH locking scheme. A λ/2 plate before the EOM rotates the polarisation to match the axis of the birefringent crystal, and the EOM sits on a 6-axis alignment mount to correct misalignments and minimise the parasitic amplitude modulation. Typically, a polarising beam splitter and λ/4 wave plate are used to extract the reflected beam from an enhancement cavity, but due to the high losses in beam splitters available at 243 nm and the high beam power available, a simpler approach was adopted. The reflected beam is picked off through the back of one of the steering mirrors and focussed onto a THORLABS APD120A2 avalanche photodetector. The 50 – 100 µW transmitted beam is still intense enough to saturate the detector, so an additional filter must be used. The reflected signal is demodulated to produce the PDH error signal with a signal to noise ratio of about 100 (see Figure 4.41), which is sent to a Toptica Digilock 110 PID controller to lock the cavity. A THORLABS PDA10A detector looks at the beam transmitted through the cavity, but this must also be attenuated as the detector quickly degrades when more than 100 µW is incident. This is done by placing a 243 nm transport mirror in the beam path at an angle greater than 45°, and tuning the angle until it acts as a 90-10 beam splitter. The higher intensity reflected beam is directed at a screen and imaged by a camera to monitor the transverse mode structure of the output beam.

5.3.2 Losses

In addition to the losses within the optical elements, the beam intensity also suffers in air. In a still air environment such as the 5m long transport tubing between the laser lab and the experimental zone, losses as high as 50% can accumulate over minutes. There are several hypotheses about the cause of this, including ozone creation (which strongly absorbs at 243 nm) and dust/moisture becoming trapped in the beam. A study was made using an enhancement cavity on the optical bench to investigate the effects of stirring the air.

An enhancement cavity was set up on an optical table using the same mirrors as the internal cavity ($R_1 = 0.99, R_2 = 0.995$), separated by 90 cm. The cavity was excited with 50 mW of 243 nm light and a piezo mounted behind the output coupler was used to scan the length of the cavity over several FSR. A THORLABS PDA10A detector placed behind the cavity was used to measure the intensity of the light transmitted through the output coupler. It was observed that when the cavity length is expanding (i.e. when a negative voltage gradient is applied to the piezo), the transmission peaks are higher and have a flat period where the circulating power is held constant (see the red trace in Figure 5.9). This suggests that there is some thermal process which maintains the optical path length of the cavity for a given threshold intensity of 243 nm light. Placing an 85 cm long, 2 cm diameter tube between the two cavity mirrors prevents the air being stirred by the air conditioning and causes the transmitted light intensity to drop by approximately a factor of 2, in addition to lowering the threshold for the thermal effect (see the blue trace in Figure 5.9).

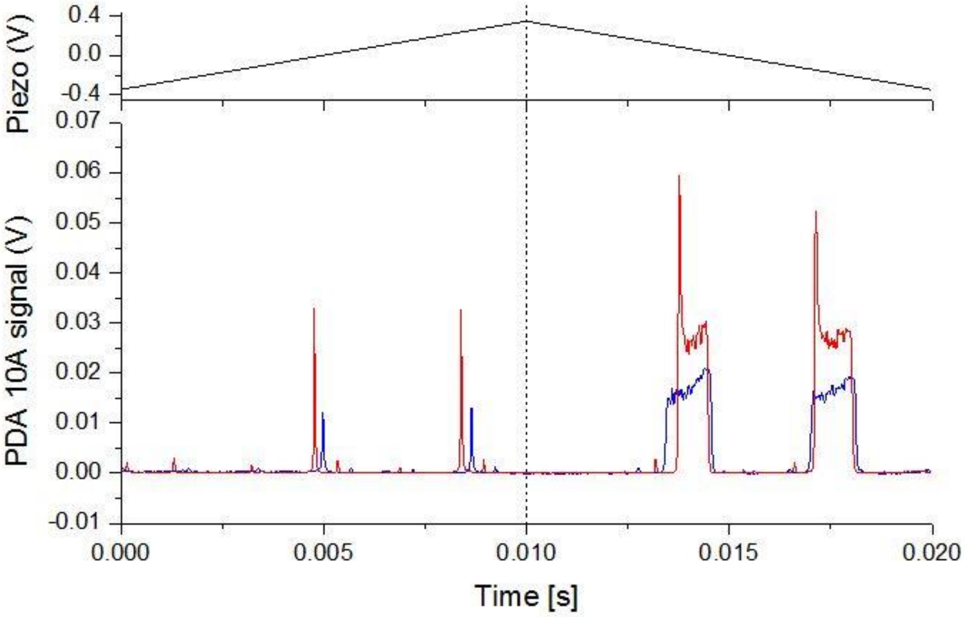

Figure 5.9: The black trace at the top of the graph shows the control voltage applied to a piezo used to scan the length of the cavity over a full spectral range. The blue trace shows the temporal mode structure of a cavity which is enclosed by a tube and the red trace shows the mode structure of a cavity which is stirred by the laboratory air conditioning.

Upon discovering this effect, the transport tubing was modified so that nitrogen gas could be flowed through it and into the zone laser box to stir the air. This improved the power transmitted through the periscope from 65 mW to 90 mW. Of the 140 mW output from the laser in 2016, losses in the EOM and mode matching lenses meant that only 110 mW reached the periscope. It is likely that another 10 mW can be gained by implementing a similar system for stirring the air in the shorter transport tubing on the laser lab side. Thermal lensing is observed in the beam path, as evidenced by the time dependent mode structure of the enhancement cavity (shown earlier in Figure 4.42). Table 5.1 summarises the losses as measured at the end of the 2016 run.

Component	Loss (%) at end of 2016 run
Transport mirrors (x13)	~1% each
EOM	15%
Convex lens	5%
Concave lens	3%
Laser lab periscope	~10%
Laser lab window	~0%
Apparatus periscope	40% without N_2 stirring ~10 % with N_2 stirring
Apparatus window	30%
Cavity input mirror	30%

Table 5.1: Power losses at 243 nm as measured at the end of the 2016 run. The components are listed in the order they are seen by the beam, with the exception of the transport mirrors which are interspersed among the other components.

5.3.3 Alignment

The 243 nm path is first pre-aligned using a class-II green laser pointer (THORLABS CPS532-C2), which is coupled in through a dichroic mirror just before the periscope. The common path mirrors have a secondary 532 nm coating with a reflectivity of about 80%. The primary aim of this guide laser was to have a safe way to align the 243 nm beam into the experimental zone, but it became a useful tool for diagnosing and aligning the enhancement cavity. Each surface of the enhancement cavity mirrors reflects ~5% of the 532 nm light, and the reflections are uniquely identifiable. By co-aligning the 532 nm beam with the reflections from the curved surfaces of the two cavity mirrors, the 243 nm beam can be injected very close to the cavity axis for trivial alignment. Additionally, by co-aligning the reflections of the curved and flat surface of each mirror and comparing them to the cavity axis, the misalignment of each mirror can be determined and the cavity axis can be completely characterised with respect to the mirrors.

5.3.4 Active beam stabilisation

Without active stabilisation, the passive beam pointing stability contributes a 50% reduction to the average power coupled into the cavity, and frequent realignment is needed. Two position sensitive detectors (ON-TRAK Photonics 2L20SP) are positioned on the optical table attached to the nose of the cryostat, and paired with piezo actuated mirrors (one on the same table and one in the laser lab) to lock the position and angle of the beam and correct any pointing errors. The detectors view the 50 – 100 µW pick-off through the back of the high-reflectivity transport mirrors, which is sufficient for identifying the position of the beam. A homemade FPGA based PID controller locks the beam with an accuracy of 20 mV, which corresponds to 20 µm on each detector. With the lock engaged, there is no visible noise contribution to the cavity due to beam pointing, and minor adjustments to the alignment are only required every few hours. In addition, the control system allows the user to align the beam remotely when access to the zone is not possible.

6 Experimental results

In 2014, a first attempt at observing the 1S-2S transition in antihydrogen was conducted with a newly arrived 243 nm laser and the first iteration of a cryogenic enhancement cavity. The reference cavity and frequency comb had not yet arrived, so the laser frequency control was limited by the 2 MHz precision of the wavemeter, which measures the SHG 486 nm light (recall from chapter 3 the linewidth of the transition is expected to be approximately 60 kHz at 243 nm). The frequency comb and ultra-stable reference cavity arrived in 2015, and the next two years were dedicated to making a serious measurement of the 1S-2S transition. Whilst in 2015 the cavity intensity was insufficient to detect the transition, the 1.05 W of circulating power and greatly improved trapping rate in 2016 made for a viable experiment.

6.1 Experimental protocol

6.1.1 2014

In 2014, the experiment searched for a reduction in the apparent trapping rate when the laser was tuned to the d-d transition (“on resonance”), compared to when it was detuned by 50 MHz (at 243 nm) below the transition (“off resonance”). On and off resonance runs were interspersed, and apart from the laser frequency, were otherwise identical. The magnetic trap was flattened by bucking (running current in reverse) mirror coils B-D to increase the length of the minimum field region. The experimental protocol was as follows:

1) Antihydrogen is formed using the autoresonance technique, and a 1 s wait ensures that any trapped atoms have sufficient time to decay to the ground state.
2) A shutter between the laser lab and the apparatus opens, to allow the 243 nm light to enter the apparatus.
3) The enhancement cavity is locked for 300 s.

4) The shutter is closed, and electric fields are pulsed to remove any charged particles (particularly antiprotons) from the trap.
5) The trap is shut down by triggering the quench response for the superconducting magnets, and the silicon detector counts the number of annihilation events.

6.1.2 2015

As the circulating power within the external cavity in 2015 was estimated to be below the threshold where a difference in the trapping rate would be discernible, the experiment was reconfigured to try to detect laser ionised antihydrogen atoms with a very low background. Instead of using the full magnetic trap, a shorter trap was formed using only mirror coils A-D. Mirror E was bucked to cancel out the field of the external 1 T solenoid and create a zero-field region within the detector. A weak potential well was formed in the mixing trap with the aim to capture the antiproton from the ionised atom. The gradient of the electrostatic potential was limited to prevent mixing of the 2S and 2P states. As the lifetime of single antiprotons in a long well is thought to be short, the well was dumped towards the zero field region every second. The silicon detector then counted the annihilations localised to beneath mirror coil E within a 9 ms window either side of the dump. Instead of quenching the magnets, the trap was shut down by ramping down the magnets over a period of 1.5 s. This induces much lower currents in the Penning trap electrodes when compared with quenching the magnets, resulting in less heating and therefore a higher overall duty cycle of the experiment, as well as allaying fears that quenching the magnets could cause electrical shorts between the electrodes.

As in 2014, on and off resonance runs were interspersed, but the off resonance shift was reduced to 200 kHz (at 243 nm) below the transitions and both the c-c and d-d transitions were targeted. Towards the end of the season, a ‘no laser’ run was added to investigate the effect of the laser on the trapping rate. For example; the laser light could cause additional outgassing from the cryogenic surfaces and reduce the antihydrogen lifetime. This run had identical timing to the on and off resonance runs, but the laser shutter never opened. To maximise data taking in the on and off resonance runs, the no laser runs were not run as frequently as their laser counterparts. The experimental protocol was as follows:

1) Antihydrogen is formed using the autoresonance technique, and a 1 s wait ensures that any trapped atoms have sufficient time to decay to the ground state.
2) Electric fields are pulsed to remove any charged particles from the trap, before a weak electrostatic well is formed to trap any laser ionised antihydrogen atoms (antiprotons).
3) With the laser tuned to the d-d transition, the shutter between the laser lab and the apparatus is opened.
4) The cavity is locked for 250 s, and the contents of the electrostatic well are dumped towards the zero field region every second.
5) The shutter closes, and the laser frequency is ramped to the c-c transition in 10 s. The shutter reopens once the correct frequency is reached and the laser is stable.
6) The cavity is locked for an additional 250 s, and the contents of the electrostatic well continue to be dumped towards the field free region every second.
7) The shutter closes, and electric fields are pulsed to remove any remaining charged particles from the trap.
8) The magnets are ramped down over 1.5 s, and the silicon detector counts the number of annihilation events.

6.1.3 2016

In 2016, a greatly improved trapping rate and a higher circulating power within the enhancement cavity made for a much more feasible experiment. The trap magnets were run in the same flattened field configuration as in 2014, but the trap was shut down using the 1.5 s ramp down technique used in 2015. On resonance, off resonance (-200 kHz at 243 nm), and no laser runs were strictly interspersed to reduce the sensitivity of the experiment to trapping rate fluctuations, with the repeating sequence: on resonance, off resonance, no laser, off resonance, on resonance, no laser. Whilst the main aim of the experiment was to identify a difference between the apparent trapping rate of on vs off resonance runs, a shallow electrostatic well was formed in the Penning trap to try to collect any ionised antihydrogen atoms (antiprotons). At the end of each 300 s laser exposure period, the contents of the trap were ejected towards the MCP to image any trapped antiprotons, although it was considered unlikely that the antiprotons would remain trapped within the long well. The experimental protocol was as follows:

1) Antihydrogen is formed in two successive mixing cycles using the slow merge technique, and a 1 s wait ensures that any trapped atoms have sufficient time to decay to the ground state.
2) Electric fields are pulsed to remove any charged particles from the trap, before a weak electrostatic well is formed to contain any laser ionised antihydrogen atoms (antiprotons).
3) With the laser tuned to the d-d transition, the shutter between the laser lab and the apparatus is opened.
4) The cavity is locked for 300 s.
5) The shutter closes, and the laser frequency is ramped to the c-c transition in 10 s. Whilst the shutter is closed, the contents of the electrostatic well are ejected towards the MCP. The shutter reopens once the correct frequency is reached and the laser is stable.
6) The cavity is locked for an additional 300 s
7) The shutter closes, and the contents of the electrostatic well are again ejected towards the MCP.
8) The magnets are ramped down over 1.5 s, and the silicon detector counts the number of annihilation events.

Table 6.1 gives a summary of the experimental protocol employed across the three years.

	2014	2015	2016
Laser exposure	300 s (d-d only)	2 x 250 s	2 x 300 s
Detection window	30 ms	1.5 s	1.5 s
Mixing technique	Autoresonance	Autoresonance	Slow merge
Antihydrogen stacks	1	1	2

Table 6.1: A summary of the experimental protocol employed in 2014, 2015 and 2016.

6.2 Results and analysis

6.2.1 2014

Due to the low circulating power within the enhancement cavity, and the lack of precise frequency metrology in 2014, only a single shift worth of trapped atoms were dedicated to 1S-2S transition measurements. As expected from simulations, there was no significant difference detected between the on and off resonance trapping rates.

Type	Trials	Detected events	Rate
On resonance	5	6	1.2 ± 0.73
Off resonance	4	6	1.5 ± 0.96

Table 6.2: The annihilation events detected during the shutdown of the neutral trap. The magnet system is intentionally quenched to de-energise the neutral trap in <30 ms, so there is no significant detector background. The error of the rate is from the $\sqrt{N}$ counting statistics alone.

6.2.2 2015

With around 0.45 W of circulating power within the external cavity of 2015, simulation predicted that there would be no discernible difference between the on and off resonance trials in the disappearance data. Whilst this is apparent in the data shown in Table 6.3, what is surprising is that the no laser runs actually have a significantly lower rate than the off resonance runs. This is due to the fact that the no laser runs were introduced late into the experiment and were not able to accurately capture the trapping rate. The higher number of on resonance trials compared to off resonance trials is an artefact of the way the shifts were run; each 8 hour beam period allowed for approximately 8 pairs of on and off resonance runs, but always started with an on resonance run – an additional bias which needed to be addressed in 2016.

Type	Trials	Detected events	Expected background	Rate
On resonance	42	27	3	0.64 ± 0.12
Off resonance	39	24	2.8	0.62 ± 0.13
No laser	12	4	0.9	0.33 ± 0.17

Table 6.3: The annihilation events detected during the 1.5 s ramp down of the neutral trap magnets. The error of the rate is the standard deviation about the mean of the number of detected events.

Annihilation events were searched for within the zero-field region and within 9 ms either side of the dumps but none were found, suggesting that this appearance mode detection technique may not work. The search was widened to include the entire trap, but the results were still consistent with background.

6.2.3 2016

In 2016, it was quickly discovered that exciting the cavity with 243 nm light reduces the antihydrogen production and trapping rates over time. This is most evident in the mixing triggers (a number which is proportional to the number of antihydrogen atoms produced) as shown in Figure 6.1, which plots the cumulative laser exposure against the mixing triggers for two trapping series with different laser powers. The effect is also visible in Figure 6.2, which plots the number of detected annihilation events against the trial number for the published trapping data. From this plot it is already clear that there is a significant difference between the on and off resonance runs, whilst the good agreement between the off resonance and no laser runs suggest that the laser does not adversely influence the antihydrogen lifetime. The full set of data is shown in Table 6.4. No evidence of antiproton annihilations was seen on the MCP images of the dumps at the end of each 300 s hold.

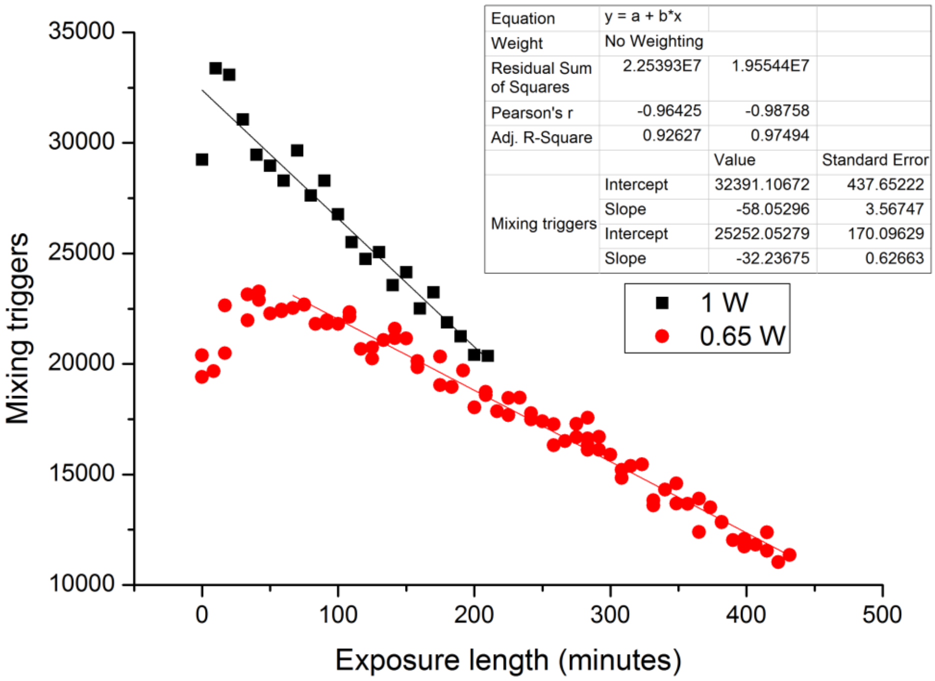

Equation	y = a + b*x		
Weight	No Weighting		
Residual Sum of Squares	2.25393E7	1.95544E7	
Pearson's r	-0.96425	-0.98758	
Adj. R-Square	0.92627	0.97494	
		Value	Standard Error
Mixing triggers	Intercept	32391.10672	437.65222
	Slope	-58.05296	3.56747
	Intercept	25252.05279	170.09629
	Slope	-32.23675	0.62663

Figure 6.1: A plot of the declining mixing triggers (proportional to antihydrogen production) when the 243 nm cavity is locked for two trapping series with 1 W circulating power (black squares) and 0.65 W of circulating power (red circles). The first few points of the 0.65 W series are low as the laser experiment has begun whilst some trap surfaces are still cooling down.

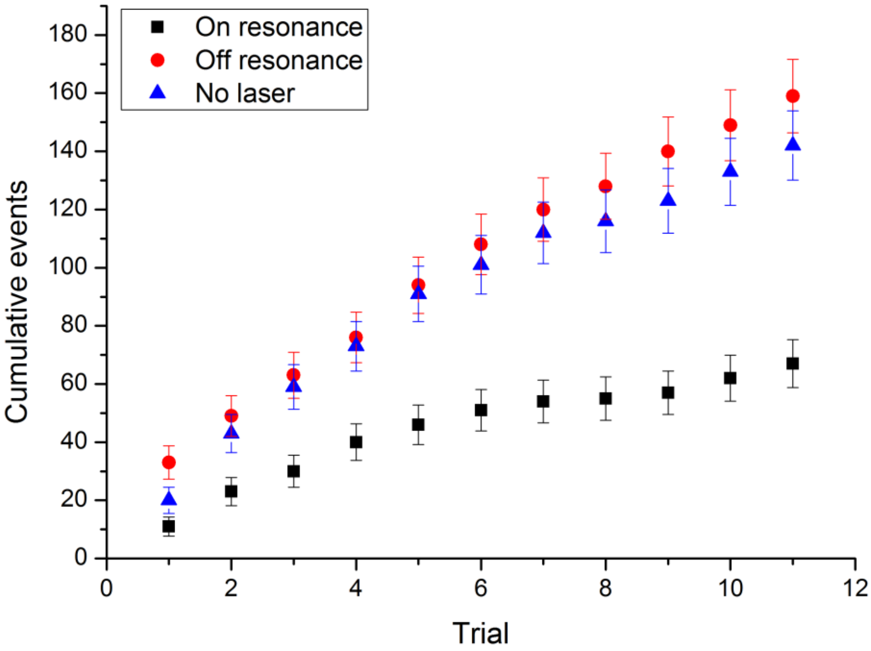

Figure 6.2: Evolution of the trapping data for the on resonance, off resonance, and no laser runs. The error bars represent the counting statistics ($\sqrt{N}$) alone.

Type	Trials	Detected events	Expected background	Uncertainty
Off resonance	11	159	0.7	13
On resonance	11	67	0.7	8.2
No laser	11	142	0.7	12

Table 6.4: The number of events detected upon ramping down the trap after 2 x 300 s of laser exposure on resonance, laser exposure off resonance, or a wait without any laser exposure. The uncertainty is from the counting statistics($\sqrt{N}$) alone.

The silicon vertex detector is not only active during the ramp down of the trap magnets, but is continuously triggered throughout the measurement cycle. The 2 x 300 s laser exposure periods can be analysed with a different MVA routine which reduces the cosmic background rate to 0.0043 ± 0.0003 Hz (at the cost of reducing the overall reconstruction efficiency to 0.376 ± 0.002) [60], to try to detect the spin-flipped or laser ionised atoms which aren't surviving in the trap long enough to be imaged by the

MCP. A significantly higher number of detected events were observed during the on resonance runs, compared to the off resonance and no laser runs which are both consistent with the expected background. The distribution of detected events was approximately equal between the c-c and d-d transitions.

	Pass-cut (2014 & 2015)	Disappearance MVA (2016)	Appearance MVA (2016)
Reconstruction efficiency	0.634	0.688 ± 0.002	0.376 ± 0.002
Cosmic false-positive rate (Hz)	0.042	0.042	0.0043 ± 0.0003

Table 6.5: Detector efficiency of the different protocols

Type	Detected events	Expected background	Uncertainty
d-d off resonance	15	14.2	3.9
d-d on resonance	39	14.2	6.2
No laser, 1st 300 s	22	14.2	4.7
c-c off resonance	12	14.2	3.5
c-c on resonance	40	14.2	6.3
No laser, 2nd 300 s	8	14.2	2.8
d-d + c-c off resonance	27	28.4	5.2
d-d + c-c on resonance	79	28.4	8.9
No laser (sum)	30	28.4	5.5

Table 6.6: The number of events detected during the 300 s hold periods. The uncertainty is from counting statistics ($\sqrt{N}$) alone.

6.3 Conclusion

Examining the results of the 2016 1S-2S experiment, we find a very significant difference in the number of detected annihilations between the on resonance and off resonance trials (C-test [82], probability of result being due to statistical fluctuations of 4.2×10^{-10}) when the magnetic trap is shut down after the laser exposure. From these results, we conclude that 58 ± 6% of the trapped antihydrogen atoms have been removed from the trap via resonant 1S-2S excitation, followed by either a spin-flip or ionisation event. This fraction is in good agreement with the simulations presented in chapter 3, which predict a loss of 47% for a circulating power of 1 W within the enhancement cavity. The off resonance and no laser trials are in good agreement, suggesting that the laser has had no adverse effect on the antihydrogen lifetime.

Looking for annihilations during the 300 s long hold times with an MVA protocol optimised to reduce the rate of false-positives from the cosmic background, we again see a clear statistical difference (C-test [82], probability of result being due to statistical fluctuations of 2.2×10^{-7}) between the on and off resonance runs. We also see that atoms are excited at both the c-c and d-d (on resonance) transition frequencies, with an approximately equal distribution. The signal observed during the off resonance and no laser trials is consistent with the cosmic background rate alone.

Taking into account the relative efficiency of the two MVA protocols, we see that the number of atoms lost from the trap ($\frac{92}{0.688} = 134 \pm 11.9$) is in good agreement with the number of annihilations detected during the two 300 s laser exposure periods ($\frac{52}{0.376} = 138 \pm 23.7$) when the laser frequency is tuned on resonance.

7 Conclusions and Outlook

The first resonant excitation of an optical transition within an anti-atom has been observed. If the spectrum of antihydrogen is assumed to be similar to that of hydrogen (i.e. there are no exotic asymmetries in the spectrum of antihydrogen), then the 400 kHz (at 121 nm) resolution of this measurement can be interpreted as a test of CPT theory at a precision of 200 parts-per-trillion. However, a stronger statement of CPT invariance requires a detailed measurement of the transition line shape, which is one of the main goals of the ALPHA collaboration during the 2017 antiproton beam period. The sensitivity of this initial measurement is approximately 2×10^{-18} GeV in terms of the absolute energy scale, which approaches the precision of the CPT test in the neutral kaon system of approximately 5×10^{-19} GeV [3].

The next step is to extend the techniques used to observe the transition to make a measurement of the full 1S-2S line shape. The laser-induced degradation of the antihydrogen production and trapping rates imposes a significant time constraint, as it requires a full thermal cycle of the apparatus to recover from. Whilst it may be possible to mitigate this effect by reducing the amount of scattered light from the cavity mirrors which reaches the electrodes, the recently developed antihydrogen accumulation technique enables many more antihydrogen atoms to be simultaneously interrogated by the laser, reducing the overall laser exposure, and allowing several frequencies to be measured per thermal cycle. The signal to noise ratio already demonstrated shows that it is possible to distinguish the c-c and d-d transitions individually, and this could be further improved by ejecting one of the states using resonant microwaves. Measuring the line shape with a precision of 40 kHz (at 121 nm) is a reasonable goal for the 2017 antiproton beam period, and requires no further modifications to the apparatus. Such a measurement would improve upon the precision of our current measurement by a factor of 10, and constitute a test of CPT theorem at the 20 part-per-trillion level. In terms of the absolute energy scale, this CPT test would have a precision of 2×10^{-19} GeV, surpassing that of the neutral kaon system. Going beyond this precision will most likely require overcoming the transit time broadening, which can be achieved by either laser cooling the trapped antihydrogen atoms or by increasing the waist size of the 243 nm enhancement cavity. Both of these options are the subject of ongoing investigation within ALPHA.

In addition to providing a sensitive test of CPT theory, the ability to excite antihydrogen to the 2S state opens up the opportunity to explore further physics such as the ‘anti-Rydberg constant’, the ‘anti-Lamb shift’, and the antiproton charge radius by measuring additional optical transitions in antihydrogen.

References

[1] L. Canetti, M. Drewes and M. Shaposhnikov, “Matter and Antimatter in the Universe,” *New Journal of Physics,* vol. 14, 2012.

[2] J. H. Christenson, J. W. Cronin, V. L. Fitch and R. Turlay, “Evidence for the 2π Decay of the K Meson,” *Physical Review Letters,* vol. 13, no. 138, 1964.

[3] NA31 and NA48 Collaborations, “A precision measurement of direct CP violation in the decay of neutral kaons into two pions,” *Physical Letters B,* vol. 544, no. 1-2, 2002.

[4] A. Alavi-Harati et al. (KTeV Collaboration), “Measurements of direct CP violation, CPT symmetry, and other parameters in the neutral kaon system,” *Physical Review D,* vol. 67, no. 1, 2003.

[5] M. Kobayashi and M. Toshihide, “CP-Violation in the Renormalizable Theory of Weak Interaction,” *Progress of Theoretical Physics,* vol. 49, no. 2, 1973.

[6] CERN, “ELENA Project,” [Online]. Available: https://espace.cern.ch/elena-project/sitepages/home.aspx. [Accessed 16 02 2017].

[7] J. DiSciacca et al. (ATRAP Collaboration), “One-Particle Measurement of the Antiproton Magnetic Moment,” *Physical Review Letters,* vol. 110, 2013.

[8] H. Nagahama et al. (BASE Collaboration), “Sixfold improved single particle measurement of the magnetic moment of the antiproton,” *Nature Communications,* 2017.

[9] CERN, “The BASE antiprotons celebrate their first birthday,” CERN press release, [Online]. Available: https://home.cern/about/updates/2016/12/base-antiprotons-celebrate-their-first-birthday.

[10] M. Hori et al. (ASACUSA Collaboration), “Two-photon laser spectroscopy of antiprotonic helium and the antiproton-to-electron mass ratio,” *Nature,* no. 475, pp. 454-488, 2011.

[11] D. H. Freedman, *Antiatoms: Here Today...,* Discover magazine, 1997.

[12] G. Blanford, D. Christian, K. Gollwitzer, M. Mandelkern, C. Munger, J. Schultz and G. Zioulas, “Observation of Atomic Antihydrogen,” *Physical Review Letters,* vol. 80, no. 14, 1997.

[13] M. Amoretti et al. (ATHENA Collaboration), “Production and detection of cold antihydrogen atoms,” *Nature,* vol. 419, pp. 456-459, 2002.

[14] G. Gabrielse et al. (ATRAP Collaboration), “Driven Production of Cold Antihydrogen and the First Measured Distribution of Antihydrogen States,” *Physical Review Letters,* vol. 89, no. 23, 2002.

[15] N. Kuroda et al. (ASACUSA Collaboration), “A source of antihydrogen for in-flight hyperfine spectroscopy,” *Nature Communications,* vol. 5, 2014.

[16] T. Namba, “Precise measurement of positronium,” *Prog Theor Exp Phys,* no. 1, 2012.

[17] A. S. Kadyrov, C. M. Rawlins, A. T. Stelbovics, I. Bray and M. Charlton, “Antihydrogen Formation via Antiproton Scattering with Excited Positronium,” *Physical Review Letters,* vol. 114, no. 18, pp. 183-201, 2015.

[18] G. B. Andresen et al. (ALPHA Collaboration), “Trapped antihydrogen,” *Nature,* vol. 468, pp. 673-676, 2010.

[19] G. Gabrielse et al. (ATRAP Collaboration), “Trapped Antihydrogen in its Ground State,” *Physical Review Letters,* vol. 108, p. 113002, 2012.

[20] G. B. Andresen et al. (ALPHA Collaboration), “Confinement of antihydrogen for 1,000 seconds,” *Nature Physics,* vol. 7, pp. 558-564, 2011.

[21] C. Amole et al. (ALPHA Collaboration), “Description and first application of a new technique to measure the gravitational mass of antihydrogen,” *Nature Communucations,* vol. 4, p. 1785, 2013.

[22] C. Amole et al. (ALPHA Collaboration), “An experimental limit on the charge of antihydrogen,” *Nature communications,* vol. 5, p. 3955, 2014.

[23] M. Baquero-Ruiz, A. E. Charman, J. Fajans, A. Little, A. Povilus, F. Robicheaux, J. S. Wurtele and A. I. Zhmoginov, “Using stochastic acceleration to place experimental limits on the charge of antihydrogen,” *New Journal of Physics,* vol. 16, 2014.

[24] M. Ahmadi et al. (ALPHA Collaboration), “An improved limit on the charge of antihydrogen from stochastic acceleration,” *Nature,* vol. 529, pp. 373-376, 2016.

[25] C. Amole et al. (ALPHA Collaboration), “Resonant quantum transitions in trapped antihydrogen atoms,” *Nature,* vol. 483, pp. 439-443, 2012.

[26] S. Maury, “The antiproton decelerator: AD,” *Hyperfine Interactions,* vol. 109, pp. 43-52, 1997.

[27] G. Gabrielse, “Particle Motions in a Penning Trap,” [Online]. Available: http://gabrielse.physics.harvard.edu/gabrielse/papers/1990/1990_tjoelker/chapter_2.pdf. [Accessed 03 05 2017].

[28] Physik Uni Mainz, “The Penning Trap,” [Online]. Available: http://wswww.physik.uni-mainz.de/werth/g_fak/penning.htm.

[29] G. B. Andresen et al. (ALPHA Collaboration), “Compression of Antiproton Clouds for Antihydrogen Trapping,” *Phys. Rev.Lett.,* vol. 100, no. 20, 2008.

[30] G. B. Andresen et al. (ALPHA Collaboration), "Centrifugal Separation and Equilibration Dynamics in an Electron-Antiproton Plasma," *Phys. Rev. Lett,* vol. 106, no. 14, 2011.

[31] T. J. Murphy and C. M. Surko, "Positron trapping in an electrostatic well by inelastic collisions with nitrogen molecules," *Physical Review A,* vol. 46, pp. 5696-5705, 1992.

[32] D. P. van der Werf, L. V. Jørgensen, T. L. Watson, M. Charlton, M. J. T. Collier, M. Doser and R. Funakoshi, "The ATHENA positron accumulator," *Applied Surface Science,* vol. 194, pp. 312-316, 2002.

[33] ALPHA, "Alpha Experiment," [Online]. Available: http://alpha.web.cern.ch. [Accessed 24 04 2017].

[34] C. Amole et al. (ALPHA Collaboration), "The ALPHA antihydrogen trapping apparatus," *Nuclear Intsruments and Methods in Physics Research,* vol. 735, pp. 319-340, 2014.

[35] G. B. Andresen et al. (ALPHA Collaboration), "Evaporative Cooling of Antiprotons to Cryogenic Temperatures," *Physical Review Letters,* vol. 105, 2010.

[36] G. B. Andresen et al. (ALPHA Collaboration), "Antiproton, positron, and electron imaging with a microchannel plate/phosphor detector," *Review of Scientific Instruments,* vol. 80, 2009.

[37] E. Klempt, C. Batty and J.-M. Richard, "The antinucleon–nucleon interaction at low energy: Annihilation dynamics," *Physics Reports,* vol. 413, pp. 197-317.

[38] G. B. Andresen et al. (ALPHA Collaboration), "The ALPHA – detector: Module Production and Assembly," *Journal of Instrumentation,* vol. 7, 2012.

[39] C. Amole et al. (ALPHA Collaboration), "Silicon vertex detector upgrade in the ALPHA experiment," *Nuclear Instruments and Methods in Physics Research Section A,* vol. 732, pp. 134-136, 2013.

[40] D. L. Eggleston, B. R. Driscoll, A. W. Hyatt and J. H. Malmberg, "Parallel energy analyzer for pure electron plasma devices," *Physics of Fluids B: Plasma Physics,* vol. 4, no. 10, 1992.

[41] M. D. Tinkle, G. G. Greaves, C. M. Surko, R. L. Spencer and G. W. Mason, "Low-order modes as diagnostics of speroidal non-neutral plasmas," *Physical Review Letters,* vol. 72, no. 3, 1994.

[42] C. Amole et al. (ALPHA Collaboration), "In situ electromagnetic field diagnostics with an electron plasma in a Penning–Malmberg trap," *New Journal of Physics,* vol. 16, 2014.

[43] S. Roy, S. Gosh Deb and C. Sinha, "Formation of antihydrogen in three-body antiproton-positron collisions," *Physical Review A,* vol. 76, 2008.

[44] J. Fajans and L. Friedland, “Autoresonant (nonstationary) excitations of pendulums, Plutinos, plasmas, and other nonlinear oscillators,” *American Journal of Physics,* vol. 69, no. 10, 2001.

[45] W. Bertsche, J. Fajans and L. Friedland, “Direct Excitation of High-Amplitude Chirped Bucket-BGK Modes,” *Physical Review Letters,* vol. 91, no. 26, 2003.

[46] C. Carruth et al. (ALPHA Collaboration), “Evaporative cooling in the strong drive regime to produce stable plasmas for antihydrogen production,” *Manuscript in preparation.*

[47] J. Fajans, N. Madsen and F. Robicheaux, “Critical loss radius in a Penning trap subject to multipole fields,” *Physics of Plasmas,* vol. 15, no. 3, 2008.

[48] C. L. Cesar, “Trapping and Spectroscopy of Hydrogen,” *Hyperfine Interactions,* vol. 109, pp. 293-304, 1997.

[49] C. G. Parthey, A. Matveev, J. Alnis, B. Bernhardt, A. Beyer, R. Holzwarth, A. Maistrou, R. Pohl, K. Predehl, T. Udem, T. Wilken, N. Kolachevsky, M. Abgrall, D. Rovera, C. Saloman, P. Laurent and T. W. Hänsch, “Improved Measurement of the Hydrogen 1S-2S Transition Frequency,” *Physical Review Letters,* vol. 107, no. 20, 2011.

[50] R. C. Telfer, “Everything You Always Wanted to Know About the Hydrogen Atom (But Were Afraid to Ask),” Johns Hopkins University, 1996.

[51] R. P. Feynman, R. B. Leighton and M. Sands, The Feynman Lectures on Physics, Reading, Massachusetts: Addison-Wesley, 1965.

[52] C. Rasmussen, “Tests Of Fundamental Symmetries With Trapped Antihydrogen (PhD thesis),” Aarhus University, 2016.

[53] H. A. Bethe and E. E. Salpeter, Quantum Mechanics of One- and Two-Electron Atoms, Springer Berlin Heidelberg, 1957.

[54] M. C. Usselman, Encyclopedia Britannica, retrieved 2013.

[55] J.B.Hearnshaw, The analysis of starlight, Cambridge: Cambridge University Press, 1986.

[56] G. Kirchhoff, “Ueber die Fraunhofer'schen Linien,” *Annalen der Physik,* vol. 185, no. 1, pp. 148-150, 1860.

[57] W. E. Lamb and R. C. Retherford, “Fine structure of the Hydrogen Atom by a Microwave Method,” *Physical Review,* vol. 72, no. 3, pp. 241-243, 1947.

[58] A. Dupays, A. Beswick, B. Lepetit and C. Rizzo, “Proton Zemach radius from measurements of the hyperfine splitting of hydrogen and muonic hydrogen,” *Physical Reveiw A,* 2003.

[59] N. Kolachevsky, A. Matveev, J. Alnis, C. G. Parthey, S. G. Karshenboim and T. W. Hänsch, "Measurement of the 2S Hyperfine Interval in Atomic Hydrogen," *Physical Review Letters,* vol. 102, no. 21, 2009.

[60] M. Ahmadi et al. (ALPHA Collaboration), "Observation of the 1S–2S transition in trapped antihydrogen," *Nature,* vol. 541, pp. 506-510, 2016.

[61] Toptica, "TA-FHG pro," [Online]. Available: http://www.toptica.com/products/tunable-diode-lasers/frequency-converted-lasers/ta-fhg-pro/. [Accessed 5 January 2017].

[62] B. E. A. Saleh and M. C. Teich, Fundamentals of Photonics, Wiley, 2007.

[63] F. Dominec, "Optical cavity," [Online]. Available: https://commons.wikimedia.org/w/index.php?curid=3017470. [Accessed 21 04 2017].

[64] Sasada Lab, "Light possessing orbital angular momenta," Keio University, [Online]. Available: http://www.phys.keio.ac.jp/guidance/labs/sasada/research/orbangmom-en.html. [Accessed 15 05 2017].

[65] R. Drever, J. L. Hall, F. V. Kowalski, J. Hough, G. M. Ford, A. J. Munley and H. Ward, "Laser phase and frequency stabilization using an optical resonator," *Applied Physics B: Lasers and Optics 31,* pp. 97-105, 1983.

[66] J. J. Herbert, "Techniques for Deriving Optimal Bondlines for Athermal Bonded Mounts," *Proc. SPIE,* vol. 6288, 2006.

[67] M. Bayar, "Lens barrel optomechanical principles," *Optical Engineering,* vol. 20, no. 2, 1981.

[68] D. Vukobratovich, K. A. Fetterhoff, J. R. Myers, P. D. Wheelwright and G. R. Cunnington, "Bonded mounts for small cryogenic optics," *SPIE Proceedings,* vol. 4131, no. 228, 2000.

[69] H. Kihm, H. S. Yang, I. K. Moon and Y. W. Lee, "Athermal Elastomeric Lens Mount for Space Optics," *Journal of the Optical Society of Korea,* vol. 13, pp. 201-205, 2009.

[70] EPOTEK, "H77 Datasheet," April 2010. [Online].

[71] EPO-TEK, "T7109 datasheet," April 2010. [Online].

[72] R. J. Corruccini and J. J. Gniewek, "Thermal Expansion of Technical Solids at Low Temperatures," National Bureau of Standards, Washington, 1961.

[73] D. Eason, "OpenFringe," 28 04 2016. [Online]. Available: https://sourceforge.net/projects/openfringe/.

[74] R. M. Goldstein, H. A. Zebker and C. L. Werner, "Satellite radar interferometry: Two-dimensional phase unwrapping," *Radio Science,* vol. 23, no. 4, pp. 713-720, 23 1988.

[75] Corning Incorporated, "HPFS Fused Silica KrF Grade," 2008.

[76] D. Gangloff, M. Shi, T. Wu, A. Bylinskii, B. Braverman, M. Gutierraz, R. Nichols, J. Li, K. Aicholz, M. Cetina, L. Karpa, B. Jelenkovic, I. Chuang and V. Vuletic, “Preventing and Reversing Vacuum-Induced Optical Losses in High-Finesse Tantalum(V) Oxide Mirror Coatings,” *Optical Express,* vol. 23, no. 14, pp. 18014-18028, 2015.

[77] Y. N. Zhao, “Sub-Hertz frequency stabilization of a commercial diode laser,” *Optics Communications,* vol. 283, no. 23, pp. 4696-4700, 2010.

[78] M. Lessing, “Menlo Systems’ Optical Reference System (ORS): Design and Performance,” 2016.

[79] HighFinesse, “HighFinesse Wavelength Meter,” [Online]. Available: http://www.highfinesse.com/en/wavelengthmeter. [Accessed 03 07 2017].

[80] Keysight Technologies, “81160A Pulse Function Arbitrary Noise Generator,” [Online]. Available: http://www.keysight.com/en/pd-1946612-pn-81160A/pulse-function-arbitrary-noise-generator. [Accessed 12 08 2017].

[81] D. W. Allan, “Allan Variance,” [Online]. Available: http://www.allanstime.com/AllanVariance/index.html. [Accessed 05 January 2017].

[82] J. Przyborowski and H. Wilenski, “Homogeneity of results in testing samples from Poisson series: with an application to testing clover seed for dodder,” *Biometrika,* vol. 31, pp. 313-323, 1940.